



A11105 157030

**NBSIR 86-3452**

# **Impact-Echo: A Method for Flaw Detection in Concrete Using Transient Stress Waves**

---

Mary Sansalone  
Nicholas J. Carino

U.S. DEPARTMENT OF COMMERCE  
National Bureau of Standards  
National Engineering Laboratory  
Center for Building Technology  
Structures Division

September 1986



---

U.S. DEPARTMENT OF COMMERCE  
NATIONAL BUREAU OF STANDARDS

QC  
100  
.U56  
NO.86-3452  
1986



NBSIR 86-3452

**IMPACT-ECHO: A METHOD FOR FLAW  
DETECTION IN CONCRETE USING  
TRANSIENT STRESS WAVES**

---

Mary Sansalone  
Nicholas J. Carino

U.S. DEPARTMENT OF COMMERCE  
National Bureau of Standards  
National Engineering Laboratory  
Center for Building Technology  
Structures Division  
Gaithersburg, MD 20899

September 1986

**U.S. DEPARTMENT OF COMMERCE, Malcolm Baldrige, *Secretary***  
**NATIONAL BUREAU OF STANDARDS, Ernest Ambler, *Director***





## ABSTRACT

To develop a basis for a nondestructive test method for heterogeneous solids such as concrete, analytical, numerical, and laboratory studies of transient stress wave propagation in solid plates and in plates containing flaws are presented. The technique, which is referred to as the impact-echo method, involves introducing transient stress waves into a test object by mechanical point impact and monitoring reflections of the waves from internal defects and external boundaries using a point receiver located close to the impact point.

Exact Green's function solutions for a point source on an infinite plate are used to study the response of a plate to elastic impact by a sphere in both the time and frequency domains. Displacement and stress fields produced by a transient point load on the top surface of an elastic plate are obtained using the finite element method. The finite element solution is verified by comparison to Green's function solutions.

The finite element method is used to study transient wave propagation in plates containing a flat-bottom hole or planar disk-shaped flaws. The finite element solution for the flat-bottom hole is verified by comparison to an experimental waveform. The numerical studies demonstrate the power of the finite element method for studying stress wave propagation within solids having arbitrary shapes, boundary conditions, and applied loads, and containing defects.

The development (instrumentation and signal processing) of an experimental impact-echo technique for finding flaws within plain and steel reinforced concrete is described. Laboratory results are presented; observations drawn from the analytical and numerical studies are used to aid in understanding experimental results. Successes achieved in the laboratory suggest that the impact-echo method has the potential to become a reliable field technique for detecting flaws within concrete structures.

**KEYWORDS:** concrete; finite element method; flaw detection; Green's function; nondestructive testing; stress wave propagation



## ACKNOWLEDGMENTS

The authors are grateful to Dr. Nelson N. Hsu of NBS for providing insight into problems involving transient stress wave propagation and signal processing, for performing the experiment that led to Fig. 6.8(a), and for providing the Green's function solutions for the response of an infinite plate that were used in Chapters 4 and 5.

The authors also thank Mr. Thomas M. Proctor and Dr. Edward Magrab of NBS for helpful discussions and for reviewing parts of this report, and Dr. John O. Hallquist of Lawrence Livermore National Laboratory for providing the finite element code which was used for the numerical studies presented in Chapters 4 and 6.



# TABLE OF CONTENTS

	Page
List of Tables .....	x
List of Figures .....	xi
CHAPTER 1: INTRODUCTION .....	1
1.1 Introduction .....	1
1.2 Objectives and Scope of Research .....	2
1.2.1 Objectives .....	2
1.2.2 Scope .....	2
CHAPTER 2: BACKGROUND .....	5
2.1 Basic principles of elastic wave propagation .....	5
2.1.1 Wave types .....	5
2.1.2 Wave velocity .....	6
2.1.3 Reflection and refraction .....	8
2.1.4 Diffraction at a crack tip .....	12
2.1.5 Attenuation and divergence .....	12
2.2 Stress pulses created by elastic impact .....	14
2.2.1 Hertz theory of elastic impact .....	14
CHAPTER 3: REVIEW OF PREVIOUS APPLICATIONS OF ECHO TECHNIQUES TO CONCRETE .....	21
3.1 Introduction .....	21
3.2 Test Methods .....	21
3.2.1 Through-transmission method .....	22
3.2.2 Echo methods .....	22
3.2.3 Resonance method .....	23
3.3 Past applications .....	24
3.3.1 Pavements and bridge decks .....	24
3.3.2 Erosion cavities under slabs and behind walls .....	26
3.3.3 Dams .....	27
3.3.4 Piles .....	28
3.3.5 Reactor structures .....	29
3.3.6 Refractory concrete .....	30
3.3.7 Surface opening cracks in submerged structures .....	30
3.4 Summary .....	31



CHAPTER 4: A FINITE ELEMENT STUDY OF TRANSIENT WAVE PROPAGATION IN PLATES .....	32
4.1 Introduction .....	32
4.2 Background .....	33
4.2.1 Transient wave propagation .....	33
4.2.2 Green's function solutions .....	34
4.2.3 Finite element method .....	36
4.3 Plate Response .....	38
4.3.1 Epicenter response .....	40
4.3.1.1 Green's function solutions .....	40
4.3.1.2 Comparison with finite element solution .....	43
4.3.2 Displacement fields within a plate .....	45
4.3.3 Impact-Echo response .....	48
4.3.3.1 Green's function solutions .....	49
4.3.3.2 Comparison with finite element solutions .....	50
4.4 Summary .....	51
CHAPTER 5: FREQUENCY SPECTRUM ANALYSIS OF THEORETICAL IMPACT-ECHO WAVEFORMS .....	58
5.1 Introduction .....	58
5.2 Frequency Analysis .....	58
5.3 Frequency Spectra of Analytical Waveforms .....	60
5.3.1 Frequency content of the impact .....	60
5.3.2 Frequency analysis of infinite plate response .....	64
5.3.2.1 Contact time of the impact .....	64
5.3.2.2 Test configuration .....	67
5.3.3 The effect of clipping or removing the R-wave signal .....	69
5.4 Conclusions .....	71
CHAPTER 6: A FINITE ELEMENT STUDY OF THE INTERACTION OF TRANSIENT STRESS WAVES WITH PLANAR FLAWS .....	79
6.1 Introduction .....	79
6.1.1 Brief review of the use of numerical methods for NDT applications .....	80



6.2	Background .....	82
6.3	Plate with a flat-bottom hole .....	84
6.3.1	Displacement response at the center of the hole .....	86
6.3.2	Displacement fields .....	88
6.3.3	Impact-Echo response .....	90
6.3.4	Comparison to experimental waveform .....	92
6.4	Planar disk-shaped flaws in plates .....	94
6.4.1	Flaw in aluminum .....	94
6.4.2	Flaws in concrete .....	96
6.4.2.1	Displacement waveforms .....	97
6.4.2.2	Displacement and stress fields .....	98
6.5	The effect of test variables on impact-echo waveforms .....	101
6.5.1	Contact time of the impact .....	101
6.5.2.	Ratio of flaw diameter to flaw depth .....	105
6.5.3	Test configuration .....	109
6.6	Summary and conclusions .....	111
CHAPTER 7: IMPLEMENTATION OF THE IMPACT-ECHO METHOD FOR FLAW DETECTION IN CONCRETE .....		130
7.1	Introduction .....	130
7.2	Development of a measurement technique .....	130
7.2.1	Impact sources .....	130
7.2.2	Transducer and filter .....	131
7.2.3	Oscilloscope .....	133
7.2.4	Concrete specimens .....	133
7.2.5	Signal acquisition and processing .....	135
7.2.6	Determining wave speeds through concrete ...	136
7.3	Waveforms and frequency spectra obtained from a solid plate .....	139
7.3.1	Contact time of the impact .....	139
7.3.2	Test configuration .....	141
7.4	Planar disk-shaped flaws in a plate .....	143
7.4.1	Effects of test variables on impact-echo waveforms .....	144
7.4.1.1	Contact time of the impact .....	145
7.4.1.2	Flaw diameter .....	147
7.4.1.3	Flaw depth .....	150
7.4.2	Sensitivity of the impact-echo method for detecting planar flaws .....	151



7.5	Flaws in reinforced concrete .....	154
7.5.1	Wave reflection from a concrete/steel interface .....	154
7.5.1.1	Wave reflection from a steel bar embedded in a concrete plate .....	157
7.5.2	Waveforms and frequency spectra obtained from a plate containing steel bars .....	158
7.5.3	Planar disk-shaped flaws in reinforced concrete .....	161
7.5.4	A simulated crack .....	163
7.6	Studies of other types of flaws .....	166
7.6.1	Depth of a surface opening crack .....	166
7.6.2	Flaw oriented at an angle to the surfaces of a plate .....	168
7.6.3	Grouted and ungrouted metal ducts .....	170
7.7	Summary and conclusions .....	173
CHAPTER 8: SUMMARY, CONCLUSIONS, AND FUTURE RESEARCH .....		206
8.1	Summary .....	206
8.2	Conclusions .....	207
8.2.1	Analytical and finite element studies .....	208
8.2.2	Laboratory studies .....	209
8.3	Future research .....	211
BIBLIOGRAPHY .....		213

## LIST OF TABLES

	Page
2.1 Specific acoustic impedances .....	17
2.2 Contact times, forces, and pressures produced by the impact of steel spheres on a concrete plate ...	17

## LIST OF FIGURES

	Page
2.1 Representative ray paths produced by impact on a plate .....	18
2.2 a) Spherical wavefronts produced by impact on the top surface of a plate; and, b) wavefronts after reflection from the bottom surface .....	18
2.3 The behavior of a P-wave incident upon an interface between two dissimilar media; a) reflection and refraction; and, b) mode conversion .....	19
2.4 Reflection coefficients at a concrete/air interface for an incident P-wave as a function of the incidence angle (Poisson's ratio = 0.2) .....	20
2.5 Reflection coefficients at a concrete/air interface for an incident S-wave as a function of the incidence angle (Poisson's ratio = 0.2) .....	20
4.1 Schematic representation of the wavefronts produced by point impact on a semi-infinite solid .....	52
4.2 Amplitude of particle displacements in the radiation pattern produced by a harmonic point source .....	52
4.3 Test configuration for a plate: a) epicenter; and, b) impact-echo .....	53
4.4 Epicenter response to a delta function impact .....	53
4.5 Epicenter response to impact: a) Green's function solution; and, b) waveform obtained from finite element analysis .....	54
4.6 Displacement and stress fields within a 0.5-m thick plate 125 $\mu$ s after the start of the impact; a) vector plot of displacements and the location of the waves; and, b) minimum principal stress contour plot .....	55
4.7 Vector plots of displacements at various times after the start of the impact: a) 148 $\mu$ s; b) 203 $\mu$ s; and, c) 250 $\mu$ s .....	56
4.8 Impact-echo response: a) Green's function solution; and, b) waveform obtained from finite element analysis .....	57

5.1	Example of a frequency spectrum obtained from a time domain waveform using the Fast Fourier Transform technique: a) digital time domain waveform; and, b) frequency spectrum .....	72
5.2	Stress pulse produced by the elastic impact of a sphere on the top surface of a plate. a) force-time function; and, b) Fourier transform .....	73
5.3	Half-cycle, sine-squared force-time function .....	74
5.4	Comparison of surface displacement waveforms for two force-time functions ( $H/T = 0.2$ and $t_c/t_{2P} = 0.25$ ): a) half-cycle, sine-squared function; and, b) half-cycle, sine function .....	75
5.5	The effect of contact time of the impact on the response of an infinite plate for $H/T = 0.2$ : a) $t_c/t_{2P} = 0.15$ ; b) $t_c/t_{2P} = 0.25$ ; and, c) $t_c/t_{2P} = 1.0$ .....	76
5.6	The effect of impact source - receiver spacing on the response of an infinite plate for $t_c/t_{2P} = 0.25$ : a) $H/T = 0.05$ ; b) $H/T = 0.2$ ; and, c) $H/T = 1.0$ .....	77
5.7	Effect on the frequency spectrum due to partially and completely removing the R-wave signal from the time domain displacement waveform shown in Figure 5a: a) R-wave signal clipped at an amplitude of -8.; and, b) R-wave signal completely removed .....	78
6.1	Diffraction at crack tips: a) P-ray incident on the edges of a crack; and, b) cylindrical wavefronts $P_dP$ and $P_dS$ emitted from edges .....	113
6.2	The important variables affecting the response of a planar disk-shaped void in a plate .....	114
6.3	Finite element model of a plate with a flat-bottom hole .....	114
6.4	Displacement waveforms obtained at the center of a flat-bottom hole and at the center of the bottom surface of a solid plate .....	115
6.5	Vector plots of the displacement fields in a plate with a flat-bottom hole: a) $6.1 \mu s$ after the start of impact; and b) $10 \mu s$ after the start of impact .....	116
6.6	Close-ups of vector plots of displacement fields around the flat-bottom hole at various times after the start of the impact: a) $12 \mu s$ ; b) $13.5 \mu s$ ; and, c) $15 \mu s$ .....	117

6.7	Impact-echo displacement waveforms obtained at the surface of a plate with a flat-bottom hole and at the surface of a solid plate .....	118
6.8	Comparison of analytical response with experimentally obtained response for a plate with a flat-bottom hole: a) experimental waveform; and, b) finite element waveform .....	119
6.9	Planar disk-shaped flaw in an aluminum plate: a) Displacement at center of the top surface of the flaw; and, b) Displacement at a point on the top surface of the plate .....	120
6.10	Planar disk-shaped flaw in a concrete plate: a) Displacement at center of the top surface of the flaw; and, b) Displacement at a point on the top surface of the plate .....	121
6.11	Displacement and stress fields in a plate containing a disk-shaped flaw 65 $\mu$ s after the start of the impact .....	122
6.12	Displacement and stress fields in a plate containing a disk-shaped flaw 80 $\mu$ s after the start of the impact .....	123
6.13	Displacement and stress fields in a plate containing a disk-shaped flaw 95 $\mu$ s after the start of the impact .....	124
6.14	Displacement and stress fields in a plate containing a disk-shaped flaw 125 $\mu$ s after the start of the impact .....	125
6.15	The effect on displacement waveforms caused by varying the contact time of the impact: a) 20 $\mu$ s; b) 40 $\mu$ s; and, c) 80 $\mu$ s .....	126
6.16	The effects on surface displacement waveforms caused by varying the diameter of a flaw. Flaw depth is 0.2 m. Flaw diameter is a) 0.05 m; b) 0.1 m; c) 0.2 m; and, d) 0.4 m .....	127
6.17	Surface displacement waveform obtained from a plate containing a 0.1 m diameter flaw located 0.4 m below the top surface of the plate .....	128
6.18	The effect on displacement waveforms of increasing the distance, H, between the impact point and the point where the surface displacement is measured: a) 0.025 m; b) 0.1 m; and, c) 0.15 m .....	129



7.1	Impactor with spring driven mass .....	177
7.2	NBS conical displacement transducer .....	177
7.3	0.2-m thick concrete plate containing steel bars: a) elevation view; and, b) plan view .....	178
7.4	0.5-m thick concrete plate containing polyurethane disks: a) plan view; and, b) elevation view .....	179
7.5	Formwork for 0.5-m thick concrete plate with disks in place prior to placement of concrete .....	179
7.6	Plan view of 0.5-m thick reinforced concrete plate containing artificial flaws .....	180
7.7	Formwork for 0.5-m thick reinforced concrete slab with flaws in place prior to placement of concrete .....	180
7.8	Test set-up: a) experimental set-up; and, b) schematic representation .....	181
7.9	Surface displacement waveform obtained from 0.25-m thick concrete plate showing computed wave arrival times .....	182
7.10	Waveforms and frequency spectra obtained from the 0.25-m thick concrete plate using various duration impacts: a) 34 $\mu$ s; b) 48 $\mu$ s; and, c) 90 $\mu$ s .....	183
7.11	Waveforms and frequency spectra obtained from the 0.25-m thick concrete plate for various distances between the impact point and the receiver: a) 0.025 m; b) 0.05 m; c) 0.125 m; and d) 0.25 m .....	184
7.12	Test configuration for tests carried out over planar disk-shaped flaws .....	185
7.13	Relationship between depth and frequency .....	185
7.14	Waveform and frequency spectrum obtained from 0.5-m thick concrete plate .....	186
7.15	Waveforms and frequency spectra obtained over a 0.2-m diameter disk-shaped flaw located 0.127 m below the top surface of the 0.5-m thick plate. Duration of the impacts was: a) 26 $\mu$ s; b) 40 $\mu$ s; and, c) 80 $\mu$ s .....	187
7.16	Waveforms and frequency spectra obtained over various diameter disk-shaped flaws located 0.25 m below the top surface of the 0.5-m thick concrete plate: a) 0.1-m diameter; b) 0.2-m diameter; and, c) 0.5-m diameter ....	188

7.17	Waveforms and frequency spectra obtained from flaws located at different depths in the 0.5-m thick concrete plate: a) 0.127 m; b) 0.258 m; c) 0.38 m; and d) bottom surface of the plate (0.5 m) .....	189
7.18	Summary of results of planar flaw studies based on frequency spectrum analysis .....	190
7.19	Wave reflection from concrete/air and concrete/steel interfaces .....	191
7.20	Waveforms and frequency spectra obtained from various diameter bars located 0.06 m below the top surface of the 0.2-m thick concrete plate; contact time of the impacts was 20 $\mu$ s: a) 2.54 cm; b) 3.81 cm; and, c) 4.45 cm .....	192
7.21	Waveforms and frequency spectra obtained from various diameter bars located 0.06 m below the top surface of the 0.2-m thick concrete plate; contact time of the impact was 54 $\mu$ s: a) 2.54 cm; b) 3.81 cm; and, c) 4.45 cm .....	193
7.22	Wavelength components of input pulses having a) 20 $\mu$ s contact time; and, b) 54 $\mu$ s contact time .....	194
7.23	Waveform and frequency spectrum obtained from a plain section of 0.5-m thick concrete plate containing a variety of flaws and reinforcing bars .....	195
7.24	Response obtained over a 0.35-m diameter flaw located 0.26 m below the top surface of the 0.5-m thick reinforced concrete plate: a) test configuration; and, b) waveforms and frequency spectrum .....	196
7.25	Response obtained over the 0.35-m diameter flaw shown in Figure 7.24 for a different test configuration: a) test configuration; and, b) waveform and frequency spectrum .....	197
7.26	Response obtained over a simulated crack in plain concrete: a) test configuration; and, b) waveform and frequency spectrum .....	198
7.27	Response obtained over a simulated crack in reinforced concrete: a) test configuration; and, b) waveform and frequency spectrum .....	199
7.28	Response obtained with impact point and receiver located on opposite sides of a vertical surface opening crack: a) test configuration; and, b) waveform and frequency spectrum .....	200

7.29	Schematic illustration of interaction of waves with vertical surface opening crack .....	201
7.30	Results obtained from a flaw oriented at a 30 degree angle to the surfaces of the 0.5-m thick plate .....	202
7.31	Waveforms and frequency spectra obtained at various points over the inclined flaw shown in Figure 7.30 .....	203
7.32	Responses obtained over hollow and grouted thin metal ducts for a contact time of 70 $\mu$ s: a) test configuration and results for hollow duct; and, b) test configuration and results for grouted duct .....	204
7.33	Responses obtained over duct for a contact time of 25 $\mu$ s: a) waveform and frequency spectrum for hollow duct; and, b) waveform and frequency spectrum for grouted duct .....	205



# CHAPTER 1

## INTRODUCTION

### 1.1 INTRODUCTION

For more than thirty years, efforts have been made to apply stress wave propagation to nondestructive testing of concrete. These efforts have met with limited success, although some progress has been made in measuring the thickness of plate elements and for integrity testing of piles. Progress has been limited because of the heterogeneous nature of concrete, which strongly attenuates high frequency waves; thus, traditional wave propagation methods developed for flaw detection in metals cannot be used for evaluation of concrete.

The research project that led to this report was aimed at developing a basis for a nondestructive test method for finding flaws within concrete using transient stress waves. The method that has been developed is referred to as the impact-echo method. The technique involves introducing a transient stress pulse into a test object by mechanical impact and monitoring surface displacements caused by the arrival of reflections of the pulse from internal defects and external boundaries.

The impact-echo test is a simple procedure; however, successful interpretation of the displacement waveforms requires an understanding of the interaction of transient stress waves with internal defects. The current state of knowledge about the propagation of transient stress waves in bounded solids containing

defects is very limited. Thus this study has focused on understanding the nature of transient stress wave propagation in solids containing defects, as well as on the development of an impact-echo method for finding flaws within concrete structures.

## 1.2 OBJECTIVES AND SCOPE OF RESEARCH

Following is a statement of the main objectives and the scope of the research work that is presented in this report.

### 1.2.1 Objectives

The objectives of this report are:

- 1) to study the displacement and stress fields created by transient point impact on an elastic solid;
- 2) to gain an understanding of transient elastic stress wave propagation in solid plates and in plates containing planar flaws; and,
- 3) to develop a method (testing technique and signal processing) for finding flaws within hardened concrete which is based on the generation and reception of transient stress waves.

### 1.2.2 Scope

Chapter 2 presents a brief review of the basic principles of elastic wave propagation. Values for wave speeds, reflection and attenuation coefficients are given for concrete. The Hertz theory of elastic impact is reviewed and applied to the impact of a steel sphere on a large concrete plate.

Chapter 3 presents a review of the previous applications of stress wave propagation techniques for evaluating concrete structures.

Chapter 4 discusses transient stress wave propagation in solid plates. The finite element method is used to study the displacement and stress fields generated by a transient point load on a plate. The validity of the finite element method for modeling transient wave phenomenon in elastic solids is established by comparing surface displacement waveforms obtained from finite element analyses to exact Green's function solutions for impact on an infinite plate.

In Chapter 5, the Fast Fourier Transform technique is used to compute the frequency content of 1) stress pulses generated by impact and 2) theoretical surface displacement waveforms obtained from the Green's function solution for an infinite plate. The effects on displacement waveforms and their corresponding frequency spectra due to changes in the duration of the impact and due to changing the test configuration (spacing between the impact point and the point where the displacement is calculated) are studied. The effect on the frequency spectrum of clipping or removing the Rayleigh wave signal is shown.

Chapter 6 presents a finite element study of the interaction of transient stress waves with planar flaws. The primary focus of this study is to determine the effects on displacement waveforms caused by waves diffracted from the sharp edges of a flaw. Displacement and stress fields within plates containing flat-bottom

holes and planar disk-shaped flaws are presented. The finite element solution is verified by comparing a surface displacement waveform obtained from the analysis of a plate containing a flat-bottom hole with an experimentally obtained waveform. To show the effect of important test variables on surface displacement waveforms, the results of parameter studies of plates containing planar disk-shaped flaws are presented. The variables studied included the duration of the impact, the diameter and the depth of a flaw, and the point where the displacement is monitored.

Chapter 7 discusses the development of an impact-echo technique for finding flaws within concrete. Results obtained from a variety of controlled flaw studies (simulated flaws in plain and reinforced concrete specimens) are presented. Observations and conclusions drawn from the analytical studies presented in the previous chapters are used to help interpret experimental waveforms and frequency spectra.

Chapter 8 summarizes important conclusions and discusses ongoing and future work and related applications.

## CHAPTER 2

### BACKGROUND

The purpose of this chapter is to provide background information on elastic wave propagation in solids and on the Hertz theory of elastic impact. This chapter is intended to provide basic background for those unfamiliar with stress wave propagation in solids.

#### 2.1 BASIC PRINCIPLES OF ELASTIC WAVE PROPAGATION

##### 2.1.1 Wave Types

There are three primary modes of stress wave propagation through isotropic, elastic media: dilatational, distortional, and Rayleigh waves. Dilatational and distortional waves, commonly referred to as compression and shear waves, or P- and S-waves, are characterized by the direction of particle motion with respect to the direction the wavefront is propagating. In a P-wave, motion is parallel to the direction of propagation; in the S-wave, motion is perpendicular to the direction of propagation. P-waves can propagate in all types of media; S-waves can propagate only in media with shear stiffness, i.e., in solids. Where there is a solid/liquid or a solid/gas interface, Rayleigh waves (R-waves) can propagate along the interface. In an R-wave, particle motion is retrograde elliptical. The amplitude of motion in the R-wave decreases exponentially with distance away from a free boundary [13]. The



shape of the P-, S-, and R-wavefronts depends upon the characteristics of the source that is used to generate the waves. There are three idealized types of wavefronts: planar, spherical, and cylindrical. When the stress waves are generated by a point source applied normal to the top surface of a plate, the resulting P- and S-wavefronts are spherical and the R-wavefront is circular.

### 2.1.2 Wave Velocity

The propagation of transient stress waves through a heterogenous bounded solid, such as a structural concrete member, is a complex phenomenon. However, a basic understanding of the relationship between the physical properties of a material and the velocity of wave propagation can be acquired from the theory of wave propagation in infinite isotropic elastic media [86].

In infinite elastic solids, the P-wave velocity,  $C_p$ , is a function of Young's modulus of elasticity,  $E$ , the mass density,  $\rho$ , and Poisson's ratio,  $\nu$  :

$$C_p = \sqrt{\frac{E (1 - \nu)}{(1 - \nu)(1 - 2\nu)}} \quad (2.1)$$

In bounded solids, such as thin plates or long rods, P-wave velocity can vary depending on the dimensions of the solid relative to the component wavelength(s) of the propagating wave. For rod-like structures, such as piles, P-wave velocity is independent of Poisson's ratio if the rod diameter is much less than the component wavelength(s) of the propagating wave [5]. In this case,  $C_p$  is

given by the following equation:

$$C_P = \sqrt{\frac{E}{\rho}} \quad (2.2)$$

For a Poisson's ratio of 0.2, a typical value in concrete, the P-wave velocity is five percent higher in an infinite solid than in a long thin rod.

The S-wave velocity,  $C_S$ , in an infinite solid is given by the following equation:

$$C_S = \sqrt{\frac{E}{2 \rho (1 + \nu)}} = \sqrt{\frac{G}{\rho}} \quad (2.3)$$

where  $G$  = shear modulus of elasticity.

A useful parameter is the ratio of the S- to P-wave speeds:

$$\frac{C_S}{C_P} = \sqrt{\frac{(1 - 2 \nu)}{2 (1 + \nu)}} \quad (2.4)$$

For Poisson's ratio of 0.2, the ratio of the S- to P-wave velocity is 0.61.

Rayleigh waves propagate at a velocity,  $C_R$ , which can be determined from the following approximate formula [92]:

$$C_R = \frac{0.87 + 1.12 \nu}{1 + \nu} C_S \quad (2.5)$$

For Poisson's ratio of 0.2, the R-wave velocity is 92 percent of the S-wave velocity.

P- and R-wave velocities are related by the following equation:

$$C_R = \frac{0.87 + 1.12 \nu}{1 + \nu} \sqrt{\frac{(1 - 2 \nu)}{2 (1 + \nu)}} C_P \quad (2.6)$$

Thus, if Poisson's ratio is known, the measured R-wave velocity can be used to estimate the P-wave velocity [83]. For Poisson's ratio of 0.2, the R-wave velocity is 56 percent of the P-wave velocity.

Wave velocity,  $C$ , frequency,  $f$ , and wavelength,  $\lambda$ , are related by the following equation:

$$C = f \lambda \quad (2.7)$$

Transient waves generated by a point source are composed of a range of frequencies; therefore, they contain a number of different wavelengths. The frequency content of transient waves is discussed in detail in Chapter 5.

### 2.1.3 Reflection and Refraction

When a P- or S-wavefront is incident upon an interface between dissimilar media, "specular" reflection occurs. (The term specular reflection is used since the reflection of stress waves is similar to the reflection of light by a mirror.) Stress waves can be visualized as propagating along ray paths and the geometry of ray reflection is analogous to that of light rays. Representative ray paths are shown in Fig. 2.1. The path of the R-wave is denoted by an R, and the paths of variously reflected P- and S-rays are denoted by a P or an S. For example, the 2P-ray (or PP-ray) represents a P-ray incident upon and reflected by an interface. The shape of the reflected wavefront can be determined by considering the reflection of individual rays. Fig. 2.2(a) illustrates the propagation of P-, S-, and R-wavefronts generated by point impact



on a plate. In Fig. 2.2(b), incident rays OA and OB are reflected as rays AC and BD, and it is seen that the reflected rays behave as though they were radiating from virtual point O'. Thus, the reflected wavefronts (2P and 2S) are also spherical.

At a boundary between two different media only a portion of a stress wave is reflected. The remainder of the wave penetrates into the underlying medium (wave refraction), as shown in Fig. 2.3a. The angle of refraction,  $\beta$ , is a function of the angle of incidence,  $\theta$ , and the ratio of wave velocities,  $C_2/C_1$ , in the different media, and is given by Snell's Law [79]:

$$\sin \beta = \frac{C_2}{C_1} \sin \theta \quad (2.8)$$

Unlike light waves, stress waves can change their mode of propagation when striking the surface of a solid at an oblique angle [85]. Incident P-waves can be partially reflected as both P- and S-waves and can be refracted as both P- and S-waves, depending on the angle of incidence. Since S-waves propagate at a lower velocity than P-waves, they will reflect and refract at angles (determined using Snell's Law),  $\theta_s$  and  $\beta_s$ , that are less than the angles of reflection and refraction for P-waves, as shown in Fig. 2.3(b).

The relative amplitudes of reflected waves depend upon the mismatch in specific acoustic impedances at an interface, the angle of incidence, the distance of an interface from the pulse source, and the attenuation along the wave path. The influence of each of these factors is considered in the following discussion.

The portion of an incident plane P-wave that is reflected

at an interface between two media of different densities or elastic moduli depends on the specific acoustic impedances of each medium. The specific acoustic impedance,  $Z$ , of a medium is

$$Z = \rho C_p \quad (2.9)$$

Since  $C_p$  is approximately equal to  $\sqrt{E/\rho}$  ;

$$Z = \sqrt{E \rho} \quad (2.10)$$

Specific acoustic impedance values for P-waves in selected materials are given in Table 2.1. Eq. (2.9) is also valid for S-waves if the S-wave velocity is used to calculate acoustic impedance.

The amplitude of particle motion in a reflected ray,  $A_r$ , is maximum when the angle of incidence of the ray is normal to the interface and is determined from the following equation [5]:

$$A_r = A_I \frac{(Z_1 - Z_2)}{(Z_1 + Z_2)} \quad (2.11)$$

where  $A_I$  is the amplitude of motion in the incident ray.

Coefficients of reflection for the amplitude of a reflected wave as a function of the angle of incidence can be determined using the formulas in Ref. [48], which are applicable for plane waves incident upon plane boundaries. These formulas were used to calculate the reflection coefficients for a concrete/air interface. Fig. 2.4 shows reflection coefficients for an incident P-wave, and Fig. 2.5 shows reflection coefficients for an incident S-wave. It is assumed that each incident wave has an amplitude equal to unity. Each figure is composed of three graphs. The graph in the upper left gives the reflection coefficients for the wave with the same mode as the incident wave; for example in Fig. 2.4, which is

for an incident P-wave, the upper left graph shows the reflection coefficients for a reflected P-wave. The graph in the lower right gives the reflection coefficients for the mode-converted wave. The lower right graph in Fig 2.4 shows the reflection coefficients for the S-wave produced by the mode conversion of the incident P-wave. The graph in the upper right gives the angular relationship between the incident wave and the mode-converted wave, which is determined by Snell's Law. The drawing in the lower left gives an illustrative example.

In the previous discussion it was assumed that reflection and refraction of wavefronts occurred at planar interfaces between two dissimilar media. This type of analysis is also applicable to flaws or discontinuities within a medium.

The ability of stress wave propagation methods to detect flaws or discontinuities (sensitivity) depends on the component frequencies (or wavelengths) in the propagating wave and on the size of the flaw or discontinuity. A general rule is that waves will diffract or bend around the edges of discontinuities if the size of the discontinuity is on the order of or less than the component wavelengths in the propagating wave. Therefore, to detect flaws on the order of 0.1 m, it is necessary to introduce into the concrete (P-wave velocity of 4000 m/s) a stress pulse that contains frequencies greater than approximately 20 KHz (wavelengths less than approximately 0.1 m).

#### 2.1.4 Diffraction at a Crack Tip

When a stress pulse is incident upon a crack tip (or the sharp edge of a discontinuity) diffracted waves are produced. These waves are spherical and they originate at the crack tip. Mode conversion of the incident wave also occurs at the crack tip, producing a second diffracted wave. For example, a P-wave incident upon a crack tip produces a diffracted P-wave and a diffracted S-wave.

#### 2.1.5 Attenuation and Divergence

As a wave propagates through a solid the acoustic pressure (and thus the amplitude of particle motion) decreases with path length due to attenuation (scattering and absorption) and divergence.

In a heterogeneous solid, scattering is the result of wave reflection, refraction, diffraction, and mode conversion at each interface between dissimilar media. In ordinary concrete the density and the elastic modulus of the coarse aggregates are generally higher than those of the mortar; thus, from Eq. (2.10), the specific acoustic impedance of the coarse aggregate is higher than that of the mortar. If the wavelength of the propagating wave is less than the size of the aggregate, this mismatch in impedances causes scattering of the incident wave as the waves undergo reflection and refraction from each mortar-aggregate interface [83]. For higher quality concrete the specific acoustic impedance of the mortar approaches that of the coarse aggregate and scattering is reduced. (Quality in this context refers to the density and elastic modulus



of the mortar phase. Higher quality is synonymous with higher density and greater elastic modulus or both.) In evaluation of concrete, lower frequency waves must be used (i.e., the wavelength to aggregate size ratio must be increased [84]) to reduce the attenuation of wave energy due to scattering. However, use of lower frequency waves reduces the sensitivity of the propagating wave to small flaws. Thus, there is an inherent limitation in the flaw size that can be detected within concrete.

Although attenuation of wave energy in heterogeneous solids is primarily due to scattering, part of the wave energy is absorbed and turned into heat (hysteretic damping) [85]. In solids damping is mainly caused by internal friction.

Attenuation also affects the frequency content of the pulse propagating in a heterogeneous medium [75]. Pulses produced by point impact contain a range of frequencies. In a material such as concrete, the higher frequency components of the propagating pulse will be preferentially attenuated with path length. As a result, the frequency spectrum of the pulse is continuously shifted to lower frequencies. Thus, both the sensitivity and the acoustic pressure of a pulse decrease with path length.

For non-planar waves, reduction of the acoustic pressure also occurs due to spreading of the wavefront as it propagates through the test medium (divergence) [79]. For a point source producing a spherical wavefront, divergence causes the pressure to vary as the inverse of the distance from the source [5].

The path of a received signal includes both the incident

path (source to flaw) and the reflected path (flaw to receiver). Both incident and reflected waves undergo attenuation and divergence; thus, the amplitude of the signal decreases with total path length. The relative losses caused by attenuation and divergence will depend upon the attenuation coefficient of both the test medium and the frequency content of the propagating wave [48].

## 2.2 STRESS PULSES CREATED BY ELASTIC IMPACT

Electro-acoustic transducers and mechanical impact are the two common methods used to introduce a stress pulse into a test object. The selection of a pulse source for a specific application depends upon the size of the flaws to be detected and on the characteristics of the test medium. In the inspection of metals, high frequency, short-duration, pulses are introduced into a test object by an electro-acoustic transducer. No commercial transducers are satisfactory for pulse-echo testing of concrete; thus, a mechanical impact source normally is used to generate a stress pulse with sufficient acoustic energy to overcome the effects of attenuation and divergence. The type of impact source that is used determines the energy and frequency content of the stress pulse.

### 2.2.1 Hertz Theory of Elastic Impact

Impact is defined as the collision of two solids. In this report, this collision involves the impact of a small diameter steel sphere dropped onto the surface of a large concrete plate. The duration of this impact is short, ranging from approximately 20

to 90 us. During the impact a portion of the potential energy in the sphere is transferred to elastic wave energy in the plate.

The force-time function resulting from the elastic impact of a sphere on a solid can be approximated as a half-cycle sine curve.

$$F = F_{\max} \sin \pi \frac{t}{t_c} \quad 0 \leq t \leq t_c \quad (2.12)$$

where  $F_{\max}$  = the maximum force (N); and  
 $t_c$  = contact time of the impact (s).

The amplitude of this force-time function,  $F_{\max}$ , affects the magnitude of stresses and displacements that occur in the stress waves generated by impact. The contact time affects the frequency content of the pulse.

The contact time of an impact produced by dropping a steel sphere on a concrete slab can be approximated by the Hertz elastic solution for a sphere dropped onto a thick plate [28]:

$$t_c = 5.97 [\rho_s (\delta_s + \delta_p)]^{0.4} \frac{R}{(h)^{0.1}} \quad (2.13)$$

$$\delta_p = \frac{1 - \nu_p^2}{E_p} \quad (2.14)$$

$$\delta_s = \frac{1 - \nu_s^2}{E_s} \quad (2.15)$$

where  $\rho_s$  = density of the sphere ( $\text{kg/m}^3$ );  
 $R$  = radius of the sphere (m);  
 $h$  = drop height (m);  
 $\nu_p$  = Poisson's ratio for the plate;  
 $\nu_s$  = Poisson's ratio for the sphere;  
 $E_p$  = Young's modulus of elasticity for the plate ( $\text{N/m}^2$ ); and  
 $E_s$  = Young's modulus of elasticity for the sphere ( $\text{N/m}^2$ );

For a steel sphere dropped onto a concrete slab ( $E_p = 36 \times 10^9 \text{ N/m}^2$  and  $\nu_p = 0.2$ ):

$$t_c = 0.00858 \frac{R}{(h)^{0.1}} \quad (2.16)$$

This relationship indicates that the contact time is a linear function of the sphere radius and is only slightly affected by drop height. As will be discussed in Chapter 7, the contact time of the impact of a steel sphere on concrete may be slightly longer than that predicted by elastic theory due to inelastic behavior of the concrete.

The maximum deformation, force, and pressure occur at  $t_c/2$ . The maximum force is given by the following equation:

$$F_{\max} = \frac{1.140 (v_o)^2 m_s}{\alpha_m} \quad (2.17)$$

$$\alpha_m = \left[ \frac{15 \pi v_o^2}{16 (R)^{0.5}} (\delta_s + \delta_p) m_s \right]^{0.4} \quad (2.18)$$

where  $m_s$  = mass of the sphere (kg).

The maximum contact pressure is:

$$P_{\max} = 0.2515 \left[ \frac{v_o^2 m_s}{(\delta_s + \delta_p)^4 (R)^3} \right]^{0.2} \quad (2.19)$$

where  $g$  = acceleration of gravity ( $\text{m/s}^2$ );  
 $v_o$  = velocity of the sphere at impact ( $\text{m/s}$ ).

Since the mass of a sphere is a function of the radius cubed,  $P_{\max}$  is independent of sphere size. Table 2.2 gives contact times and maximum contact forces resulting from the elastic impact of 4 to 16 mm diameter steel spheres dropped 0.2 m onto a concrete slab. The maximum contact pressure in this case is 1675 MPa.



TABLE 2.1 Specific Acoustic Impedances

Material	Density (kg/m <sup>3</sup> )	P-Wave Velocity (m/s)	Specific Acoustic Impedance (kg/(m <sup>2</sup> -s))	Ref.
Air	1.205	343	0.413	14
Concrete*	2300	3000 - 4500	6.9 - 10.4 x 10 <sup>6</sup>	-
Granite	2750	5500 - 6100	15.1 - 16.8 x 10 <sup>6</sup>	6
Limestone	2690	2800 - 7000	7.5 - 18.8 x 10 <sup>6</sup>	6
Marble	2650	3700 - 6900	9.8 - 18.3 x 10 <sup>6</sup>	6
Quartzite	2620	5600 - 6100	14.7 - 16.0 x 10 <sup>6</sup>	6
Soils	1400 - 2150	200 - 2000	0.28 - 4.3 x 10 <sup>6</sup>	9
Structural Steel	7850	5940	46.6 x 10 <sup>6</sup>	48
Water	1000	1480	1.48 x 10 <sup>6</sup>	48

\*The mass density of concrete depends on the mix proportions and the specific gravities of the mix ingredients. The given density is for an average, normalweight concrete.

TABLE 2.2 Impact of a Steel Ball on a Concrete Plate

Sphere Diameter (m)	Maximum Force (N)
0.004	86.75
0.006	195.18
0.008	346.98
0.010	542.16
0.012	780.71
0.014	1062.63
0.016	1387.93

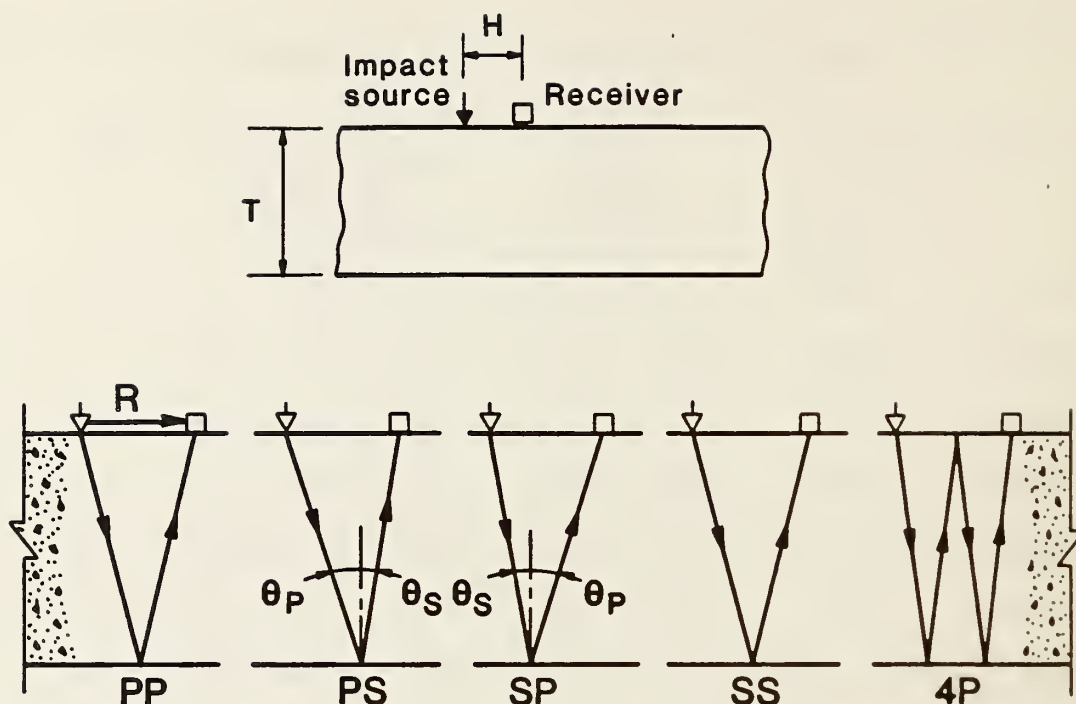


Figure 2.1 Representative ray paths produced by impact on a plate.

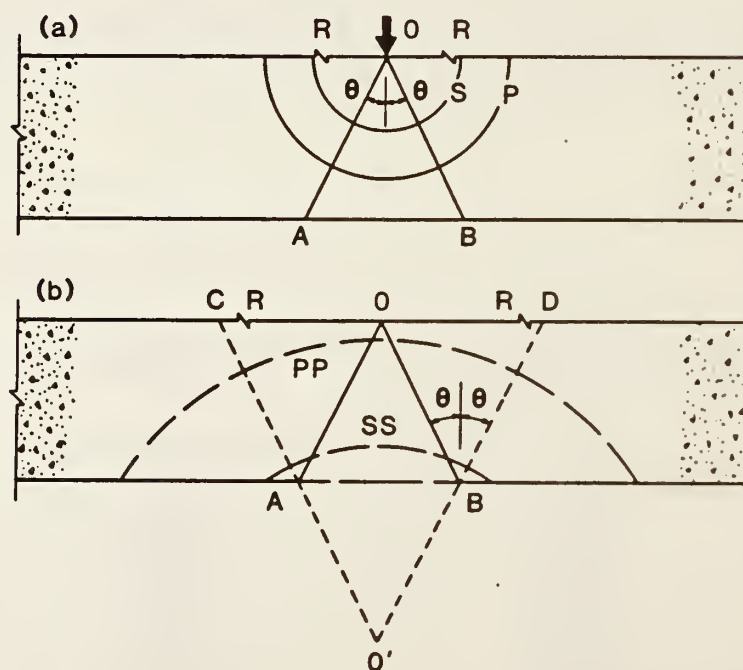
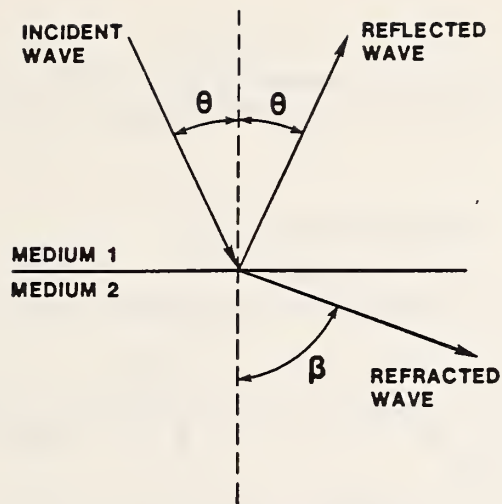
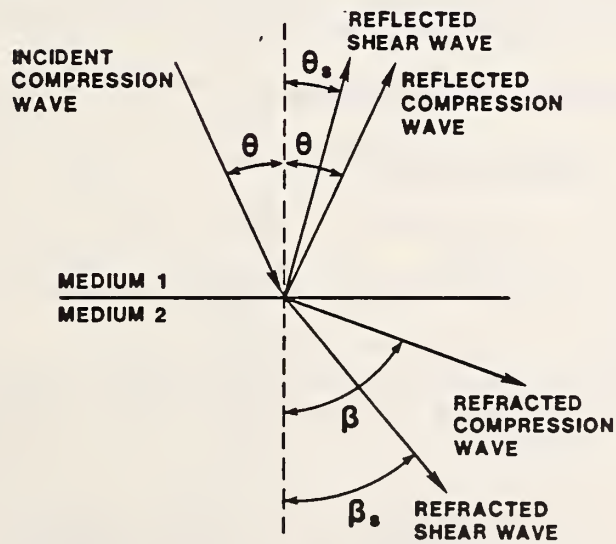


Figure 2.2 a) Spherical wavefronts produced by impact on the top surface of a plate; and, b) wavefronts after reflection from the bottom surface.



$$\frac{\sin \theta}{c_1} = \frac{\sin \beta}{c_2}$$

a) Reflection and Refraction



$$\frac{\sin \theta}{c_{p1}} = \frac{\sin \beta}{c_{p2}} = \frac{\sin \theta_s}{c_{s1}} = \frac{\sin \beta_s}{c_{s2}}$$

b) Mode Conversion

Figure 2.3 The behavior of a P-wave incident upon an interface between two dissimilar media; a) reflection and refraction; and, b) mode conversion.

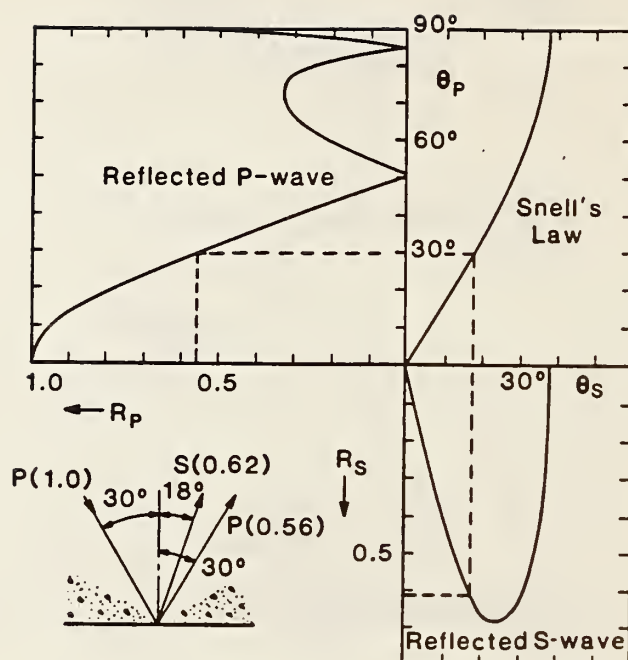


Figure 2.4 Reflection coefficients at a concrete/air interface for an incident P-wave as a function of the incidence angle (Poisson's ratio = 0.2).

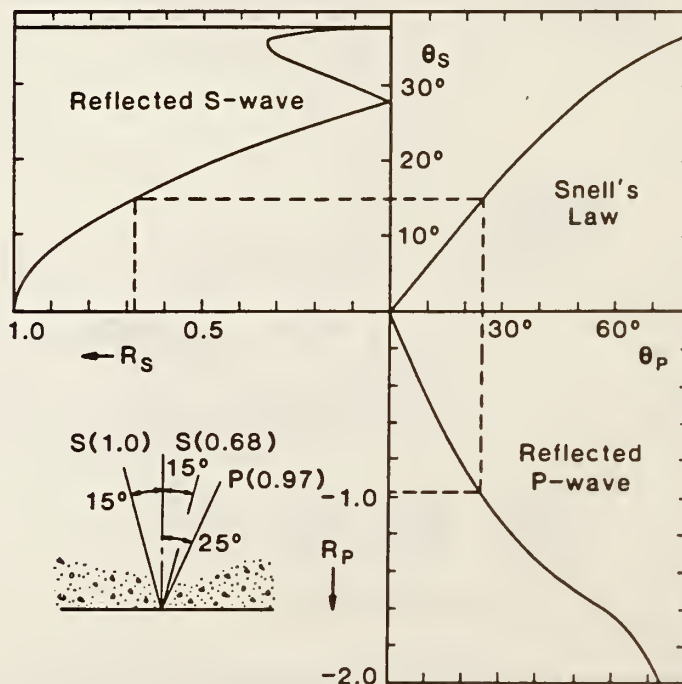


Figure 2.5 Reflection coefficients at a concrete/air interface for an incident S-wave as a function of the incidence angle (Poisson's ratio = 0.2).

## CHAPTER 3

### REVIEW OF PAST APPLICATIONS OF ECHO METHODS TO CONCRETE

#### 3.1 INTRODUCTION

With the exception of visual inspection, the use of acoustic methods is the oldest form of nondestructive testing. Striking an object with a hammer and listening to the "ringing" sound is a common way of detecting the presence of internal voids, cracks, or delaminations.

In 1929, Sokolov of Russia first suggested the use of ultrasonic waves to find defects in metal objects [85]. However, it was not until the nearly simultaneous introduction of pulse-echo flaw detectors in 1942 by Firestone of the University of Michigan and by Sproule of England that significant progress was made. Since that time, ultrasonic pulse-echo testing of metals, plastics, and other homogeneous materials has developed into an efficient, reliable, and versatile nondestructive test method. The development of test techniques and equipment for evaluation of less ideal materials, such as concrete, has been hindered by the difficulties inherent in obtaining and interpreting a signal record from a heterogeneous material.

#### 3.2 TEST METHODS

There are a variety of techniques that are based on using stress wave propagation for nondestructive testing. The primary

distinctions between the techniques are in the methods used for generating and receiving the stress waves. Three methods that have been used for evaluation of concrete are: 1) the through-transmission (pulse-velocity) method; 2) echo methods; and 3) the resonance method. These methods are discussed in the following sections.

### 3.2.1 Through-Transmission Method

In the through-transmission (or pulse-velocity) method, one measures the time it takes for a stress pulse to travel from a transmitting transducer to a receiving transducer located on the opposite side of a test object. From the measured travel time and the known distance between transducers, an apparent pulse velocity is calculated. The computed pulse velocity value can be used to draw inferences about the integrity of the medium. This approach has its limitations: it requires two accessible surfaces and it offers no indication as to the cause of any differences among pulse velocity values in different parts of a structure. Because of these limitations, applications of this technique will not be discussed.

### 3.2.2 Echo Methods

In the echo methods a stress pulse is introduced into the test medium at an accessible surface by a transmitter or by mechanical impact. If a transmitter is used, the method is referred to as a pulse-echo technique; if mechanical impact is used, the method is referred to as an impact-echo technique. The pulse propagates through the medium and is reflected by material defects



or by interfaces between phases of different densities or elastic moduli. These reflected waves, or echoes, are monitored by either the transmitter acting as a receiver (true pulse-echo) or by another receiving transducer coupled to the surface of the test object near the pulse source (pitch-catch). The transducer output is displayed on an oscilloscope. Using the time base of the display, the travel time of the pulse can be determined. If the wave velocity in the medium is known, the round-trip travel time of each echo can be used to determine the location of a defect or an interface.

### 3.2.3 Resonance Method

Resonance techniques are used to determine the thickness or length of a test object. Continuous waves are introduced into a test object by a transmitter or a mechanical oscillator. The frequency of these waves is systematically varied until a resonance condition is set up in a test object. Resonance occurs when the driving frequency is equal to the frequency of the fundamental mode of vibration of the test object. The response of the test object is monitored by a receiving transducer which is located close to the transmitter. When a resonance condition is achieved, there is a significant increase in the amplitude of the measured response. The fundamental mode of vibration is identified by noting the frequency,  $f$ , at which this increase occurs. If the P-wave velocity in the test object is known, the thickness of the test object,  $t$ , which equals one-half the wavelength of the propagating waves, can be calculated.

### 3.3 PAST APPLICATIONS

The three stress wave propagation methods discussed in Section 3.1 have been used for detecting very large structural cracks in concrete dams, for integrity testing of slender concrete structures, such as piles, for measuring the thickness of plate elements, such as highway slabs, and for several other specialized applications. These applications are reviewed in the following section.

#### 3.3.1 Pavements and Bridge Decks

Resonance and echo techniques have been developed to measure the thickness of concrete pavements and to detect delaminations in bridge decks. In the early 1960's, Muenow [57] developed a technique to measure pavement thickness which was based on determining the frequency of the fundamental mode of vibration of the slab in the thickness dimension. A transmitter was used to excite resonances in the slabs.

Resonance methods have also been used to detect delaminations in concrete bridge decks. A technique developed in 1973 by researchers at Texas A & M University [56] used an oscillating steel plunger to excite the characteristic vibrations of a delaminated area. As the plunger oscillates at 60 Hz, the vibrations of the bridge deck were monitored by a receiving transducer. The location and extent of delaminated areas could be determined from the relative amplitudes of the received signals. The use of this technique has been limited by the fact that it cannot be used where concrete decks have asphaltic overlays exceeding approximately 5 cm.

In 1964, Bradfield and Gatfield [11] of England reported the development of an echo technique for measuring the thickness of concrete pavements. Using two 100 kHz resonant transducers (16 cm tall, 10 cm wide, and 25 cm long) in a pitch-catch arrangement, they were able to measure the thickness of a 12-inch concrete specimen with an accuracy of 2 percent. However, this system could not be field tested [38] due to the impracticality of the test set-up. Besides being bulky, the transducers were coupled to the concrete by a large plastic block which required a smooth flat concrete surface for good coupling. Difficulties were also reported in obtaining reflections from the bottom of rough textured pavement surfaces.

In 1968, Howkins, et al., at IIT Research Institute [38] independently investigated available resonance and echo techniques in an attempt to identify a feasible method for pavement thickness measurements. Tests using the resonance technique proposed by Muenow [57] and the echo technique proposed by Bradfield and Gatfield [11] were performed. Although it was felt that the resonance technique was, in principle, a good approach, significant reservations were stated concerning the reliability of Muenow's resonance method. Using an echo technique similar to that developed by Bradfield and Gatfield, the IIT researchers were able to measure the thickness of 7 and 10-inch thick portland cement concrete slab specimens, for both simply supported slabs and slabs supported on a 4-inch thick gravel base course, and 5-inch thick, simply supported bituminous concrete slab specimens with an accuracy of  $\pm 2$  percent.

However, it was concluded that the transducer arrangement was not practical for field use.

An echo system was developed at Ohio State university in the late 1960's [52] to measure pavement thickness by monitoring the travel time for an ultrasonic pulse to propagate through the thickness of the concrete and return to the receiving transducer at the top surface after being reflected by the concrete pavement-subbase interface. A large transmitter was needed to introduce sufficient acoustic energy into the test medium to overcome wave attenuation problems due to coarse-grained aggregates and to obtain coherent reflections from rough pavement-subbase interfaces. The transmitter was a hollow cylinder, with a 46 cm outer diameter, a 15 cm inner diameter, and a 200 kHz resonant frequency. The receiving transducer was placed in the center of the transmitter. Accuracies of plus or minus 3 percent at more than 90 percent of the test locations were obtained. The accuracy and good performance of the Ohio State thickness gage was confirmed in independent field tests conducted in 1976 by Weber, Gray, and Cady [88]. However, Weber, et al., concluded that the Ohio State instrument needed to be redesigned to better withstand the rigors of field use before it could be considered as practical nondestructive testing equipment.

### 3.3.2 Erosion Cavities Below Slabs and Behind Walls

Yamshchikov, Sidorov, Baukov, and Potapov of Russia [93] used an acoustic resonance technique for finding large erosion cavities behind concrete canal walls and below reinforced concrete



slabs on soil substrates. In the case studies presented, the canal walls were 18 to 23 cm thick and the reinforced concrete slab was 10 cm thick. The resonance technique used was an adaptation of a standard technique in the USSR for checking bonds in multilaminate plastic structures; this technique is referred to as the Method of Free Vibrations [50]. Flexural modes of a wall or a slab were excited by the periodic impact of an electromechanical vibrator operating at a frequency of 16 Hz. The response of the wall or slab was monitored by an accelerometer, and a spectral analyzer was used to obtain the frequency spectrum of the received signal. The presence of a cavity was detected by monitoring the change in the amplitude of the frequencies corresponding to the thickness of the slab. When a cavity was present, there was a noticeable increase in amplitude. Cavities approximately 2 m and larger were detected.

### 3.3.3 Dams

Engineers in India [58] used an impact-echo method to estimate the depth and extent of large horizontal cracks that developed in Koyna dam during a major earthquake in 1967. Very low frequency stress waves (200-600 Hz) were introduced into the concrete by mechanical impact with a free falling steel hammer. This range of frequencies allowed detection of cracks on the order of 15 m and larger. The energy generated by the mechanical impact was sufficient to obtain reflections from cracks located 100 m away from the point of impact. After existing cracks were grouted, the



impact-echo technique was used to assess the degree of grout penetration. The assessment was made qualitatively by comparing the echo amplitudes in signal records obtained before grouting to those obtained after grouting.

#### 3.3.4 Piles

Since the early 1970's, impact-echo and resonance techniques have been widely used for integrity testing of concrete piles [3, 12, 24, 25, 36, 37, 61, 62, 67, 81, 83, 90]. The behavior of stress waves in slender, rod-like structures, such as piles, is well known. If a pulse is generated by mechanical impact at one end of the rod, the resulting wavefront is initially spherical but quickly becomes planar as the pulse propagates down the long slender rod. Plane wave reflection occurs at the bottom surface, and the reflected wavefront travels back up the length of the rod to be picked up the receiving transducer. Thus, the rod acts as a waveguide. Because of the length of piles, long duration impacts can be used. As a result, signal analysis is relatively simple.

Steinbach and Vey [83] were among the first to apply impact-echo techniques to field evaluation of piles. A pulse was introduced into a concrete pile at the top surface by mechanical impact and returning echoes were monitored by an accelerometer mounted on the same surface. The signal record could then be used to detect partial or complete discontinuities, such as voids, abrupt changes in cross section, very weak concrete, and soil intrusions, as well as the approximate location where such irregularities

existed. In the absence of major imperfections the location of the bottom of a sound pile could be determined. However, little specific information could be obtained as to the extent of defects or the relative soundness of concrete at the location of an irregularity. The success of the method is dependent upon the damping characteristics of the surrounding soil; a high degree of damping can severely weaken returning echoes.

Resonance methods have also been widely used for integrity testing of piles and to determine pile performance under load and to gain information about the soils surrounding the pile. The first resonance method for integrity testing of piles was developed in France by Paquet in 1968. Since that time, the use of resonance methods for testing of piles has become widespread. Techniques for evaluating the integrity of piles, determining pile performance under load, and gaining information about soils surrounding piles are discussed in detail in Refs. [37, 62, and 81].

### 3.3.5 Reactor Structures

In 1976, Sutherland and Kent [84] of Sandia Laboratories used an ultrasonic pulse-echo method to measure the thickness of concrete reactor substructures subjected to the thermal energy of a hypothetical core meltdown. Two transducers were used in the pitch-catch mode. The relative position of a concrete-gas interface subjected to a high heat flux from a plasma jet was monitored as a function of time to determine the erosion rate of the concrete substructure.

### 3.3.6 Refractory Concrete

Claytor and Ellingson [16] used an echo method to measure the thickness of 30.5 cm thick refractory concrete specimens. It was found that for frequencies below 100 kHz, the use of a single transducer as both the transmitter and receiver was impractical because the ringing of the transmitter obscured the echo signal. Tests were also carried out using two transducers in a pitch-catch arrangement; however, the transmitting transducer generated strong R-waves which interfered with the reception of the echo signal by the receiving transducer. To reduce R-wave interference, large diameter (17.8 cm) transducers were constructed. As the response of a transducer is an averaged phenomenon over the contact area, the sensitivity of a larger diameter transducer to localized surface disturbances (R-waves) was reduced.

### 3.3.7 Surface Opening Cracks in Submerged Structures

Smith [80] demonstrated that Rayleigh waves can be used to detect surface opening cracks in submerged concrete structures, such as concrete tanks and offshore structures. Two 0.5 MHz, 25-mm diameter, P-wave transducers were used as transmitter and receiver. When a transmitted P-wave strikes the surface of a solid at a critical angle (defined by Snell's Law), mode conversion occurs producing a R-wave which propagates along the solid-liquid interface. As the R-wave propagates, mode conversion also occurs, producing a P-wave which radiates into the liquid at the same critical angle and is picked up by the receiving transducer. The

distance between the two transducers can be adjusted to optimize the amplitude of the received signal. If the path of the propagating R-wave is crossed by a crack, reflection occurs and no signal will be picked up by the receiving transducer. If a crack is favorably oriented (a crack at 90 degrees to the propagating wave is the best orientation), the P-waves produced by mode conversion of the reflected R-wave will be picked up by the transmitting transducer. Analysis of the received signals obtained from a complete scan, i.e., from moving the transducers parallel to and over the surface of the test object in a prearranged pattern, allowed the location of surface opening cracks to be determined.

### 3.4 SUMMARY

A review of the literature shows that resonance and echo methods have been used successfully to detect the thickness of concrete slabs and to detect voids beneath slabs or behind walls. Delaminations within bridge decks and large cracks within dams have been detected. Impact-echo and resonance techniques have been widely used for integrity testing of concrete piles; the technique and the instrumentation for the evaluation of this type of structure are fairly well established. Although limited success has been achieved in other specialized applications, no standardized stress wave propagation method currently exists for general nondestructive evaluation of concrete structures.



## CHAPTER 4

### A FINITE ELEMENT STUDY OF TRANSIENT WAVE PROPAGATION IN PLATES

#### 4.1 INTRODUCTION

The propagation of waves in an infinite elastic plate has been studied since the work of Lord Rayleigh [70] and Lamb [49] in the late 1800's. The work of Miklowitz [55] on transient waves in elastic waveguides formed the first detailed study of transient wave propagation in elastic plates. Recently, due to the interest in the propagation of acoustic emission waves in elastic solids, the problem of a transient, normal point load on the surface of an infinite elastic plate has been studied. This is the problem that is of interest in this chapter. Solutions of this problem [15, 21, 41, 64, 69] have been obtained using generalized ray theory [63] in conjunction with Cagniard's method [63] or with the Fourier inversion technique [89], the method of superposition of normal modes [87], and classical integral transform methods [91].

In this chapter, the finite element method is used for the first time to study stress wave propagation in elastic plates subjected to transient, normal point loads. Surface displacement time-histories and internal displacement and stress fields are presented. To verify the analyses, surface displacement time histories obtained from the finite element method are compared to exact solutions obtained using generalized ray theory and the Fourier inversion technique. (In this report, solutions obtained using ray theory will be referred to as Green's function solutions.)



## 4.2 BACKGROUND

### 4.2.1 Transient Wave Propagation

Point impact on the surface of a solid gives rise to three types of disturbances: dilatational and distortional waves which propagate into the solid along spherical fronts, and a Rayleigh (R) wave which propagates along a circular front over the surface of the solid. The dilatational and distortional waves are commonly referred to as P- and S-waves. In addition, there is a low amplitude wave known as a head wave. The front of the head wave extends from the intersection of the P-wavefront with the surface of the solid to a point that is tangent to the S-wavefront. Fig. 4.1 is a schematic representation of the P-, S-, R- and head wavefronts generated by elastic impact on a solid.

Explicit equations for the radiation pattern produced by a transient point source on a semi-infinite solid have not yet been derived. Ideas about the nature of this radiation pattern come from knowledge about the far-field radiation patterns produced by a harmonic point source on a semi-infinite solid [53, 54, 71]. Fig. 4.2 shows the angular variation of the amplitude of displacements within the P- and S-waves for a material with a Poisson's ratio equal to 0.2. In the P-wave, the amplitude of the displacements is maximum along the centerline of the plate and decreases to zero at the surface. In the S-wave, the amplitude of displacements is zero at the centerline of the plate and at the surface and is maximum along a ray located approximately 37 degrees from the centerline. There is a discontinuity in the S-wave

displacements at an angle,  $\theta_c$ , given by the following equation:

$$\theta_c = \arcsin (C_s/C_p) \quad (4.1)$$

where  $C_s$  = S-wave speed; and  
 $C_p$  = P-wave speed.

In this chapter, the finite element method is used to study the internal displacement and stress fields produced by a transient point load on a plate. The displacement fields produced by a transient point load are compared to those shown in Fig. 4.2.

#### 4.2.2 Green's Function Solutions

Theoretical solutions for transient wave propagation in solids are available for a limited number of problems; these solutions can be used to obtain the displacement response at a single point in a solid. The displacement,  $u(r,t)$ , at a point due to an impact at some other point, a distance  $r$  away on an elastic body, can be obtained by knowing the impulse response function of the body,  $G(r,t)$ , and the force-time function of the impact,  $F(t)$ . The impulse response is called the dynamic Green's function of the elastic body. This Green's function is defined as the impulse (dirac delta function) response of the body for a particular impact configuration (impact at one location and the receiver at a different location). The response of the body for an arbitrary force-time function can be found by solving the following convolution integral:

$$u(r,t) = \int_{-\infty}^{\infty} G(r, t - \tau) F(\tau) d\tau \quad (4.2)$$

Since the delta function is causal, from the condition of causality, the impulse response is also causal [65]. Thus,

$$G(r, t - \tau) = 0 \quad \tau > t \quad (4.3)$$

so that Eq. (4.2) becomes:

$$u(r, t) = \int_{-\infty}^t G(r, t - \tau) F(\tau) d\tau \quad (4.4)$$

The force-time function,  $F(\tau)$ , is also causal; thus,

$$F(\tau) = 0 \quad \tau < 0 \quad (4.5)$$

and Eq. (4.2) reduces to Duhamel's Integral [65]:

$$u(r, t) = \int_0^t G(r, t - \tau) F(\tau) d\tau \quad (4.6)$$

Thus, Eq. 4.2 is reduced to a definite integral which can be solved numerically using a digitized form of  $G(r, t)$ .

The Green's function solution is the exact solution to the partial differential equation and associated boundary conditions governing transient elastic wave propagation. The solution is in the form of an infinite series expansion which is referred to as a generalized ray expansion. Stress waves can be visualized as propagating along ray paths. Each term in the series corresponds to the arrival of successive stress waves which propagate along the various ray paths that connect the impact source to the receiver. For a given time duration, a finite number of rays (terms in the series expansion) contribute to the total displacement response at the receiver.

Explicit formulae for Green's function solutions which are amenable to numerical computations have been derived only for simple geometries, such as a semi-infinite space or an infinite plate. (For computation of the Green's function, see Refs. [15, 42, 64].)

The Green's function solution for an infinite plate is applicable to a finite plate for the duration of time prior to the arrival of the first wave reflected from the sides of the plate. To obtain displacement and stress fields in bounded plates, the finite element method was used.

#### 4.2.3 Finite Element Method

The finite element method is a numerical technique for obtaining approximate solutions to the partial differential equations that arise from boundary value problems. The method involves dividing a continuum into a finite number of discrete parts - the finite elements. The discretized representation of the continuum is referred to as the finite element model. For stress analysis, the behavior of each element is described by a set of assumed functions which represent the variation of displacements or stresses within that element. Variational principles are used to formulate force-displacement element equations. These element equations are then used to construct the global equations which describe the behavior of the entire continuum. Solution of these global equations gives the displacements or stresses at points in the element [26].

An explicit, two-dimensional (axisymmetric or plane strain), finite element code (DYNA2D), developed at Lawrence Livermore Laboratory for solving finite-deformation, dynamic contact-impact problems [29, 32, 33], was used to perform the studies discussed in this report. An input generator (MAZE) [34] was used to create the finite element model. A mini-computer with a virtual operating



system, 8 MBytes of memory, and a floating point processor was used to carry out the analyses.

In DYNA2D, a continuum is divided into elements using constant strain (or linear displacement) triangles and quadrilaterals [32]. Higher order elements (e.g., linear strain, quadratic strain) are not available in DYNA2D because they are computationally expensive in wave propagation applications compared to the use of constant strain elements. For a particular element type, element size determines the accuracy of the finite element solution. In wave propagation problems, the optimum element size depends on the geometry of the continuum and on the characteristics of the dynamic loading. For the constant strain quadrilaterals and the dynamic loading functions used in the plate analyses presented in this chapter, studies were carried out to determine the optimum element size. Comparisons were made between finite element displacement time-histories obtained at points on the top and bottom surfaces of a plate and the waveforms obtained at the same points by the Green's function solution for an infinite plate. For 0.25- to 0.5-m thick plates subjected to a force-time function which simulated impact by a steel sphere (contact time of impact was 25 to 31  $\mu$ s), rectangular elements with dimensions on the order of 0.02 times the plate thickness were found to give accurate results. The elastic material properties used in the analyses were representative of concrete.

In dynamic finite element analyses, numerical integration of the equations of motion must be carried out; DYNA2D uses the central



difference method [32] to accomplish this integration. The central difference method requires a small time step for numerical stability. This is not a drawback since wave propagation applications require very small time steps to obtain an accurate solution and to capture the true dynamic response. Numerical stability requires that the time step,  $h$ , meets the following criterion:

$$h \leq h_{\max} = L / C_p \quad (4.7)$$

where  $L$  = shortest dimension of the element, m; and  
 $C_p$  = P-wave speed in the material, m/s.

In DYNA2D, the time step is taken as  $0.67h_{\max}$  unless the user specifies some other value. During an analysis, data are stored in data files at intervals specified by the user. In the analyses discussed in this chapter, data were stored every  $2 \mu\text{s}$ . An interactive graphic post-processor (ORION) [35] was used to process the results of the analyses.

Before the finite element code could be used with confidence to study transient wave propagation in bounded solids containing internal flaws, solutions obtained by the method were verified using Green's function solutions for infinite plates.

### 4.3 PLATE RESPONSE

The successful implementation of the impact-echo technique as a method for flaw detection in heterogeneous materials, such as concrete, requires an understanding of the reflection of transient stress waves by the free boundaries of a solid and the interaction of waves with internal defects. A first step is understanding the

response of an infinite plate to impact. In the following discussion of the elastic response of a plate to point impact on the top surface, the following analytical results are presented: 1) the displacement time-history obtained at the bottom surface of the plate directly under the impact point; 2) displacement fields recorded at successive times to show transient stress waves propagating within the plate; and 3) the displacement time-history of a point on the top surface of the plate near the point of impact.

For the case of a sphere impacting on a plate, Eq. (4.6) can be used to predict the surface displacement that will be detected by a receiving transducer located on either the top or bottom surface of the plate. Two test configurations are considered in this study; these are shown in Fig. 4.3. Fig. 4.3(a) shows the receiver located at the epicenter, that is, on the bottom surface of the plate directly under the point of impact. Fig. 4.3(b) shows the impact-echo configuration - the receiver is located on the top surface of the plate near the point of impact. For this configuration, the separation between impact point and receiver is denoted by  $H$ .

The time-history of the contact force generated by the elastic impact of a sphere dropped on the surface of a plate can be approximated by a half-cycle sine curve (see Fig. 4.1). If the appropriate Green's function,  $G(r,t)$ , is known, then the displacement,  $u(r,t)$ , can be computed by numerical solution of the convolution integral given by Eq. (4.6) [10].

In this study, the Green's function for a unit step, force-time

function on an infinite plate was obtained using a computer code recently developed at NBS [21, 39]. This program computes the response for a unit step force-time function input. To obtain the Green's function (impulse response), the derivative with respect to time of the step function solution is calculated. The step function response is calculated using nondimensionalized variables so that the solutions are applicable to a plate of any thickness. Values of the step function response are calculated at prescribed time steps so that the computer solution is a discretized representation of the true solution. The only input parameters required are the source-receiver geometry and the ratio of S- to P-wave speeds. In the analyses presented in this paper, the ratio was 0.61 (Poisson's ratio equal to 0.2).

#### 4.3.2 Epicenter Response

##### 4.3.2.1 Green's Function Solutions

Before considering the response of a plate to impact by a sphere, the impulse response is shown. In the impulse response, wave arrivals correspond to abrupt discontinuities in the waveform. It is therefore easier to determine the displacements caused by each individual wave arrival.

Since the numerical solution used in this study results in a discrete representation of the step function response, the derivative of this solution (the impulse response) also has a discrete representation.

The impulse response for a 0.25-m thick plate is shown in Fig.

4.4. The P- and S-wave speeds are 4000 and 2440 m/s, respectively. A time step of 1  $\mu$ s was used in the calculations. This response consists of normal surface displacements caused by the arrival of direct P- and S-waves, multiply reflected waves (3P, 3S, 5P, etc) and mode-converted waves (2PS, P2S, etc.). The arrival times of these waves are indicated on the waveform.

The P-wave generated by impact on the top surface of the plate is the first wave to arrive at the epicenter; it is a compression wave (a wave causing compressive stress at the wavefront) and it causes a large downward displacement of the surface. This compression wave will be reflected at the bottom surface of the plate (free boundary) as a tension wave. The tension wave will propagate back up through the plate to be reflected at the top surface as a compression wave. (The multiply-reflected P-wave is now called the 3P-wave because when it arrives at the bottom of the plate it will have traveled through the thickness of the plate three times.) When the 3P-wave arrives at the bottom surface it pushes the surface downward. This cycle is repeated so that every multiply-reflected P-wave arriving at the bottom surface of the plate (5P, 7P, etc.) is a compression wave and causes a downward displacement of the plate surface.

Notice that the amplitude of the surface displacements caused by successive P-wave arrivals decreases. This is due to divergence (spherical beam spreading).

Theoretically, an S-wave arriving at the epicenter has no vertical displacement component (see Fig. 4.2). However, the arrival



of the S-wavefront is still easy to identify because the arrival of the wavefront corresponds to a rapid upward movement of the downwardly displaced bottom plate surface.

The waveform obtained from the Green's function solution for a point located a distance  $r$  from an impulse point source in an infinite solid shows displacements produced by the arrivals of the P- and S-wavefronts. No other displacements occur. However, in the impulse response of the infinite plate (Fig. 4.4), notice that in addition to the displacements caused by P-, S-, and mode-converted waves, there are displacements that occur between the arrivals of each of these waves. These intermediate displacements are referred to in this report as "wakes"; they result from the transient point source being applied normal to a stress-free boundary.

To obtain the epicenter response caused by a sphere impacting the top surface of the plate, the waveform shown in Fig. 4.4 must be convolved with the force-time function shown in Fig. 4.1 (Eq. (2.12)). Using the identity for the derivative of convolution, a mathematically equivalent approach is to convolve the response computed for a unit step function,  $H(r,t)$ , with the derivative of the force-time function,  $d[F(t)]/dt$  [10]. This approach is numerically more accurate in this case. Thus Eq. (4.6) can be written in the following form:

$$u(r,t) = \int_0^t H(r,t - \tau) \frac{dF(\tau)}{d\tau} d\tau \quad (4.8)$$

The waveform obtained by this convolution is shown in Fig. 4.5(a). The time step used in these calculations was 2  $\mu$ s.



In this analysis, the contact time of the impact was 31  $\mu\text{s}$ , which is equal to one-half the time required for a P-wave to travel from the impact point to the epicenter. The waveform generated by a 31  $\mu\text{s}$  point impact is much smoother than the impulse response that was shown in Fig. 4.4. (Chapter 5 will present a more detailed discussion of the effect of contact time on surface displacement waveforms.)

The arrivals of P-, S-, and mode-converted wavefronts are indicated on the calculated waveform. The displacements caused by the large amplitude P-wave arrivals dominate the waveform. Notice that there is a second dip in the waveform after the end of the direct P-wave and before the arrival of the S-wavefront. The steady change in displacement (wake) between these two waves in the impulse function response (see Fig. 4.4) gives rise to this second dip.

#### 4.3.1.2 Comparison with Finite Element Solution

The impact response of the same plate was also calculated using an axisymmetric finite element model. In both the Green's function solution and the finite element analysis the plate was unsupported. Impact on the top surface of the plate was simulated by applying a uniform stress over an element at the center of the plate. The time history of the applied stress was a half-cycle sine curve with a duration of 31  $\mu\text{s}$ . The values of the material properties used in the analysis were: a modulus of elasticity of 33100 MPa, a Poisson' ratio of 0.2, and a density of 2300  $\text{kg/m}^3$ . These values result in P-, S-, and R-wave speeds of 4000, 2440, and 2240 m/s,

respectively. Fig. 4.5(b) shows the normal displacement at the epicenter of the plate. The computed arrival times of P-, S-, and mode-converted waves are indicated on the waveform.

The response obtained by the finite element analysis can be compared with the Green's function solution for an infinite plate for the period of time before wave reflections return from the sides of the bounded plate used in the finite element analysis. If the shape and magnitude of the perturbations in the waveform obtained from the Green's function solution (Fig. 4.5(a)) are compared with those in the waveform obtained from the finite element analysis, it is seen that there is good agreement between the two waveforms.

In the waveform obtained from the finite element analysis, there is a series of low amplitude, extraneous oscillations (ringing) between the back of the S-wave (128  $\mu$ s) and the arrival of the 3P-wavefront. This ringing is due to the excitation of spurious modes of vibration in the constant strain finite elements used in DYNA2D. These modes are referred to as "zero energy" or "hourglass modes" [29] and they are due to distortions of the elements. A decrease in the contact time of the impact causes more rapid changes in displacement; this causes greater distortion of elements and tends to increase ringing. Artificial viscosities are introduced in DYNA2D to damp out the ringing [23], but it generally cannot be completely suppressed. The ringing is particularly evident in this case because there is a relatively quiescent period between the rapid, large amplitude change in displacements which occurs prior to 128  $\mu$ s and the arrival of the 3P-wave.

#### 4.3.2 Displacement Fields within a Plate

A single finite element analysis solves for displacements and stresses over the entire domain (the collection of finite elements) at each time step during the specified time of analysis. These results can be used to study the dynamic displacement and stress fields that are produced within a solid.

An axisymmetric, finite element analysis was performed for a 25- $\mu$ s duration impact on a 0.5-m thick, 1.5-m diameter, unsupported, plate. Material properties were identical to those used in the previous analysis. A 0.5-m thick plate was used in this analysis so that the P- and S-waves generated by the 25  $\mu$ s impact became separated as they propagated through the plate; this makes the displacement fields created by the waves easier to study.

The right hand side of Fig. 4.6(a) shows the displacement field in the plate 125  $\mu$ s after the start of the impact. (Since the displacement field is axisymmetric, only half of the plate is shown.) At 125  $\mu$ s the P-wavefront arrives at the epicenter of the plate. The position of the P- and S-wavefronts are indicated the left hand side of the figure. The magnitude and direction of the average nodal displacement of each element is indicated by a vector. The relative lengths of the vectors depend on the magnitude of the largest displacement that occurs within the plate at a particular time. The vector lengths are also adjusted by a scale factor which is not under the user's control. Therefore, the vector plots shown in Figs. 4.6(a) and 4.7 are not drawn to the same scale; this must be remembered when comparing the figures.

As mentioned, particle motion in a P-wave is parallel to the direction of wave propagation. In Fig. 4.6(a), the vectors within the P-wave are oriented along rays emanating from the impact point. This orientation is consistent with the direction of motion. The magnitude of the displacements in the P-wave are not uniform along the spherical wave. Displacements are maximum near the centerline of the plate (ray connecting the impact point to the epicenter) and they diminish to almost zero at the top surface of the plate. This pattern of displacements is in agreement with that shown in Fig. 4.2.

The motion in an S-wave is perpendicular to the direction of wave propagation. In Fig. 4.6, the S-wave is easy to identify because of the orientation and large amplitude of the vectors within the wave. As expected, vectors are perpendicular to rays emanating from the impact point. Displacements along a spherical surface within the plate were studied to determine the effects caused by the S-wave. The displacements in the S-wave are approximately zero at the center of the plate and become larger along rays located at increasing angles from the centerline. A study of displacement time-histories obtained for various elements along a spherical front inside the plate showed that, near the critical angle (approximately 37 degrees from the centerline of the plate), there is a discontinuity in the displacements in the spherical S-wavefront. This discontinuity agrees with that predicted by the radiation pattern shown in Fig. 4.2. Near the surface, it is difficult to determine the amplitude of the displacements in the S-wave because



of interference due to the displacements caused by the R-wave. Note that in the vector displacement field all effects are superimposed; each vector represents the total displacement of any given element.

Fig. 4.6(b) shows a contour plot of minimum principal (compression) stress. The stresses in the P-wave are greatest at the centerline of the plate and decrease toward the surface. Since a state of pure shear stress is equivalent to a state of equal biaxial tension and compression, the plot of minimum principal stress also shows the stress variation in the S-wave. The stresses in the S-wave are lowest at the centerline and increase toward the surface. In the region near the surface of the plate, the stresses caused by the R-wave are superimposed upon those produced by the S-wave making it is difficult to separate the stresses caused by each wave.

The observed patterns of displacements and stresses in the P- and the S-waves is similar to those expected based on the displacement fields produced by a harmonic point source (Fig. 4.2). However, in addition to the these P- and S-wave radiation patterns, Fig. 4.6 shows that in the region between the P- and S-waves there are displacement and stresses that resemble those that occur in a P-wave; this is the "P-wake." There is also a region of nonzero displacements and stresses trailing the S-wave (the "S-wake") that resemble the patterns in the S-wave. Thus, the disturbances generated by impact on a plate are not confined in the P- and S-waves.



Figs. 4.7(a) through 4.7(c) show displacement fields obtained from the finite element analysis, along with corresponding representations of the positions of the P-, S-, and mode-converted waves, at 148, 203, and 250  $\mu\text{s}$  after the start of the impact.

The displacement field at 148  $\mu\text{s}$  (Fig. 4.7(a)), shows reflection of the P-wave at the bottom surface of the plate. The S-wave created by mode-conversion of the incident P-wave (referred to as the PS-wave) is not yet discernible as it is masked by the displacements caused by the reflected P-wave.

At 203  $\mu\text{s}$  (Fig. 4.7(b)), the S-wavefront arrives at the epicenter. The bottom surface of the plate is displaced downward at this time because of the effect of the preceding P-wave and P-wave wake. The S-wave wake is clearly visible.

At 250  $\mu\text{s}$  (Fig. 4.7(c)), the front of the reflected P-wave arrives at the top surface of the plate. The PS-wave is now easily discernible. Reflection of the S-wave is occurring and the mode-converted P-wave (referred to as SP) that was generated by the reflection of the incident S-wave is seen emerging from the front of the reflected S-wave.

Once multiple reflections of the P-, S-, and mode-converted waves begin to occur, the disturbances created by individual waves become more difficult to distinguish in the displacement fields.

#### 4.3.3 Impact-Echo Response

The use of the impact-echo method for nondestructive testing involves interpretation of displacement waveforms obtained near

the point of impact. In this section, a surface displacement waveform obtained from the Green's function solution for an infinite plate is compared with results obtained by the finite element method.

#### 4.3.3.1 Green's Function Solution

The normal displacement calculated at a point on the top surface of a infinite plate due to impact at another point on the same surface is shown in Fig. 4.8(a). The thickness,  $T$ , of the plate was 0.25 m. The spacing,  $H$ , between the impact point and the point where the displacement was calculated (the point where a receiving transducer would be located) was 0.05 m (see Fig. 4.3(b)). The ratio of the S- to the P-wave speed was 0.61 and the contact time of the impact was 31  $\mu$ s as in the epicenter analysis.

The waveform shown in Fig. 4.8(a) consists of displacements caused by the arrival of multiply reflected P- and S-waves and mode-converted waves. In addition, there is an initial large amplitude displacement caused by the R-wave propagating along the top surface of the plate. In the figure, the R-wave arrival is denoted by an R, and multiple P- and S-wave arrivals and mode-converted wave arrivals are indicated. For this particular test configuration ( $H/T = 0.2$ ), the normal displacements caused by the S-wave are very small.

As discussed previously, the P-waves which arrive at the top surface are tension waves; the arrival of each tension wave pulls the surface downward. Thus the perturbations in the impact-echo response have a pattern similar to the epicenter response.

#### 4.3.3.2 Comparison with Finite Element Solution

The displacement waveform obtained from the finite element analysis of the 0.25-m thick plate subjected to a 31  $\mu$ s duration impact is shown in Fig. 4.8(b). The spacing between the impact and the point where the waveform was recorded is 0.05 m as in the Green's function solution. Material properties are the same as those used in the previous analyses.

If the shape and relative magnitudes of the perturbations in the waveform obtained from the finite element analysis (Fig. 4.8(a)) are compared with those in the waveform obtained from the Green's function solution (Fig. 4.8(b)), it is seen that there is good agreement between the two waveforms.

As in the epicenter response obtained from the finite element analysis, low amplitude oscillations due to excitation of the zero energy modes of the finite elements occur in Fig. 4.8(b). After the R-wave has passed the receiver, the surface displacement should go to zero, as shown in Fig. 4.8(a), until reflections arrive from the bottom of the plate. However, the oscillations due to excitation of the zero energy modes cause the computed surface displacement to oscillate about zero for a short time. In this case, the zero energy modes are excited by the element distortion caused by the rapid, large amplitude changes in displacement that occur in the R-wave. This numerical ringing does not affect the displacement pattern due to the multiply reflected waves.

#### 4.4 SUMMARY

The internal displacement and stress fields produced by a transient point load on the top surface of an elastic plate were studied using the finite element method. It was shown that in addition to P- and S-waves, intermediate displacement and stress fields (waves) are produced by a transient point load applied normal to a stress-free boundary. Surface displacement waveforms computed by the finite element method showed good agreement with those obtained from the Green's function solution.

The study presented in this chapter has demonstrated the potential of the finite element method for becoming a powerful tool for understanding the interaction of stress waves with defects within solids. Such knowledge is essential for successful implementation of nondestructive testing techniques based on stress wave propagation, such as the impact-echo method. The power of the finite element method lies in its ability to analyze solids having arbitrary shapes, boundary conditions, and applied loads, and to generate complete pictures of displacement and stress fields in a computationally efficient manner.

Chapter 6 will present finite element studies of the diffraction of transient stress waves by flat-bottom holes and circular disks within plates - problems for which no Green's function solutions currently exist.



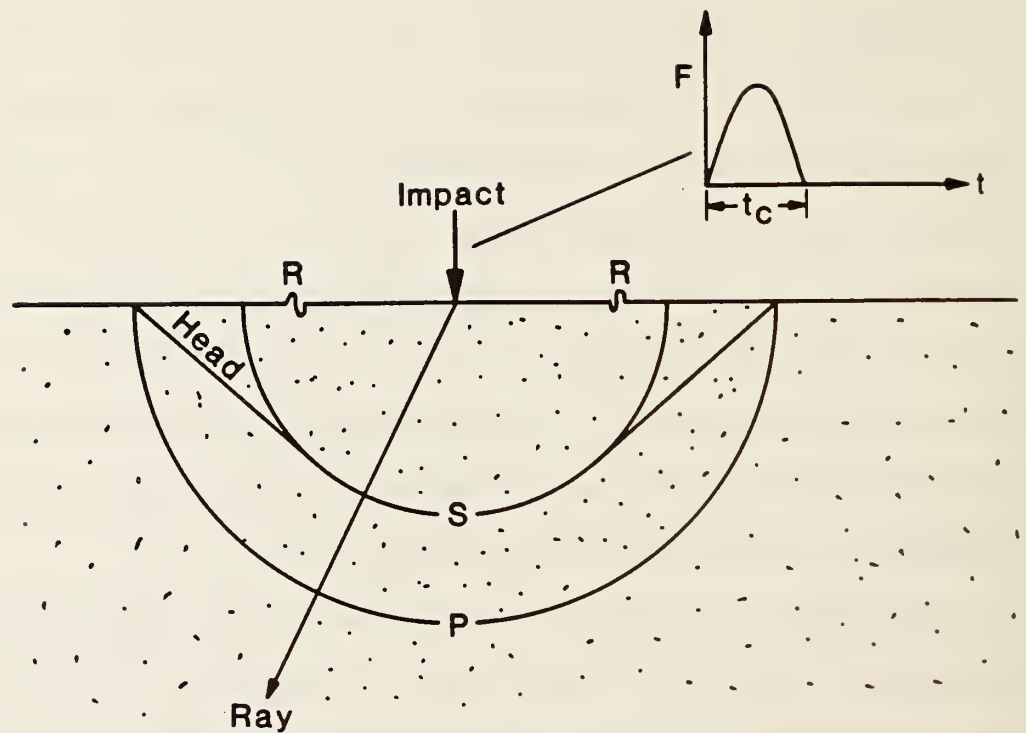


Figure 4.1 Schematic representation of the spherical wavefronts produced by point impact on a semi-infinite solid.

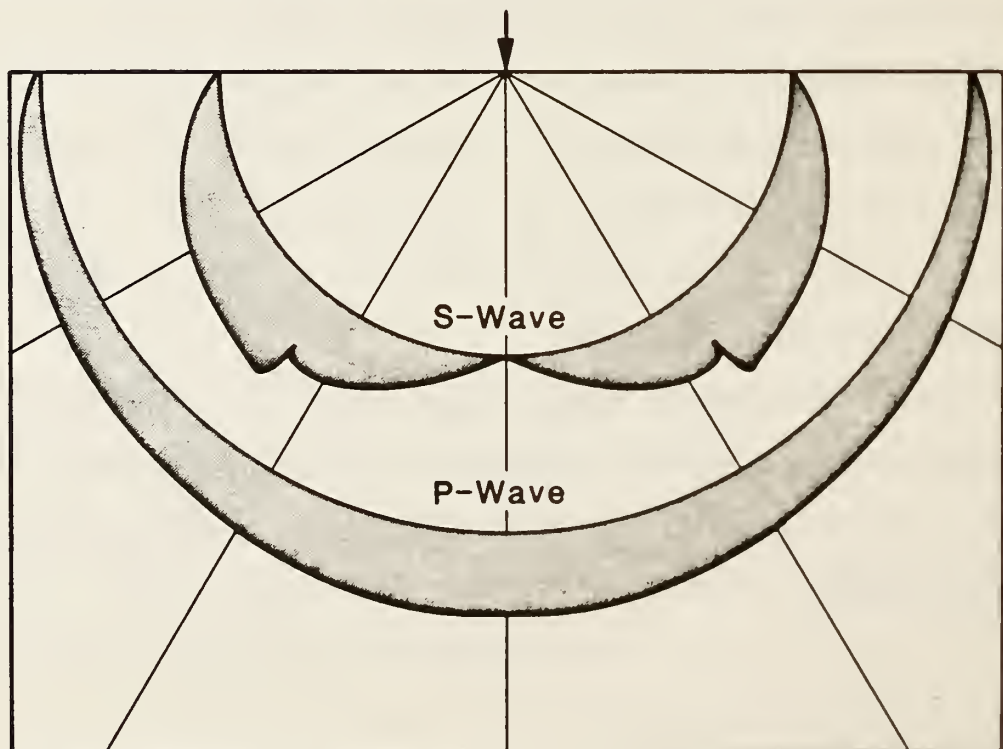


Figure 4.2 Amplitude of particle displacements in the radiation pattern produced by a harmonic point source.



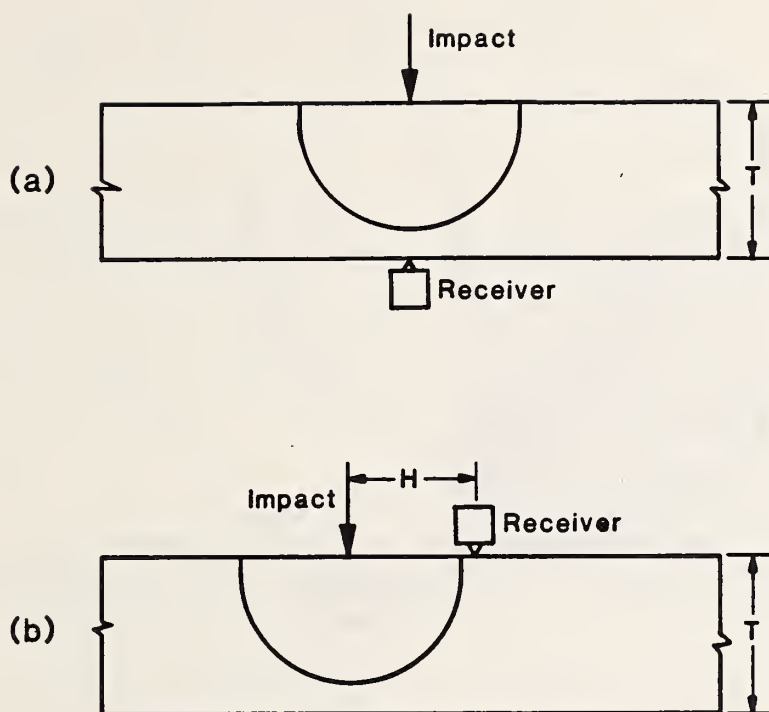


Figure 4.3 Test configuration for a plate: a) Epicenter; and b) Impact-Echo.

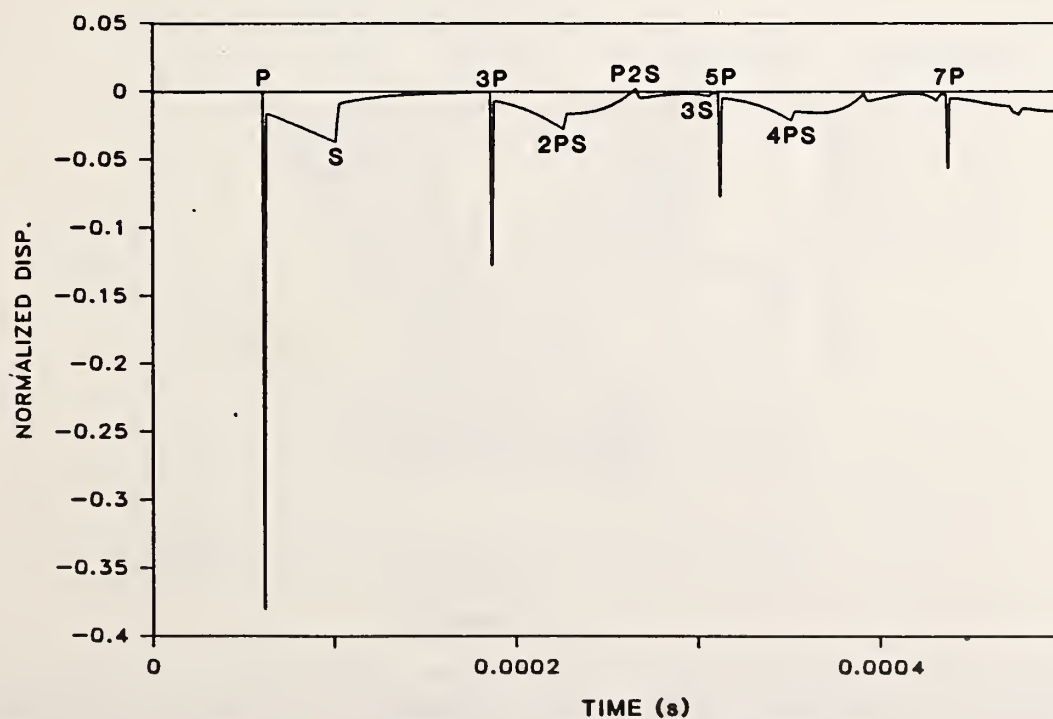


Figure 4.4 Epicenter response to a delta function impact.

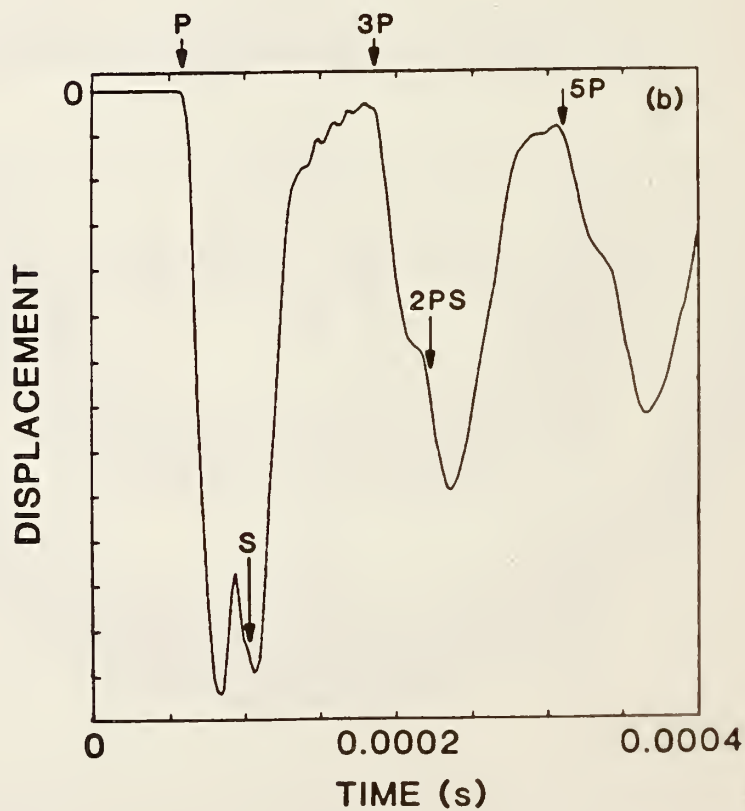
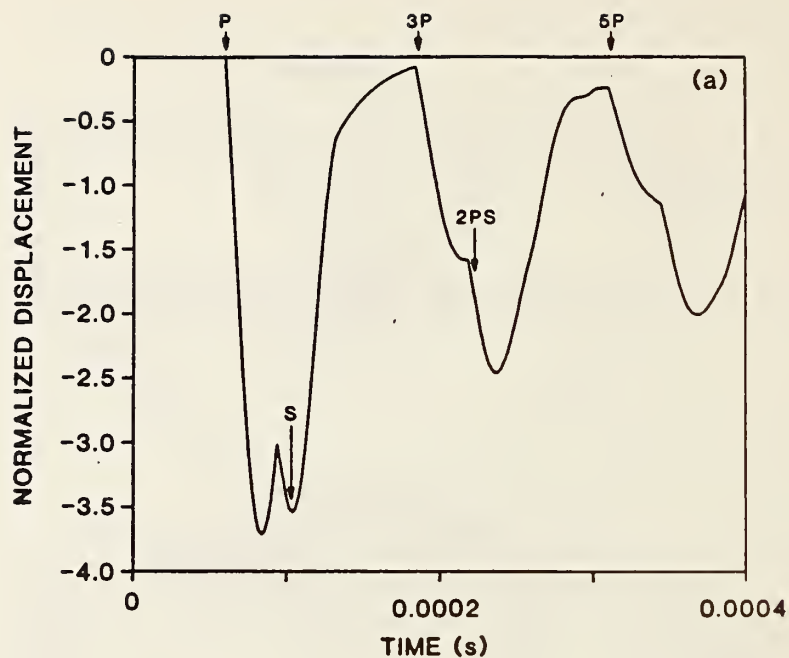


Figure 4.5 Epicenter response to impact: a) Green's function solution; and b) Waveform obtained from the finite element analysis.

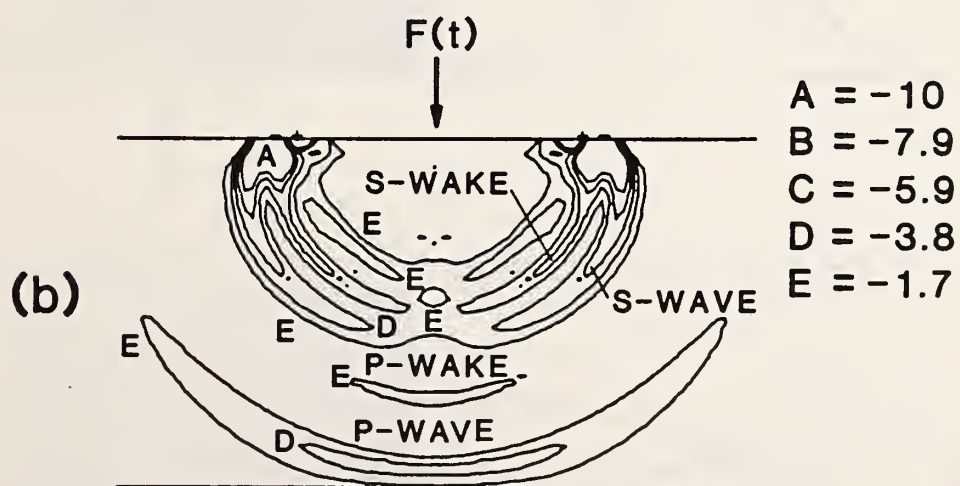
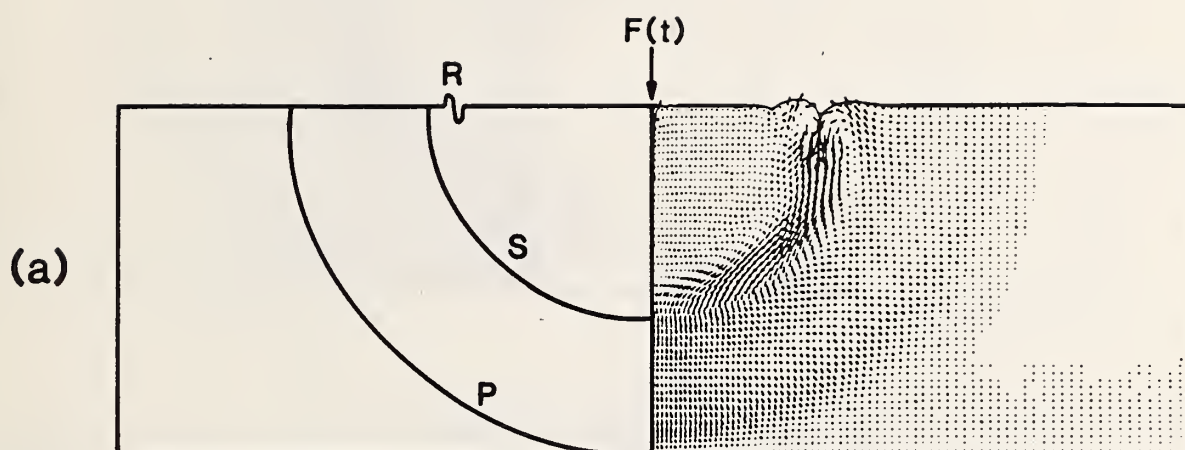


Figure 4.6 Displacement and stress fields within a 0.5-m thick plate 125  $\mu$ s after the start of the impact: a) vector plot of displacements and the location of the wavefronts; and, b) minimum principal stress contour plot.

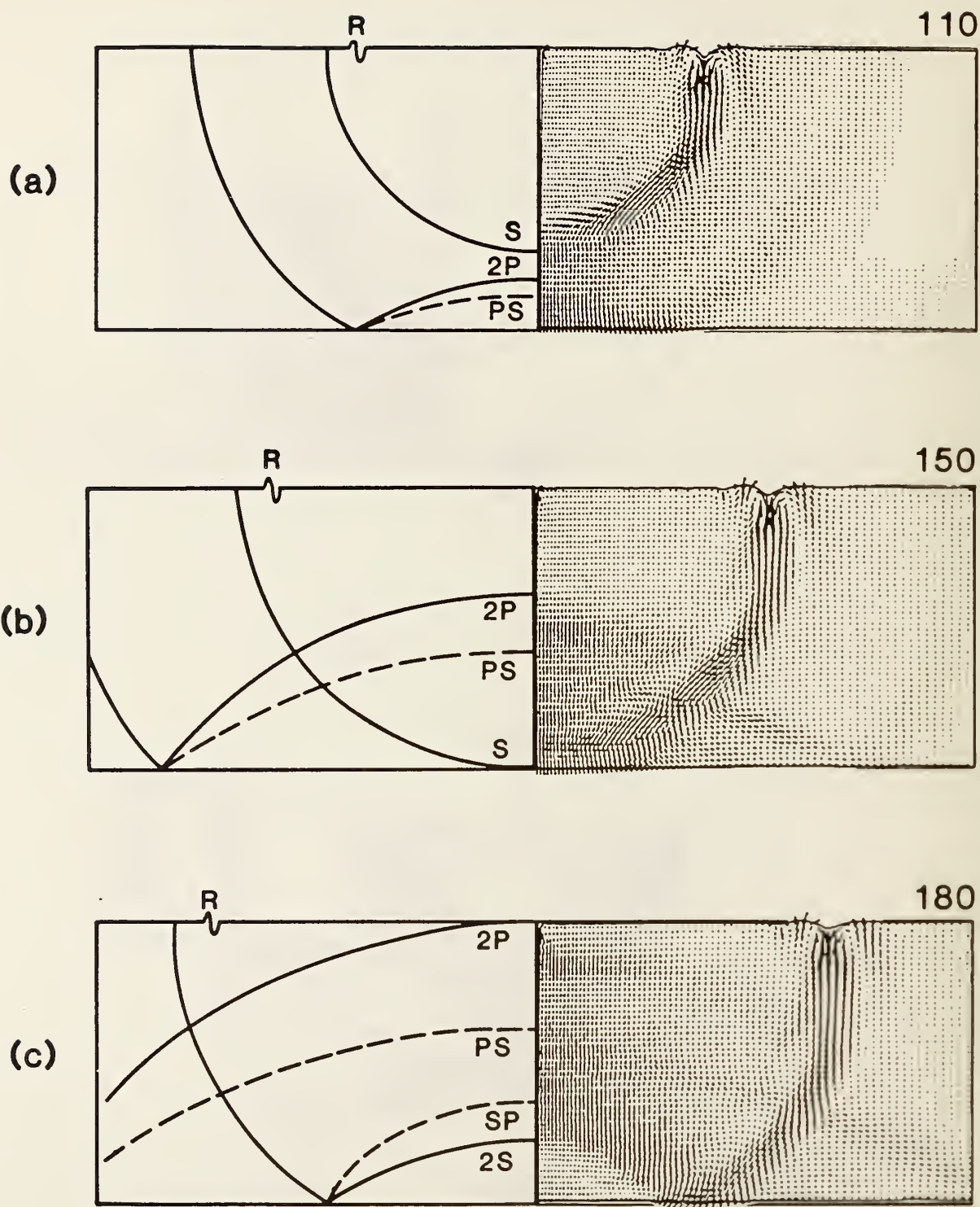


Figure 4.7 Vector plots of displacements at various times after the start of the impact: a) 148  $\mu\text{s}$ ; b) 203  $\mu\text{s}$ ; and, c) 250  $\mu\text{s}$ .

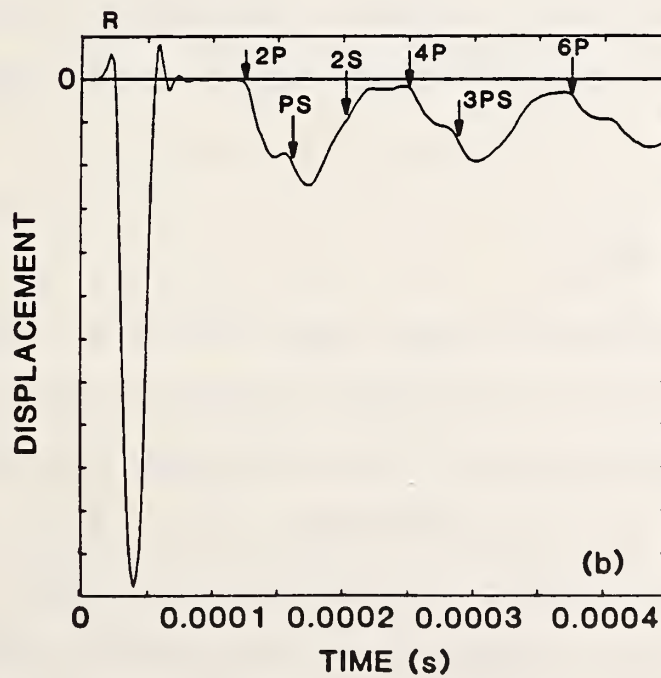
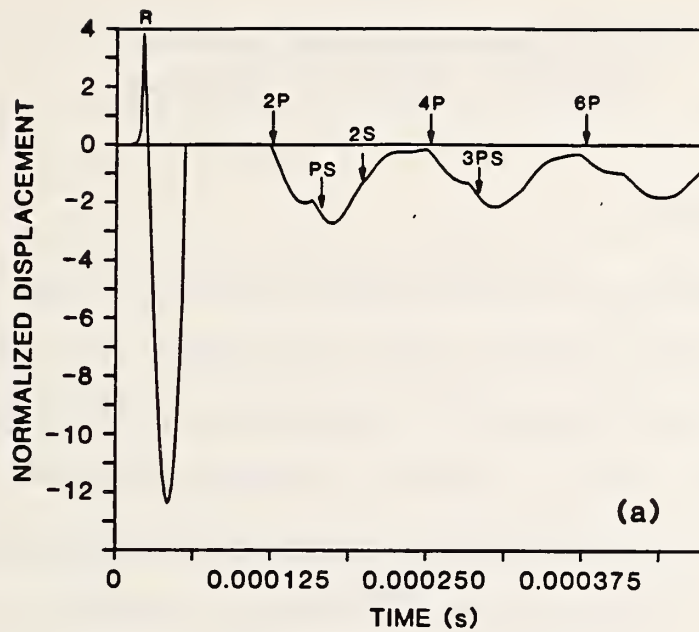


Figure 4.8 Impact-Echo response: a) Green's function solution; and, b) waveform obtained from finite element analysis.



## CHAPTER 5

### FREQUENCY SPECTRUM ANALYSIS OF THEORETICAL IMPACT-ECHO WAVEFORMS

#### 5.1 INTRODUCTION

In Chapter 4, displacement waveforms obtained from an infinite elastic plate were studied in the time domain. In this chapter, the results of analytical studies carried out in the frequency domain are presented. The Fast Fourier Transform technique is used to determine the frequency content of stress pulses generated by elastic impact on a thick plate. Frequency spectra obtained by transformation of theoretical displacement waveforms are studied as a function of the contact time of the impact and the spacing between impact source and receiver. The effects on frequency spectra of clipping or removing the R-wave signal in time domain waveforms are discussed.

#### 5.2 FREQUENCY ANALYSIS

The multiple reflections from the top and bottom surfaces of a plate give the displacement response a periodic character. In bounded solids containing flaws, reflections occur from a variety of interfaces and free boundaries. As a result, time domain waveforms become complex and difficult to interpret. However, if the waveforms are transformed into the frequency domain, multiple reflections from each interface become dominant peaks in the frequency spectrum - at values corresponding to the frequency of arrival of reflections from each interface. These frequencies can

be used to calculate the location of each interface. It will be shown that data interpretation is generally simpler in the frequency domain than in the time domain.

The transformation from the time to the frequency domain is based on the idea that any waveform can be represented as a sum of sine curves, each with a particular amplitude, frequency, and phase shift. This transformation is carried out using Fourier transforms. As an example, Fig. 5.1(a) shows the digital time domain waveform,  $g(t)$ , given by the function:

$$g(t) = \sin 2\pi(20)t + 2 \sin 2\pi(40)t + 3 \sin 2\pi(60)t \quad (5.1)$$

where  $t$  = time (s).

This function is composed of three sine curves of different amplitudes having frequencies of 20, 40, and 60 Hz. The time interval between points in the digital signal is 0.001 seconds; this is equivalent to a sampling frequency of 1000 Hz. The frequency spectrum was obtained from a digital time domain waveform containing 256 points using the Fast Fourier Transform (FFT) technique. A personal computer and an FFT program given in Appendix [B] of Ref. [82] were used to perform the calculations. The frequency spectrum obtained by the FFT technique contains half as many points as the time domain waveform and the maximum frequency in the spectrum is one-half the sampling rate, which for this example is 500 Hz. Fig. 5.1(b) shows the initial portion of the frequency spectrum obtained by the FFT technique; the peaks occur at 20, 40, and 60 Hz. Each of the peaks corresponds to one of the component sine curves in Eq. (5.1). The frequency interval in the spectrum is equal to the

maximum frequency divided by the number of points in the spectrum. For this example, the interval is equal to  $500 \text{ Hz} / 128 \text{ points}$ , that is,  $3.9 \text{ Hz}$ . Since the frequency interval is inversely proportional to the sampling rate, a slower sampling rate enhances resolution in the frequency domain. However, to avoid errors in frequency analysis, the sampling rate should be greater than twice the maximum frequency that appears in the time domain waveform [82].

### 5.3 FREQUENCY SPECTRA OF ANALYTICAL WAVEFORMS

Frequency analyses were carried out for force-time functions generated by the elastic impact of a sphere on a plate and for the surface displacement waveforms obtained from the Green's function solution of point impact on an infinite plate. The frequency content of impact force-time curves and displacement waveforms was studied as a function of the contact time of the impact and the spacing between source and receiver. The results are used to gain an understanding of how experimental test parameters affect the shape of the frequency spectrum.

#### 5.3.1 Frequency Content of the Impact

As has been discussed, the force-time function,  $F(t)$ , produced by the elastic impact of a sphere on a plate can be approximated as a half-cycle sine curve (Eq. (2.12)). This force-time function is shown in Fig. 5.2(a).

The Fourier transform,  $F(s)$ , of the continuous force-time function given by Eq. (2.12) can be obtained in closed form solution

[10]. The amplitude spectrum of this transform is:

$$F(s) = \frac{t_c}{2} \left[ \frac{\sin \pi(s - 0.5)}{\pi(s - 0.5)} + \frac{\sin \pi(s + 0.5)}{\pi(s + 0.5)} \right] \quad (5.2)$$

where  $s = f \cdot t_c$ ; and  
 $f$  = frequency (Hz).

A plot of Eq. (5.2) is shown in Fig. 5.2(b). The X- and Y-axes are normalized with respect to the contact time. To obtain the actual frequency, X-axis values must be divided by the contact time of a specific impact.

The frequency content of the input pulse is directly related to the contact time of the impact. The shorter the contact time the broader the range of frequencies contained in the pulse, but the lower the amplitude of each component frequency. For a long contact time, the pulse is made up primarily of large amplitude, low frequency components. The range of frequencies contained in a stress pulse determines the thickness of a plate that can be measured and the size of the flaw that can be detected using the impact-echo method. Higher frequency pulses are needed to measure the thickness of thin plates, and, as will be discussed in subsequent chapters, higher frequency pulses are needed to detect small flaws.

Notice that in the spectrum of the input pulse (Fig. 5.2(b)), there are frequency values which have zero amplitude. These "zeroes" occur at frequencies equal to  $1.5/t_c$ ,  $2.5/t_c$ ,  $3.5/t_c$ , etc. The frequency difference between two successive zeroes is equal to  $1/t_c$ . For example, if the first and second zeroes occur at 30 and 50 kHz, respectively, then,  $1 / t_c = 20$  kHz, or  $t_c = 50 \mu s$ .

As has been mentioned, the impact of a sphere on a plate



generates an R-wave which propagates along the surface of a test object. This R-wave produces an initial, large amplitude response in the displacement waveform, which resembles a half-cycle sine curve with a half-period approximately equal to the contact time of the impact (see Fig. 4.8(a)). Therefore, the frequency spectrum of the plate response is composed of the spectrum due to P- and S- wave reflections and the spectrum due to the R-wave.

Since the R-wave gives information about the contact time of the impact, the frequency spectrum of experimental waveforms can be used to determine the duration of the input pulse. In this study, the contact time produced by the impact of steel spheres on a plate was estimated by finding the difference between the "zeroes" in the frequency spectrum.

In the theoretical and finite element studies presented in this report, the half-cycle sine curve (Eq. (2.12)) is used as the force-time function for the impact of a sphere on a thick plate. This is in accordance with the Hertz theory of elastic impact. In work carried out by Chang [17], it was shown that for impacts that do not involve large amounts of energy, the Hertz theory is very good. However, in his comparisons of Hertz theory to experiments involving the impacts of small diameter steel balls on a glass plate, it can be seen that the initial and final slopes of the experimental curves are not as steep as the initial slopes predicted by theory. An alternative approximation to the experimentally obtained force-time function is the half-cycle sine squared function, used by Lange and Ustinov [50, 51]. This function



is given by the following equation:

$$F(t) = F_{\max} \sin^2 \left( \pi \frac{t}{t_c} \right) \quad 0 \leq t \leq t_c \quad (5.3)$$

Fig. 5.3 shows a comparison of the force-time functions described by Eqs. (2.12) and (5.3). The maximum amplitude of both curves is the same. However, the initial and final slopes of the sine-squared curve (Eq. (5.3)) are much flatter than the slopes in the half-cycle sine curve (Eq. (2.12)).

The amplitude spectrum of the Fourier transform of the sine-squared curve [51] is very similar to that shown in Fig. 5.2(b), except that the frequencies having zero amplitude occur at  $2/t_c$ ,  $3/t_c$ ,  $4/t_c$ , etc. Thus, a pulse produced by an impact with a half cycle sine-squared force-time function contains a slightly broader range of frequencies than a pulse produced by an impact with a half cycle sine force-time function. The force-time curves obtained by Chang [17] appear to fall somewhere in between the sine and the sine-squared approximations.

Fig. 5.4 shows a comparison between a Green's function solution calculated for a half-cycle sine-squared force-time function (Fig. 5.4(a)) and the solution for a half-cycle sine force-time function (Fig. 5.4(b)). In both solutions, the value of  $H/T$  was equal to 0.2, and the value of  $t_c/t_{2p}$  was equal to 0.25. The surface displacement waveform obtained for an impact having a sine-square force-time function is very similar to that obtained for a sine curve. There are two minor differences between the two waveforms.

- 1) There is less area under a sine-squared curve (Eq. (5.3));

therefore, less total energy is applied during the impact. As a consequence, the amplitudes of the displacements in Fig. 5.4(a) are slightly less than those in Fig. 5.4(b); 2) The initial and final slopes of the sine-squared curve are flatter than those in the sine-curve. Therefore the displacements caused by the arrivals of wavefronts are not as sharp in the waveform generated using the sine-squared curve (Fig. 5.4(a)). Although the following discussion is restricted to surface displacement responses of plates generated by impacts having a half-cycle sine force-time function, the trends and conclusions are equally applicable to responses generated with impacts having half-cycle sine-squared force-time functions.

### 5.3.2 Frequency Content of Infinite Plate Response

#### 5.3.2.1 Contact Time of the Impact

The normal surface displacement waveforms obtained from an infinite plate subjected to impact are affected by the contact time of the impact. The left side of Fig. 5.5 shows a series of displacement waveforms calculated for a test configuration that corresponds to a ratio of impact source - receiver spacing ( $H$ ) to plate thickness ( $T$ ) of 0.2 (see Fig. 4.3(b)). The only variable in Fig. 5.5 is the contact time of the impact, which is also given in terms of a ratio: the contact time of the impact ( $t_c$ ) divided by the arrival of the first P-wave reflection returning from the bottom surface of the plate ( $t_{2p}$ ). Waveforms are shown for  $t_c/t_{2p}$  ratios of 0.15, 0.25, and 1.0.

For  $H/T$  values less than about 0.25, the path length of the

2P-wave is approximately twice the plate thickness; therefore, the travel time,  $t$ , between the successive arrivals of P-wave echoes from the bottom surface of the plate is approximately

$$t = \frac{2T}{C_p} \quad (5.5)$$

The corresponding frequency,  $f$ , of wave arrivals is

$$f = \frac{1}{t} = \frac{C_p}{2T} \quad (5.6)$$

In the spectra shown in the right hand side of Fig. 5.5, the X-axis represents a dimensionless, normalized frequency ( $f_n$ ), which is obtained using the following formula:

$$f_n = \frac{Tf}{C_p} \quad (5.7)$$

Combining Eqs. (5.6) and (5.7) gives  $f_n$  equal to 0.5. This is the normalized frequency corresponding to P-waves arriving from the bottom surface of the plate. Each of the frequency spectra shown in Fig. 5.5 has a peak at  $f_n$  equal to 0.5.

For an impact produced by a short contact time and for the given test configuration (an H/T value of 0.2), the sudden downward displacements in the waveform (Fig. 5.5(a)) correspond to the arrival of the R-wave followed by waves returning from the bottom surface of the plate. The arrival of the first P-wave (2P) corresponds to the downward displacement beginning at  $t_n$  equal to 2. In using the impact-echo technique, the arrival time of this first P-wave can be used to calculate the plate thickness, if the P-wave velocity is known. However, as the contact time increases (Fig. 5.5(c)),

the response becomes smoothed out due to the convolution of the impulse response function of the plate with the force-time function. Wave arrival times no longer agree with the beginning of the downward displacements in the time domain waveform. Thus, in time domain analysis, it is essential to have a short contact time in order to accurately determine wave arrival times.

In frequency analysis, however, it is not essential that the impact have a short contact time. As was shown in Fig. 5.2(b), a short contact time results in a force-time pulse which has energy distributed over a broader frequency range. Thus, a pulse produced by a short contact time has a smaller concentration of energy at the frequency which corresponds to the multiple P-wave reflections as compared to a pulse produced by a longer contact time. Therefore, as is apparent in Fig. 5.5, the peak in the frequency spectrum obtained from a waveform produced by an impact having a short contact time has a smaller amplitude.

The contact time of the impact affects the R-wave signal in both the time and the frequency domains. The Fourier transform of the plate response is composed of the transform of displacements caused by waves reflected from the bottom surface of the plate and the transform of displacements caused by the R-wave. Therefore, the relative magnitude and duration of the initial displacement produced by the R-wave as compared to the displacements produced by internal reflections is important. The R-wave in the time domain waveform generated by the impact with the shortest contact time (Fig. 5.5(a),  $t_c/t_{2p}$  equal to 0.15) causes displacements that are



approximately eight times the amplitude of the displacements produced by reflections from the bottom surface of the plate. Thus the frequency components due to the R-wave are a large portion of the spectrum in Fig. 5.5(a). Notice the similarity between the spectrum shown in Fig. 5.5(a) and the spectrum of the impact force-time function shown in Fig. 5.2(b). In contrast, a waveform generated by an impact having a long contact time (Fig. 5.5(c),  $t_c/t_{2p}$  equal to 1.0) produces a long duration R-wave signal that causes displacements that are only approximately twice that caused by internal reflections. The frequency spectrum is dominated by a single peak which corresponds to waves arriving from the bottom surface of the plate, since the frequency components due to the R-wave are relatively minor.

In practice, the peak in the frequency spectrum can be used to calculate the plate thickness,  $T$ , using the formula

$$T = \frac{C_p}{2 f_p} \quad (5.8)$$

where  $f_p$  = peak frequency.

#### 5.3.2.2 Test Configuration

In addition to the contact time of the impact, the surface displacement waveform is affected by the distance between the impact point and the point where the displacement is calculated. A convenient parameter for describing the test configuration is the ratio of the distance between the impact point and point where the displacement is calculated ( $H$ ) to the plate thickness ( $T$ ). Fig.



5.6 shows a series of displacement waveforms and their corresponding frequency spectra for  $H/T$  values of 0.05, 0.2, and 1.0. The ratio of contact time of the impact to the 2P-arrival time is the same in all the traces and is equal to 0.25.

For a low  $H/T$  value (Fig. 5.6(a)), the displacement due to the R-wave is very large relative to displacements due to internal reflections, and as discussed previously the Fourier transform of the R-wave signal dominates the frequency spectrum. Notice that the frequency spectrum shown in Fig. 5.6(a) is nearly identical to that shown in Fig. 5.2, except for the addition of a small peak corresponding to the frequency of P-wave reflections from the bottom surface of the plate.

The plate response obtained at a point corresponding to a large  $H/T$  value (Fig. 5.6(c)) produces results that are difficult to interpret in both the time and the frequency domains. In this case, the R-wave and the 2P-wave arrive at the receiver at the same time, and the 2P-wave arrival is masked in the transducer response to the very large amplitude R-wave. In addition, there are perturbations in the displacement waveform due to relatively large amplitude S-wave reflections, making the arrival times of individual P- and S-waves difficult to distinguish. There is no peak in the frequency spectrum which corresponds to the frequency of multiple P-wave reflections from the bottom of the plate. These observations can be explained by the physics of wave reflection. The amplitude of P- and S-wave reflections depends, in part, upon the angle that an incident wave strikes a free boundary or an interface. For an

H/T value of 0.05, the amplitudes of reflected P-waves are near their maximum value, while the amplitudes of reflected S-waves are very small. In contrast, for an H/T value of 1.0 the incident angles are large, and the amplitudes of reflected S-waves are near maximum, while the amplitudes of reflected P-waves have decreased to approximately half their value at an H/T value of 0.05 (Section 2.1.3). In addition, for large H/T values, S-wave reflections have a larger displacement component normal to the surface. Thus, for large H/T values, S-wave reflections make a significant contribution to the normal surface displacement. This complicates both the time domain waveform and the frequency spectrum, and makes it impossible to determine the thickness of a plate from the dominant peak in the frequency spectrum.

For the H/T values studied, those in the range of 0.2 to 0.5 give the best results by minimizing the complications caused by large amplitude R-waves and those caused by S-wave reflections.

### 5.3.3 Clipping and Removing the R-Wave Signal

When taking measurements in the laboratory, it is preferable to amplify the signal produced by the reflections returning from internal flaws or the bottom surface of the specimen. This can be achieved by changing the gain setting on the digital oscilloscope so that echo signals occupy the full scale of the display. As a result, the R-wave signal will be cut-off (clipped). Clipping the R-wave in the time domain waveform changes the nature of the R-wave representation in the frequency spectrum, since the clipped R-wave

now resembles a square wave with a duration approximately equal to the contact time of the initial impact. Compare the frequency spectrum shown in Fig. 5.6(a) to that shown in Fig. 5.7(a). Both were obtained from the displacement waveform shown in Fig. 5.6(a). The frequency spectrum in Fig. 5.6(a) is obtained from the original unaltered waveform, while that in Fig. 5.7(a) was obtained after clipping the R-wave signal at an amplitude of -8. In the spectrum obtained from the trace with the clipped R-wave, the frequency peak corresponding to the thickness of the plate is much easier to identify. Thus experimental frequency spectra are made simpler to interpret by amplifying the displacement pattern produced by internal reflections and allowing the R-wave signal to be automatically clipped. The contact time of the impact can still be determined from the zeroes in the frequency spectrum. The only difference is that the zeroes in the Fourier transform of a square wave of duration  $t_c$  occur at  $1.0/t_c$ ,  $2.0/t_c$ ,  $3.0/t_c$ , etc [10].

If the R-wave is removed completely from the waveform, only frequencies obtained by transforming the displacements produced by internal reflections are present in the spectrum. For example, if the R-wave is completely removed from the waveform shown in Fig. 5.6(a), the spectrum in Fig. 5.7(b) is obtained. The spectrum contains no information about the contact time of the impact.

Thus clipping the R-wave signal, as is automatically done in experimental work, appears to be the optimum approach. The peak corresponding to the thickness of the plate is easier to identify, and information about the contact time of the impact is preserved.

#### 5.4 CONCLUSIONS

The Fast Fourier Transform technique was used to study the frequency content of pulses and theoretical surface displacement waveforms produced by the impact of a sphere on a thick plate.

Analytical results show that frequency spectrum analysis can be used to determine the frequency content of a pulse generated by impact, the contact time of the impact, and the thickness of plate specimens.

To facilitate interpretation of frequency spectra it is advantageous to: (a) clip the R-wave signal in the displacement waveform; (b) avoid using impacts having a very short contact times relative to the time of arrival of the first P-wave; and (c) keep the distance between the impact point and the point where displacement is monitored within 0.2 to 0.5 of the plate thickness.

Frequency spectrum analysis is shown to be simpler than time domain analysis. In the time domain, the arrival time of P-waves must be determined. Accurate interpretation of time domain displacement waveforms must be carried out by an experienced person and is feasible only for simple geometries. However, in the frequency domain, the depth of reflecting interfaces is easy to determine from the dominant peaks in the spectra. In Chapter 7, the ideas presented in this chapter are extended to the study of displacement waveforms and frequency spectra obtained during impact-echo testing of solid concrete plates and concrete plates containing flaws.



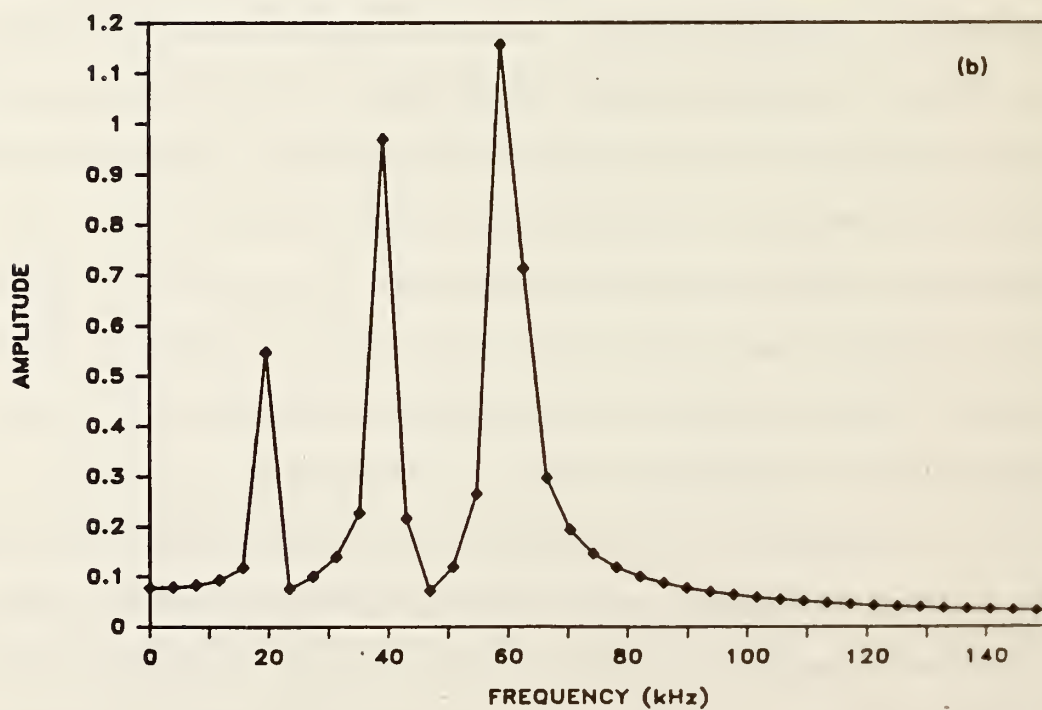
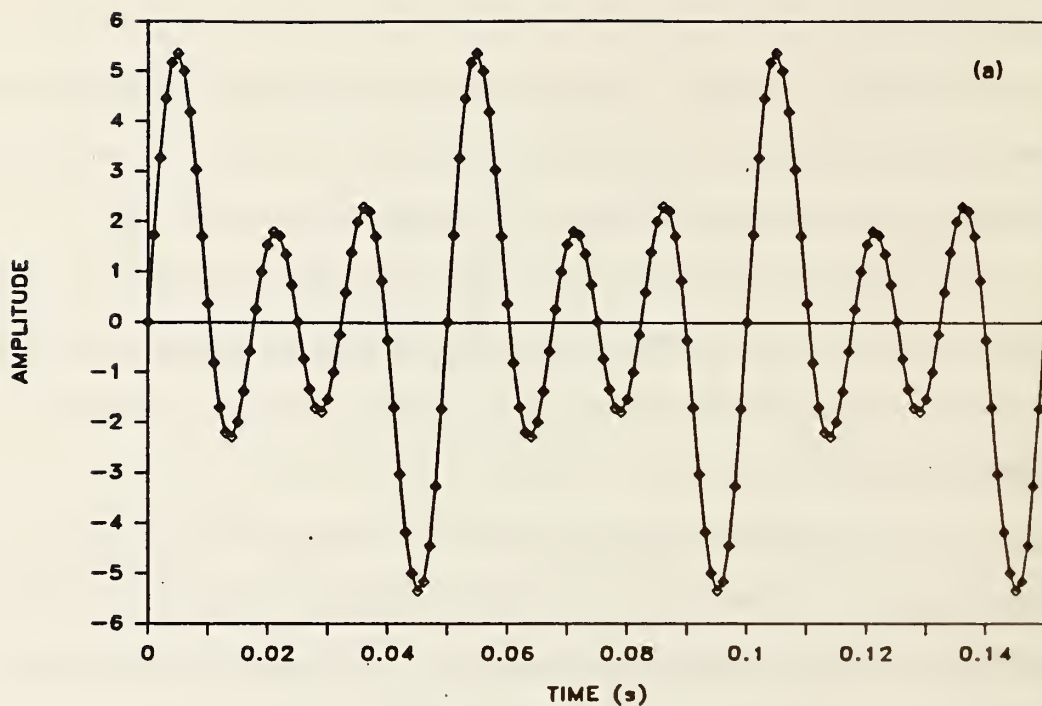


Figure 5.1 Example of a frequency spectrum obtained from a time domain waveform using the Fast Fourier Transform technique. a) digital time domain waveform; and, b) frequency spectrum.



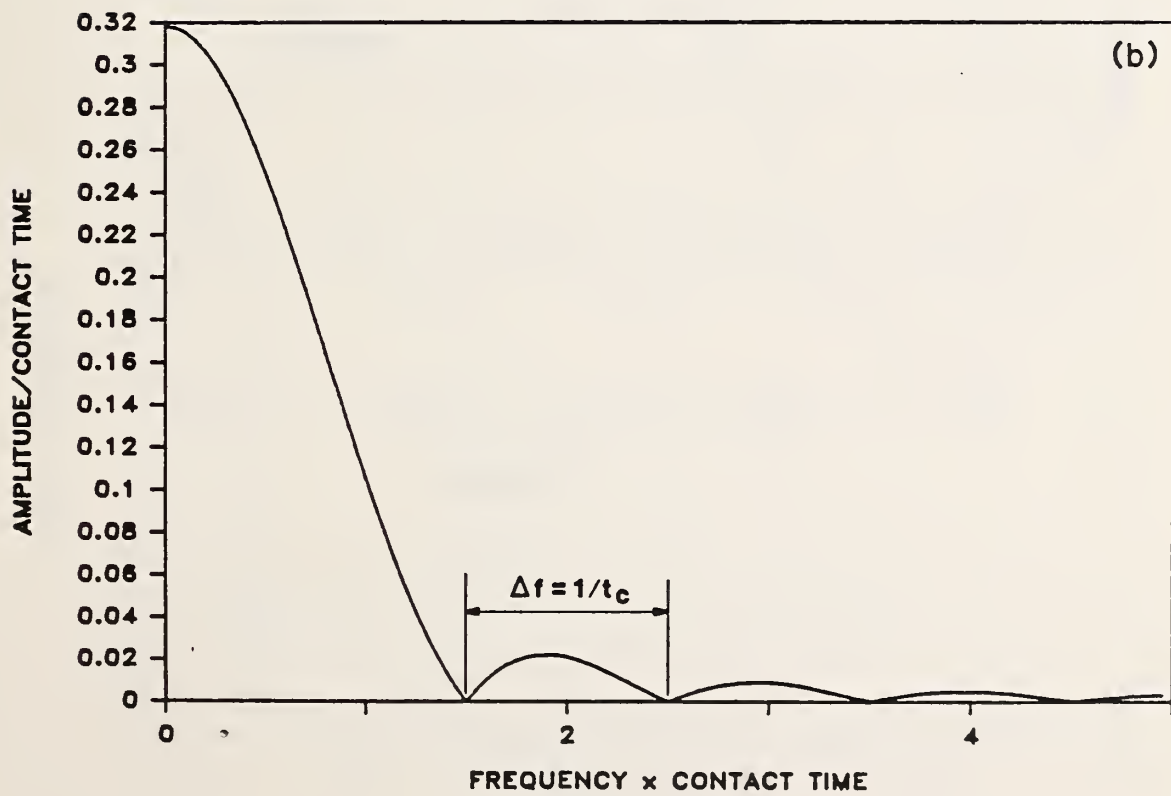
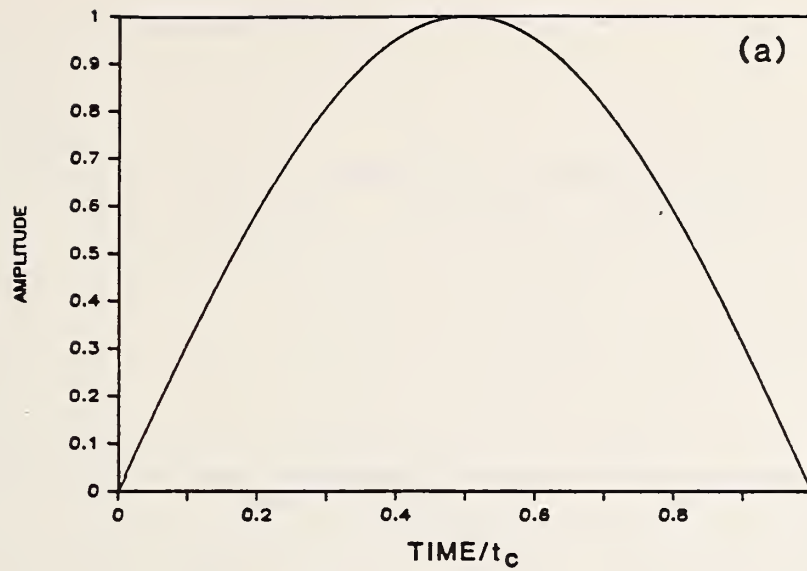


Figure 5.2 Stress pulse produced by the elastic impact of a sphere on the top surface of a plate: a) force-time function; and, b) Fourier transform.

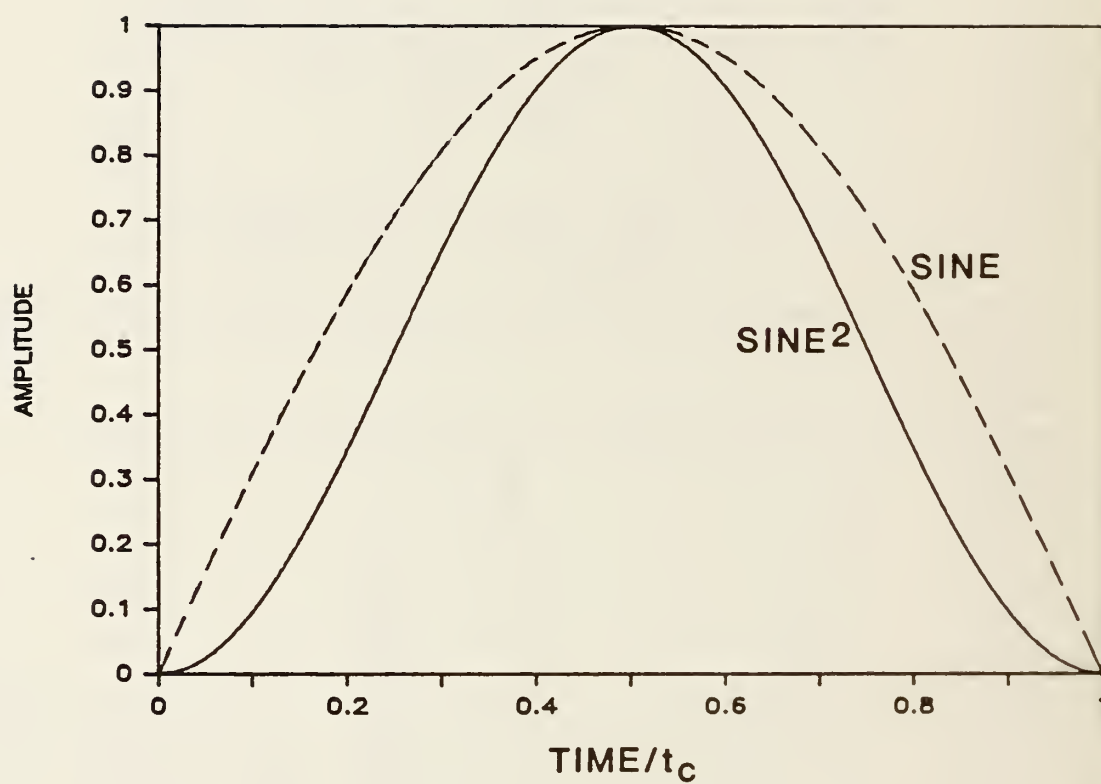


Figure 5.3 Comparison of half-cycle sine and sine-squared force-time functions.

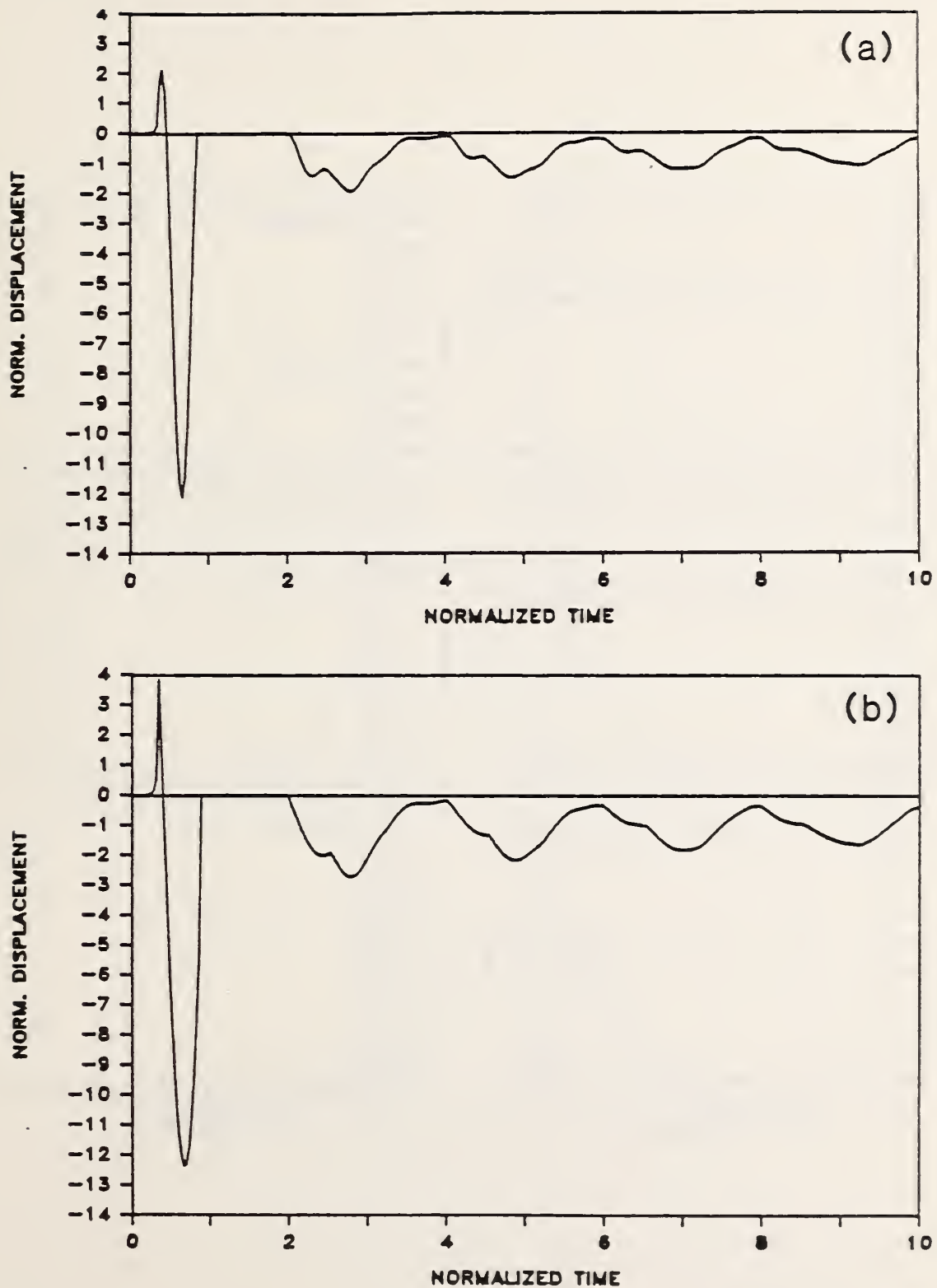


Figure 5.4 Comparison of surface displacement waveforms for two force-time functions ( $H/T = 0.2$  and  $t_c/t_{2p} = 0.25$ ): a) half-cycle sine-squared function; and, b) half-cycle sine function.

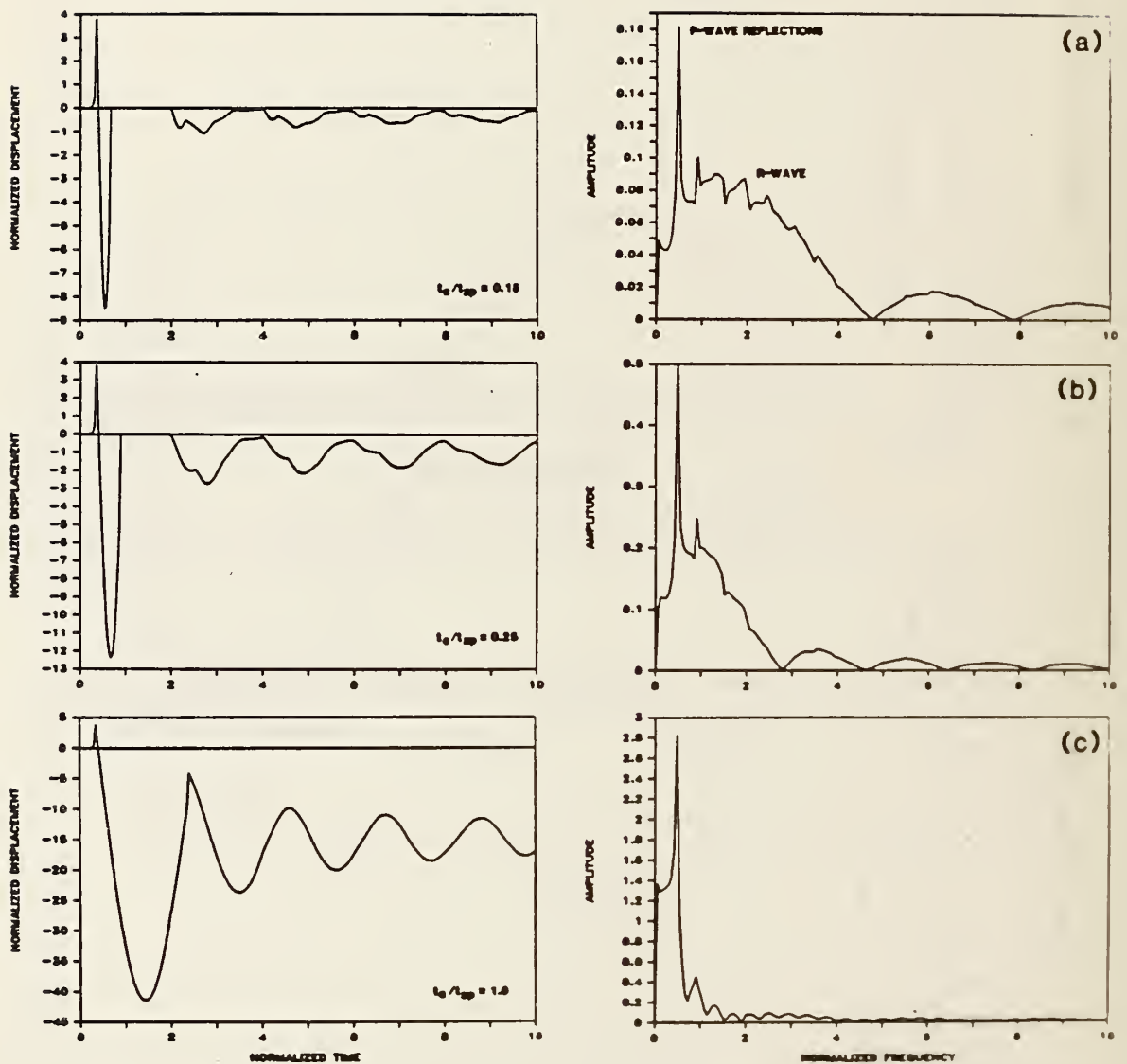


Figure 5.5 The effect of contact time of the impact of the response of an infinite plate for  $H/T = 0.2$ : a)  $t_c/t_{2P} = 0.15$ ; b)  $t_c/t_{2P} = 0.25$ ; and, c)  $t_c/t_{2P} = 1.0$ .

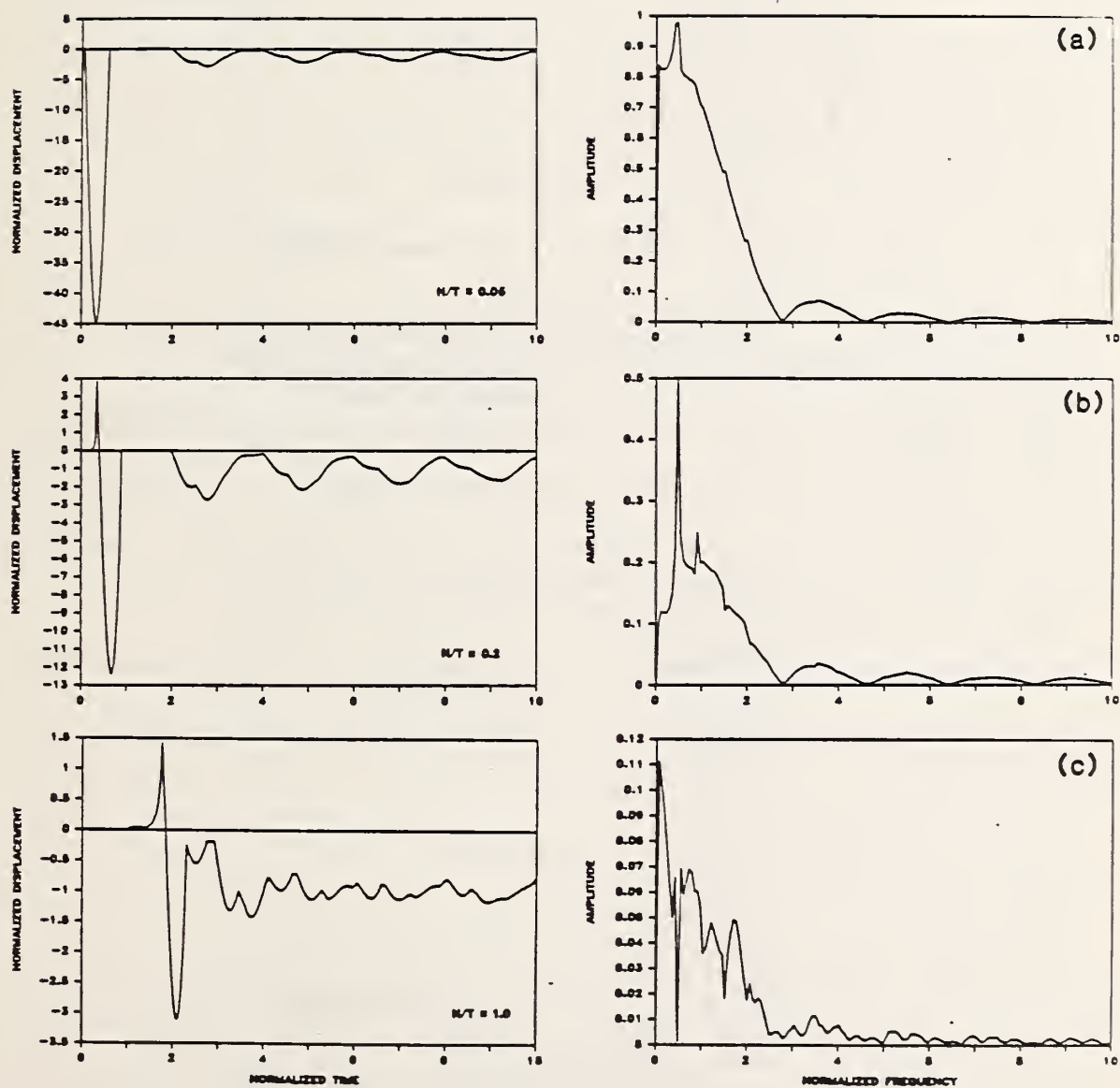


Figure 5.6 The effect of impact source - receiver spacing on the response of an infinite plate for  $t_c/t_{2p} = 0.25$ : a)  $H/T = 0.05$ ; b)  $H/T = 0.2$ ; and, c)  $H/T = 1.0$ .



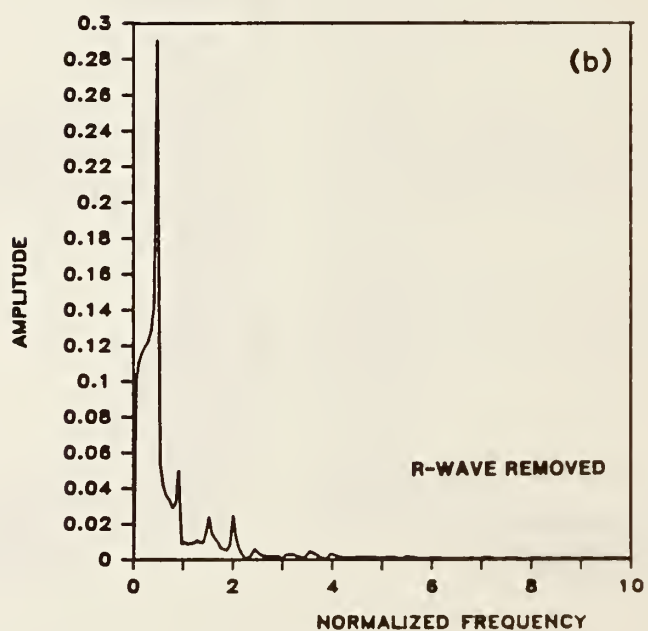
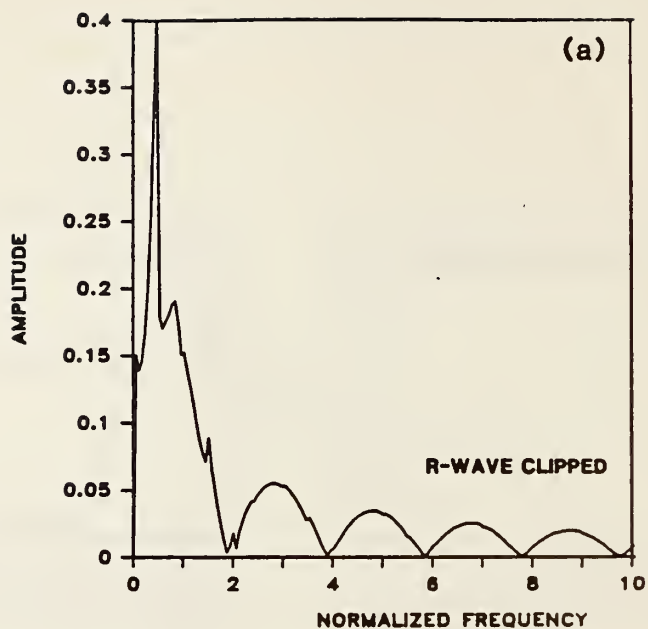


Figure 5.7 Effect on the frequency spectrum due to partially and completely removing the R-wave signal from the time domain displacement waveform shown in Figure 5.5(a): a) R-wave signal clipped at an amplitude of -8; and, b) R-wave signal completely removed.

CHAPTER 6  
A FINITE ELEMENT STUDY  
of the  
INTERACTION OF TRANSIENT STRESS WAVES WITH PLANAR FLAWS

6.1 INTRODUCTION

This chapter presents finite element studies of the interaction of transient stress waves with planar discontinuities in an elastic solid. Emphasis is placed on the effects on displacement waveforms caused by waves diffracted from the edges of a flaw.

The finite element results had to be verified by comparison with experimentally obtained waveforms; thus an aluminum plate containing a flat-bottom hole was chosen for the initial finite element studies because the physical specimen was easy to fabricate.

Displacement waveforms obtained from analyses of planar, disk-shaped flaws in aluminum and concrete plates are presented. Displacement and stress fields produced by the interaction of transient waves and a planar disk-shaped flaw in a concrete plate are studied. Finally, parameter studies of concrete plates containing disk-shaped flaws were carried out to determine the effect of important test variables on surface displacement waveforms. The variables that were studied included: the diameter and depth of a planar flaw; the contact time of the impact (frequency content of the waves); and, the distance between the impact point and the point where the displacement is recorded. The results of these studies are used in Chapter 7 to help interpret experimental impact-echo displacement waveforms.

### 6.1.1 The Use of Numerical Methods for the Study of Stress Wave Propagation in Solids

In the past 15 years, advances in computer technology and the availability of computer power has enabled the use of numerical models to study the stress wave propagation in solids. The use of approximate numerical methods to study nondestructive testing (NDT) related problems has been motivated by the limited number of analytical solutions that are available for these types of problems, and because of the difficulties involved in obtaining quantitative information from experimental techniques. With the emphasis on the development of reliable NDT methods, there was and is a need for alternate methods. Numerical methods provide the ability to model arbitrary geometries and boundary conditions (loading and support conditions) and to obtain full field solutions. The early work in the use of numerical models to study stress wave propagation in solids was carried out by researchers in geophysics and seismology. Application of numerical models to NDT related problems soon followed.

In 1982, Bond [7] wrote a comprehensive summary of methods available for the computer modelling of ultrasonic waves in solids. He reviews Ray Tracing methods, Finite Difference methods (explicit schemes and the Method of Characteristics), Finite Element methods, and several other lesser known modelling techniques. Most of the work that has been done in the past has involved the use of ray tracing methods and finite difference methods; Bond's summary provides an excellent review of the progress that has been achieved using these methods.

Boundary Element (Boundary Integral Equation) methods have also been applied to steady-state and transient stress wave propagation problems. Ref. [59] presents a summary of the different boundary element methods that have been used to study stress wave propagation. Ref. [44] discusses the types of problems that have been studied using these methods. One class of problems that has been studied extensively is dynamic stress concentrations created by the interactions of stress waves with cavities and elastic inclusions in infinite or semi-infinite solids.

In 1982, Bond, in his review of numerical models, stated that finite element techniques had yet to be applied to pulsed elastic wave problems related to NDT [7]. In other fields, such as seismology and electromagnetism, finite element methods have been used to study wave problems. Many of these applications are summarized by Bond [7].

Finite element methods have been applied to the study of elastic stress wave propagation in rods [77] and layered waveguides [46], and to flexural wave propagation in beams [94]. The method was used to determine the plane strain, steady-state response of an elastic half-space to a surface pressure wave (Cole-Huth problem) and the axisymmetric response of an elastic half-space to a concentrated, downward step force applied at a given depth beneath the free surface of the half-space (Pekeris-Lifson problem) [77].

Much work has been done on the use of finite elements for problems involving stress wave propagation produced by blast [18] or impact [95]. Much of this work is classified, but some of the

finite element codes developed for these applications (such as DYNA, the code used to carry out the finite element analyses presented in this report) are suitable for NDT related studies. The capabilities of available codes are discussed in Ref. [95].

A review of the applications of the finite element method to stress wave propagation in solids revealed only one series of studies that used the method for NDT related problems. In these studies, a combined finite element and analytical method was used for analyzing scattering of plane, longitudinal waves and vertically polarized shear waves by cavities in an infinite elastic medium [76], and for scattering of plane horizontally polarized shear waves by surface breaking cracks [1, 20]. The defects were contained in an interior bounded region which was represented by finite elements. Wavefunction expansions are used to represent the field in the exterior region. A nodal force-displacement relation was developed to satisfy the continuity conditions along the boundaries separating the two regions. Results obtained by the method for scattering of plane, longitudinal and shear waves by a circular, cylindrical cavity are shown to agree with the exact solution [76].

The work in this report represents the first application of the finite element method to the study of transient wave propagation in solids containing flaws.

## 6.2 BACKGROUND

When a transient stress wave is incident upon a crack within a solid, the following phenomena occur: specular reflection from



the crack face; diffraction at the crack tip; and, mode conversion of waves on the crack face and at the crack tip. Fig. 6.1(a) shows the specularly reflected P-wavefront (2P) and the mode-converted PS-wavefront produced when a spherical P-wave is incident upon a circular crack. Rays OA, which intersect the crack tips, will be diffracted as shown in Fig. 6.1(b), producing two diffracted waves,  $P_dP$  and  $P_dS$ . The designation used for diffracted waves includes the incident wave and the wave produced by diffraction. For example,  $P_dS$  is the designation for the diffracted S-wave that is produced by an incident P-wave. The diffracted waves propagate along cylindrical wavefronts; the crack tip is the center of the cylinder. A similar set of specular (2S), mode-converted (SP), and diffracted waves ( $S_dP$  and  $S_dS$ ) are produced when the S-wave is incident upon a crack. The amplitude of particle motion in each of the specularly reflected, mode-converted, and diffracted waves varies with direction and depends upon the size, geometry, and depth of the crack, the frequency content of the waves incident upon the crack, and the orientation of the crack with respect to the propagating waves. As shown in Fig. 6.1(b), there is a region beneath the crack called the shadow zone, where direct P- and S-waves cannot penetrate.

Fig. 6.2 shows a schematic representation of point impact on a plate containing a planar disk-shaped flaw. The center of the flaw is located directly under the point of impact and the flaw is parallel to the top surface of the plate. This is the case that will be discussed in this report. For this condition, the important variables affecting the response are the diameter,  $D$ , and depth,

$T$ , of the flaw, and the frequency content of the stress waves generated by impact. The frequency content is determined by the contact time,  $t_c$ , of the impact (Section 5.3.1). A long contact time produces stress waves made up primarily of large amplitude, low frequency components. Stress waves produced by a short duration impact contain a broader range of frequencies; however, the amplitude of each component frequency is lower. This is important because it is the frequency content of the waves that determines the size of a flaw that can be detected by monitoring specular reflections using the impact-echo technique. Waves containing higher frequency components are needed to detect smaller flaws.

### 6.3 PLATE WITH A FLAT-BOTTOM HOLE

In the impact-echo method, a surface displacement waveform recorded near the point of impact is used to gain information about the interior of the solid. When sharp discontinuities exist, the displacements caused by the arrival of diffracted waves are added to the displacements caused by the arrival of reflected waves. Correct interpretation of waveforms requires an understanding of the displacements caused by diffracted waves. In this study, the finite element method is used to gain this understanding.

A plate containing a flat-bottom hole is the simplest test specimen that can be fabricated to model a solid containing an internal flaw with sharp edges. A physical specimen was needed to verify the results from the finite element analyses.

In the discussion of the elastic response of a plate with

a flat-bottom hole to point impact on the top surface, the following analytical results are presented: 1) the displacement time-history obtained on the surface of the hole, directly under the point of impact; 2) displacement fields recorded at successive times to show transient stress waves propagating within the plate; and 3) the displacement time-history of a point on the top surface of the plate, near the point of impact. To clearly identify the effects caused by diffraction, the displacement time-histories obtained from the plate with a flat-bottom hole are compared to time-histories obtained from a solid plate which had the same thickness as the distance to the flat-bottom hole. Finally, a displacement time-history obtained from a finite element analysis is compared to an experimentally obtained impact-echo displacement waveform.

The dimensions of the plate with the flat-bottom hole are shown in Fig. 6.3. The diameter,  $D$ , is 0.038 m and the depth of the hole,  $T$ , is 0.038 m; this geometry corresponds to a  $D/T$  value equal to 1. The axisymmetric, finite element model is shown on the right hand side of the figure. The plate is made of aluminum and the values of the material properties used in the analysis were: a modulus of elasticity of  $7.1 \times 10^7$  kPa, a Poisson's ratio of 0.33, and a density of  $2700 \text{ kg/m}^3$ . These values resulted in P-, S-, and R-wave speeds of 6242, 3144, and 2930 m/s, respectively. In the region above and near the edge of the hole, 0.75-mm square elements were used to construct the finite element model. The time history of the impact loading was a half-sine curve with a 2  $\mu\text{s}$  contact time ( $t_c$ ). The arrival time of the 2P-wave reflected from the

surface of the hole is  $12.2 \mu\text{s}$ ; this results in a  $t_c/t_{2p}$  value of 0.16. The transient load was applied as a uniform pressure over one element at the centerline of the plate. In the analyses of aluminum plates discussed in this chapter, values of displacement and stress were stored in data files every  $0.2 \mu\text{s}$ .

### 6.3.1 Displacement Response at the Center of the Hole

The vertical displacement waveform obtained at the center of the flat-bottom hole (point A in Fig. 6.3) is shown as a solid line in Fig. 6.4. This response consists of vertical surface displacements caused by the arrival of the direct waves, multiply reflected waves (3P), mode-converted waves (2PS), and diffracted waves ( $P_dP$ ,  $P_dS$ ,  $S_dP$ ,  $S_dS$ ,  $3P_dP$ , etc). The computed arrival times of the various waves are indicated on the waveform. The analysis was terminated before waves reflected from the sides and the bottom of the plate arrived at the hole.

For comparison, the dashed line in Fig. 6.4 shows the response of a point at the center of the bottom surface of a solid aluminum plate. The plate was  $0.038 \text{ m}$  thick, and was subjected to a  $2 \mu\text{s}$  duration impact, as in the analysis of the plate containing the flat-bottom hole. The finite element mesh for the plate was the same as the mesh for the top  $0.038\text{-m}$  thickness of the flat-bottom hole model (Fig. 6.3), that is, the elements below the depth of the hole were eliminated. The vertical surface displacement for the plate consists of displacements caused by direct, multiply reflected, and mode-converted waves; diffracted waves are absent.



The waveform obtained from the flat-bottom hole is the superposition of this plate response and the displacements caused by diffracted waves. Thus, the differences between the waveforms shown in Fig. 6.4 are due to the displacements caused by diffracted waves from the edges of the flat-bottom hole.

Using the waveform obtained from the solid plate as a baseline response, that is, the component of the response that is common to both waveforms, the effect of the diffracted waves on the displacement pattern in the waveform obtained from the surface of the flat-bottom hole can be determined. The arrival of diffracted wave  $P_dP$  produces a noticeable discontinuity in the displacement pattern, but causes only a slight increase in the magnitude of the displacement compared with the baseline response. The  $P_dS$ -wave causes an upward displacement of the surface which pushes the surface well above its original undisturbed position. The  $S_dP$ -wave also produces an upward displacement of the hole; however, the magnitude of this displacement is less than that produced by  $P_dS$ . The  $S_dS$ -wave causes an increase in the magnitude of the upward displacement that occurs after the 3P-wave. Arrivals of subsequent diffracted waves ( $3P_dP$  and  $3P_dS$ ) produce noticeable displacements in the waveform that are absent in the waveform obtained from the solid plate. Thus, for this particular flat-bottom hole geometry and for the 2  $\mu s$  duration impact used in the analysis, large amplitude, diffracted waves are produced which significantly alter the displacement pattern obtained at the center of the hole compared with that obtained at the bottom of a solid plate.



### 6.3.2 Displacement Fields

The right sides of Figs. 6.5(a) and (b) show vector plots of the displacement fields in the plate with the flat-bottom hole at 6.1 and 10  $\mu\text{s}$  after the start of the impact. (Since the displacement field is axisymmetric, the field for only half of the specimen is shown.) The corresponding positions of the P-, S-, mode-converted, and diffracted wavefronts are indicated on the left side of each figure.

The displacement field at 6.1  $\mu\text{s}$  (Fig. 6.5(a)) shows the P-wavefront arriving at the hole. The S-wavefront has traveled approximately half the distance to the hole. The pattern of displacements between the P- and S-waves, the P-wake, is evident.

Fig. 6.5(b) shows the displacement field at 10  $\mu\text{s}$ . The reflected P-wave (2P) is evident. The mode-converted PS-wave, produced by the incident P-wave, is difficult to distinguish as it overlaps the S-wave. The surface of the hole is displaced downward due to the displacements caused by the preceeding P-wave and the P-wave wake, which at 10  $\mu\text{s}$  is incident upon the hole (see Fig. 6.4). The pattern of displacements trailing the S-wave, the S-wake, is clearly evident. The low amplitude head wave can also be distinguished. Diffracted waves  $P_dP$  and  $P_dS$  have been produced by the P-wave incident at the edge of the hole. The  $P_dP$ -wave is clearly evident in the shadow zone behind the hole (Fig. 6.5(b)) where the direct P-wave cannot penetrate. The circular pattern of displacements caused by  $P_dS$  is larger in amplitude than that caused by  $P_dP$ , and is easily identified around the edge of the hole.

To show the effects of the diffracted waves on the displacement response at the hole, the vector plots shown in the right side of Figs. 6.6(a), (b), and (c) are close-ups of the region near the hole. The plots represent the displacement fields at 12, 13.5, and 15  $\mu\text{s}$  after the start of the impact. The positions of the wavefronts are shown on the left side of each figure.

In the displacement field at 12  $\mu\text{s}$ , (Fig. 6.6(a)), the S-wave is incident on the center of the hole. The  $P_dP$ -waves are overlapping in the region above the hole.

Fig. 6.6(b), the displacement field at 13.5  $\mu\text{s}$ , shows the S-wave incident upon the edge of the hole. In the radiation pattern of the S-wave (Fig. 4.2), vertical displacements in the center of the plate are very small; therefore, the S-wave does not cause significant downward movement of the center region of the hole. Thus, at 13.5  $\mu\text{s}$ , the center region of the hole is recovering and moving upward. At larger angles in the radiation pattern, the vertical component of the displacement in the S-wave increases. Thus, the outer region of the hole is depressed by the incident S-wave. The fronts of diffracted waves  $P_dS$  (one from each edge) have just arrived at the center of the hole. Recall that in the displacement waveform obtained from the surface of the flat-bottom hole (solid line in Fig. 6.4), it was  $P_dS$  that produced the large upward displacement that pushed the center of the hole well above its original undisturbed position. In Fig. 6.4, at 13.5  $\mu\text{s}$ , the center of the hole is moving rapidly upward, but it is still displaced below its undisturbed position.

At approximately  $15\ \mu\text{s}$ , the upward displacement of the center of the hole has reached its maximum (see Fig. 6.4). The center of the hole is displaced upward, while the edge of the hole is pushed down by the incident S-wave. The diffraction pattern has become complicated; at  $15\ \mu\text{s}$  four diffracted wavefronts have been produced by the incident P- and S-waves. Each of these diffracted waves will give rise to new diffracted waves when they reach the opposite edge of the hole [2]. These doubly diffracted wavefronts have not been discussed as they appear to be of secondary importance. The arrival of multiply reflected P- and S-waves from the top surface of the solid, such as the 3P-wave (seen at the top of Fig. 6.6(c)), will also produce diffracted waves. In addition, diffracted waves will be reflected from the top surface of the plate, giving rise to new diffracted waves when they strike the edge of the hole.

### 6.3.3 Impact-Echo Response

Displacement responses recorded on the top surface of a plate are referred to as impact-echo waveforms. Impact-echo waveforms obtained from both the plate with the flat-bottom hole and the solid plate can be used to determine the effects caused by diffracted waves on the displacement response at the top surface. The effects caused by diffracted waves can be more difficult to determine at the top surface of the plate than at the center of the surface of the hole, because surface waves often mask the effects caused by the specularly reflected and diffracted waves. However, since the relative wave arrival times of surface waves, reflected waves, and

diffracted waves differ at increasing distances from the impact point, the problem can be overcome by studying waveforms obtained at different points along the surface.

A study of impact-echo waveforms obtained from the plate with the flat-bottom hole showed that  $P_dP$ ,  $P_dS$ ,  $S_dP$ , and  $S_dS$  all cause upward movement of the top surface of the specimen. This is in contrast to the downward displacements caused by specularly reflected P-waves. Displacement waveforms represent the superposition of displacements caused by specularly reflected and diffracted waves. Thus, depending upon the arrival times of the diffracted waves relative to the specularly reflected waves, the effect of a diffracted wave may only appear to lessen or increase the displacements caused by specularly reflected waves.

As an example, the solid line in Fig. 6.7 shows a displacement waveform obtained on the top surface of the plate with the flat-bottom hole. The separation,  $H$ , between the impact point and the point where the response was recorded was 0.025 m (point B in Fig. 6.3). The response consists of displacements caused by the arrivals of direct P-, S- and R-waves propagating along the surface, reflected P- and S-waves ( $2P, 2S, 4P$ ), mode-converted waves ( $PS$ ), and diffracted waves ( $P_dP$ ,  $P_dS$ ,  $S_dP$ ,  $S_dS$ , etc.). The arrival times of these various waves are indicated on the waveform. In the figure, arrival times of diffracted waves correspond to the arrival of waves diffracted from the point on the edge of the hole nearest the receiver; these diffracted waves produce the most significant effects in the displacement response.



For comparison, the dashed line in Fig. 6.7 represents an impact-echo response that was obtained from the analysis of the 0.038-m thick plate subjected to a 2  $\mu$ s duration impact. As for the plate containing the flat-bottom hole, the separation between the impact point and point where the waveform was recorded was 0.025 m. The response is dominated by the arrival of the P-waves which cause downward displacements; the top surface is never displaced above its undisturbed position.

From a comparison of the waveforms in Fig. 6.7, it is concluded that the diffracted waves cause the following effects:  $P_dP$  noticeably reduces the downward displacement caused by the 2P-wave;  $P_dS$  appears to have little effect, although it slightly reduces the downward displacement caused by the PS-wave;  $S_dP$  and  $S_dS$  both cause upward displacements.

If another point on the top surface of the plates had been chosen for this comparison, the displacement response caused by superposition of the specular and diffracted waves would be different, as both the arrival times and the amplitudes of the waves change relative to one another.

#### 6.3.4 Comparison to Experimental Waveform

Since no exact solutions are available to compare with the finite element displacement waveforms, the finite element solution was verified by comparison to an experimentally obtained waveform. An impact-echo test was carried out on an aluminum plate containing a flat-bottom hole with dimensions as shown in Fig. 6.3. The impact



point was located at the center of the specimen; the spacing between the impact and receiving transducer was 0.029 m. The impact source was a 1.6-mm diameter steel ball, dropped from a height of 3 cm. A high fidelity, conical, broadband displacement transducer, developed at NBS for acoustic emission testing [68], was used as the receiver. The output of this transducer is proportional to normal surface displacement. The small diameter of the conical tip of the transducer (1.5 mm) approximated a point receiver. (This transducer will be discussed in more detail in Chapter 7.) Fig. 6.8(a) shows the experimental waveform up to a time of 60  $\mu$ s. Using the measured response, the contact time of the impact was determined to be 10  $\mu$ s. The waveform includes reflections from the sides and bottom of the plate. At 40  $\mu$ s, the P-wave reflection from the bottom of the plate arrives at the receiver causing a large downward displacement; at 52  $\mu$ s, the R-wave reflected from the side of the plate arrives at the receiver also causing a large downward displacement.

Fig. 6.8(b) shows a displacement waveform obtained from a finite element analysis of the plate containing the flat-bottom hole subjected to an impact having a force-time history in the shape of a half-sine curve with a contact time of 10  $\mu$ s. The spacing between impact point and the point where the displacement was recorded was 0.029 m, as in the experiment.

There is good agreement between the experimental response and the response predicted by the finite element analysis, that is, there is agreement in the pattern of displacements caused by

the surface wave, specular reflections, and diffracted waves. The 10  $\mu$ s duration impact results in a  $t_c/t_{2p}$  value of approximately 0.8. For this contact time and for the spacing between the impact point and the receiver, effects due to individual wave arrivals are difficult to discern. The superposition of effects causes the arrival of the initial internal reflections to be hidden in the response of the surface to the large amplitude R-wave. However, the important feature in both waveforms is that effects caused by diffracted waves move the surface above its undisturbed position.

This comparison verifies that the finite element method can be used to model transient wave propagation in elastic solids containing flaws. Thus, the method can be used to study the interaction of transient waves with flaw geometries more likely to be encountered in actual impact-echo testing. In the following section, the discussion of a plate containing a flat-bottom hole is extended to study a similar, but more realistic, geometry - a plate containing a planar, disk-shaped flaw.

## 6.4 PLANAR DISK-SHAPED FLAWS IN PLATES

### 6.4.1 Flaw in Aluminum

The dimensions of an aluminum plate containing a disk-shaped flaw are the same as those shown in Fig. 6.3 for the plate containing the flat-bottom hole. The depth and diameter of the circular flaw are identical to the same dimensions for the flat-bottom hole. The finite element model is identical to that shown in Fig. 6.3, with the addition of the elements required to form a disk-shaped

void from the hole. The void is 0.001 m thick. The analysis was carried out using the same material properties and loading conditions as used in the analysis of the plate with the flat-bottom hole.

Displacement waveforms obtained at the center of the top surface of the flaw (point A in Fig. 6.3) and at a point on the top surface of the plate, 0.025 m from the point of impact (point B in Fig. 6.3), are shown in Figs. 6.9(a) and (b), respectively. Wave arrival times are indicated on both waveforms. These waveforms do not need detailed explanation as they are very similar to those obtained from the plate containing the flat-bottom hole (Figs. 6.4 and 6.7). There are minor differences in the waveforms obtained from the surface of the hole (Fig. 6.4) and the disk-shaped flaw (Fig. 6.9(a)) which occur after the arrival of the  $S_dS$ - and 2PS-waves. The waveforms obtained at the top surface of the plates are almost identical, except that the displacements in the waveform obtained from the plate containing the disk-shaped flaw (Fig. 6.9(b)) appear shifted slightly above those obtained from the plate with the flat-bottom hole after the arrival of the  $S_dP$ -wave. Thus, it appears that the presence of the material below the flaw does not significantly change the overall response. (This conclusion is only valid for the period of time prior to wave reflections from the bottom of the plate.)

The displacement patterns previously discussed were obtained for planar flaws in aluminum, a material with a Poisson's ratio of 0.33 (ratio of S- to P-wave speeds equal to 0.50). As explained, aluminum was used so that waveforms obtained from the finite element

analysis could be compared to waveforms obtained from an easily fabricated test specimen. However, the primary focus of the research program is in applying the impact-echo method to concrete, a material with a Poisson's ratio of approximately 0.2 in the elastic range. For a Poisson's value of 0.2, the S-wave speed is 61% of the P-wave speed; this ratio is significantly different than that in aluminum. This difference affects the relative arrival times of the wavefronts. For comparison, the displacement patterns obtained from planar disk-shaped flaws in plates having elastic properties representative of concrete are presented.

#### 6.4.2 Flaws in Concrete

In this discussion, the following results are presented: displacement time-histories obtained on the top surface of the flaw, directly under the point of impact, and at a point on the top surface of the plate, near the point of impact; and, displacement and stress fields recorded at successive times to show the interaction of transient stress waves with a planar flaw.

In the analyses presented in this section, the concrete was modeled as a linearly-elastic, homogeneous solid, with the following material properties: a modulus of elasticity of  $3.31 \times 10^7$  kPa; a Poisson's ratio of 0.2; and, a density of  $2300 \text{ kg/m}^3$ . These values resulted in P-, S-, and R-wave speeds of 4000, 2440, and 2240 m/s, respectively. In the region above and near the edge of the flaw, 5-mm square elements were used in the finite element model.



#### 6.4.2.1 Displacement Waveforms

An analysis was performed for a planar, disk-shaped void in a 0.5-m thick concrete plate. The diameter and the depth of the flaw were both 0.2 m for a D/T value of 1, as in the analyses of the flaws in aluminum. The time history of the impact load was a half-sine curve with a 16  $\mu$ s contact time. The arrival time of the 2P-wave reflected from the flaw was 100  $\mu$ s, which resulted in a  $t_c/t_{2p}$  value equal to 0.16, as in the analyses of flaws in aluminum.

Displacement waveforms obtained at the center of the top surface of the flaw and at a point on the top surface of the plate, 0.05 m from the impact point, are shown in Figs. 6.10(a) and (b), respectively. Wave arrival times are indicated on the waveforms. The displacement caused by each wave is the same as has been discussed; however, since there is less difference between the P- and S-wave speeds, wave arrivals in concrete are more closely spaced than in aluminum. Thus, the displacement waveforms obtained from the concrete specimen are different from those previously shown for the same flaw in aluminum. For example, compare the displacement pattern in Fig. 6.9(a) with that in Fig. 6.10(a). In the concrete specimen, the  $P_dS$ -wave arrives somewhat later than the S-wave, rather than at approximately the same time as in the aluminum plate; thus, the large upward displacement caused by the  $P_dS$ -wave is easily identified in Fig. 6.10(a). As in aluminum, if the response obtained from the concrete plate containing the disk-shaped flaw is compared to the response obtained from a solid concrete plate (such as in



Fig. 4.5), the effects caused by diffracted waves are clearly evident. Diffracted waves produce more frequent fluctuations in the displacement and they move the surface above its undisturbed position. For the top surface displacement shown in Fig. 6.10(b), the most noticeable effect due to diffracted waves is the large upward surface displacement caused by the arrivals of the  $P_dS$ - and  $S_dP$ -waves.

In Fig. 6.10(b), there is a period after the arrival of the R-wave when the displacement appears to oscillate about its undisturbed position. These oscillations are due to the numerical ringing which occurs due to excitation of the zero energy modes of the constant strain finite elements.

#### 6.4.2.2 Displacement and Stress Fields

An analysis was performed for impact on a 0.5-m thick, 1.5-m diameter, concrete plate containing a disk-shaped void. The void was 0.01-m thick and 0.1 m in diameter; it was located 0.25 m below the top surface of the plate, resulting in a D/T value of 0.4. The contact time of the impact was 20  $\mu$ s. The arrival time of the 2P-wave reflected from the top surface of the void was 125  $\mu$ s for a  $t_c/t_{2P}$  value of 0.16.

The right sides of part (a) in Figs. 6.11 through 6.14 show vector plots of the displacement fields in the plate 65, 80, 95, and 125  $\mu$ s after the start of the impact. The corresponding positions of the P-, S-, mode-converted, and diffracted wavefronts are shown on the left side of part (a) of each figure. Part (b)

of each figure shows a contour plot of minimum principal (compression) stress.

The P-wavefront arrives at the flaw at  $62.5 \mu\text{s}$ , and is incident upon the edge of the flaw at  $64 \mu\text{s}$ . At  $65 \mu\text{s}$ , the stress contours in Fig. 6.11(b) show that diffraction of the P-wave is occurring; the  $P_dP$ -wavefront is beginning to emerge from the edge of the flaw. The S-wavefront has traveled approximately two-thirds of the distance to the flaw. Rays emanating from the impact point and intersecting the edges of the flaw delineate the shadow zone beneath the flaw. Only diffracted waves can penetrate this zone.

Fig. 6.12 shows the displacement and stress fields at  $80 \mu\text{s}$ . The front of the reflected P-wave (2P) is just overlapping the front of the direct S-wave. The top surface of the flaw is displaced downward because of the effects caused by the direct P-wave. The diffracted  $P_dP$ -waves have overlapped in the center region of the plate, above and below the flaw; thus, the entire shadow zone is stressed. Close inspection of Fig. 6.12(a) shows that the displacement vectors in the diffracted  $P_dP$ -waves are oriented in spherical patterns emanating from the edges of the flaw. The direction of displacements of the vectors in the  $P_dP$ -waves is outward, away from the edges of the flaw. The stress contours in Fig. 12(b) show that the  $P_dP$ -wave is a compression wave.

At  $95 \mu\text{s}$  (Fig. 6.13), the P-wave has completely passed the flaw. This wavefront is now formed by the  $P_dP$ -wavefront in the shadow zone and the original P-wavefront outside the shadow zone. Note that the part of the wavefront formed by the diffracted waves

is no longer spherical. Reflection and diffraction of the P-wave are occurring.

Fig. 6.14 shows the displacement and stress fields at 125  $\mu$ s. The 2P-wave reflected from the surface of the flaw arrives at the top surface of the plate. The PS-wave produced by mode-conversion of the P-wave incident upon the flaw has traveled approximately 60 percent of the distance from the flaw to the top surface of the plate. Reflection and diffraction of the S-wave by the flaw has occurred. The P-wave has reformed below the flaw. The P-wavefront is nearing the bottom surface of the plate.

Compare Fig. 6.14 to Fig. 4.6 which shows the displacement and stress fields in a solid, 0.5-m thick, plate at 125  $\mu$ s. In the plate containing the flaw (Fig. 6.14) diffracted waves allowed the P- and S-wavefronts to penetrate the shadow zone. Thus, the displacement and stress fields produced by the P- and S-waves in the plate containing the flaw are similar to those in the solid plate (Fig. 4.6). However, in the fields obtained from the plate containing the flaw, the displacement and stresses caused by the waves produced by the interaction of the P- and S-waves with the flaw are also present. These waves will reflect from the surfaces of the plate and interact with the flaw producing new reflected and diffracted waves. In addition, subsequent interactions of the reflected P- and S-waves with the top and bottom surfaces and the edges of the flaw will result in new reflected and diffracted waves. Thus, the presence of the flaw greatly complicates the displacement and stress fields.

A displacement waveform recorded near the point of impact at the top surface of a plate containing a flaw consists of displacement caused by waves reflected and diffracted from the flaw and waves reflected from the bottom surface of the plate and subsequently diffracted by the flaw. Multiple reflections and mode-conversions of all these waves occur, complicating the displacement waveform. The relative importance of the effects caused by each of these phenomena on surface displacement waveforms depends on the flaw geometry and on the test conditions.

## 6.5 THE EFFECT OF TEST VARIABLES ON IMPACT-ECHO WAVEFORMS

To better understand how surface displacement waveforms are affected by flaw geometry and test conditions, parameter studies were carried out. The variables examined are shown in Fig. 6.2; they include: the contact time of the impact; the diameter and the depth of a flaw; and, the test configuration, that is, the point where the displacement is recorded.

### 6.5.1 Contact Time of the Impact

As discussed in Chapter 5 (Section 5.4.1), the frequency content of the stress waves produced by impact depends on the contact time of the impact. As was shown in Fig. 5.4, a shorter contact time produces a broader range of frequencies in the waves; however, the amplitude of each component frequency is lower. Waves produced by a long contact time are made up primarily of large amplitude, low frequency components. This is important because it is the



frequency content of the waves produced by impact that determines the size of the flaw that can be detected. For a flaw to be detected, it is generally stated that the dimensions of the flaw must be on the order of, or larger than, the component wavelengths in the propagating waves. (This general rule will be referred to as the "one-wavelength" criterion.) Higher frequency components have shorter wavelengths; thus, waves containing higher frequencies are reflected by smaller flaws. However, high frequency waves have less penetrating ability, as they are attenuated more quickly than low frequency waves in a heterogenous material such as concrete.

Three analyses of a 0.5-m thick concrete plate containing a disk-shaped flaw were carried out. The variable in the analyses was the contact time of the impact. The test configuration is shown in Fig. 6.2. The flaw diameter was 0.2 m and it was located 0.13 m below the top surface of the plate (D/T value of 1.54). The separation between the impact point and the point where the waveform was recorded was 0.02 m (H/T value of 0.15). The contact times of the impacts were 20, 40, and 80  $\mu$ s.

Using the "one-wavelength" criterion, a 0.2-m diameter flaw will reflect frequencies having wavelengths on the order of, or greater than, approximately 0.2 m; therefore, for the flaw to be detected, sufficient energy must be contained in the frequencies approximately equal to and greater than 40 kHz. The normalized amplitude spectrum of the force-time history of a half-cycle sine curve (Fig. 5.4) can be used to determine the frequency content of the various impacts. By multiplying the horizontal axis by each



contact time, it is found that the 20, 40, and 80  $\mu\text{s}$  duration impacts have a first zero amplitude at 75, 37.5, and 18.75 kHz, respectively. Figs. 6.15(a)-(c) show the surface displacement waveforms obtained from the plate for each of these contact times. Wave arrival times are indicated on the waveforms. Notice that in all three waveforms, regardless of the contact time, effects caused by the diffracted waves cause the surface to be displaced above its undisturbed position, indicating that a flaw is present.

A 20- $\mu\text{s}$  duration impact results in a combination of conditions which allow displacements caused by specularly reflected, mode-converted, and diffracted waves to be identified in the waveform shown in Fig. 6.15(a). These conditions are as follows: A large amount of the total energy is contained in frequencies in the range of 40 kHz and higher; thus, a large portion of the energy in the pulse is reflected by the flaw. The arrival of the first reflection from the flaw (2P-wave) occurs at 100  $\mu\text{s}$ . This results in a  $t_c/t_{2p}$  value of 0.32. As discussed in Chapter 5, a small  $t_c/t_{2p}$  value means that the contact time is short enough relative to the time of the arrival of the first internal reflection (2P-wave) so that the displacement pattern produced by internal reflection is not masked by the R-wave arrival. In this case, the perturbations in the waveform can be used to accurately determine the depth of the flaw.

In the surface displacement produced by a 40- $\mu\text{s}$  duration impact (Fig. 6.15(b)), P-wave arrivals from the flaw dominate the response. The waveform is smoother, as the displacements caused

by diffracted waves are masked by the general smoothing effect of a longer duration impact (see Section 5.3.2). A contact time of 40  $\mu\text{s}$  results in a  $t_c/t_{2p}$  value of 0.64. This is twice as large as in the previous case; however, the R-wave does not interfere with the displacement pattern produced by internal reflections. There is still good agreement between calculated P-wave arrival times and the large downward displacements in the waveform; thus, the depth of the flaw can be accurately determined from a time domain analysis. The diameter of the flaw cannot be determined in this case because the arrival of diffracted waves from the edges of the flaw cannot be identified.

Fig. 6.15(c) shows the surface displacement waveform produced by an 80- $\mu\text{s}$  duration impact. In this case,  $t_c/t_{2p}$  is equal to 1.3; the duration of the impact is longer than the arrival time of the 2P-wave. The initial part of the displacement pattern produced by internal reflections from the flaw is lost in the surface response to the large amplitude R-wave, and there is no agreement between the perturbations in the waveforms and calculated wave arrival times. However, because of effects caused by diffraction which push the surface displacement above its undisturbed position, the presence of the flaw can still be detected, even though the depth of the flaw cannot be determined from a time domain analysis.

In summary, as the contact time of the impact increases and more of the energy produced by impact is contained in the low frequency components of the input pulse, the following trends are observed: 1) The displacement response becomes smoother; 2) Surface

displacements caused by the R-wave begins to mask the displacements caused by internal reflections from the flaw; and, 3) Calculated wave arrival times do not agree with the perturbations in the waveforms.

#### 6.5.2 Ratio of Flaw Diameter to Flaw Depth

Figs. 6.16(a)-(d) show surface displacement waveforms obtained from 0.05, 0.1, 0.2, and 0.4 m diameter, disk-shaped flaws which were located 0.2 m below the top surface of a 0.5 m thick concrete plate. Flaw geometries are shown schematically on the left of each figure. These flaw geometries resulted in D/T values of 0.25, 0.5, 1, and 2, respectively.

In each analysis, the spacing between the impact point and the receiver was 0.05 m; that is for each flaw geometry, the waveform was recorded at the same point on the top surface of the plate. Thus, the position of the receiver relative to the edge of the flaw was different in each case: for the 0.05 m diameter flaw (Fig. 6.16(a)), the waveform was recorded off the edge of the flaw; for the 0.1 m diameter flaw (Fig. 6.16(b)), the waveform was recorded directly over the edge of the flaw; for the larger flaws (Figs. 6.15(c) and (d)), the waveforms were recorded over the flaw. The point where the waveform was recorded relative to the location of the flaw is important, as it will affect the amplitude and arrival times of the various echoes produced by the flaw. This parameter will be studied in more detail in the following section.

The contact time of the impact was 16  $\mu$ s ( $t_c/t_{2p}$  value of

0.16)). Wave arrival times are indicated on the waveforms. The following paragraphs discuss the effects on the surface displacement waveforms caused by increasing the flaw diameter.

As flaw diameter increases at a given depth (Fig. 6.16(a) to (d)), the arrival times of diffracted waves change relative to the arrival times of specularly reflected and mode-converted waves. The larger the diameter of the flaw, the greater the time lag between the arrival of the specular reflection produced by an incident wave and the diffracted waves produced by the same wave. Therefore, as the diameter increases, the superposition of displacements caused by specular, mode-converted, and diffracted waves is different.

The amplitude of specularly reflected waves increases as the size of the flaw increases. This increase in amplitude results from the fact that a larger flaw reflects a greater range of frequencies. For flaws having diameters of 0.05, 0.1, 0.2, and 0.4 m, frequencies in the range of and greater than 80, 40, 20, and 10 kHz, respectively, will be reflected. For a contact time of 16  $\mu$ s, the first zero amplitude in the spectrum occurs at a frequency of 93.7 kHz. Thus, as the diameter of the flaw decreases from 0.4 m to 0.05 m, the amount of energy reflected by the flaw decreases significantly, until, for the smallest flaw (Fig. 6.16(a)), displacement caused by wave arrivals from the flaw are difficult to distinguish from the noise (numerical in this case). Reflections from this small flaw are also difficult to discern because the waveform was recorded at a point off the edge of the flaw. For this particular test configuration (impact point and the point where



the displacement was recorded are equally distant from the edge of the flaw), only diffracted waves from the flaw contribute to the surface displacement waveform.

The amplitude of diffracted waves depends, in part, on the position of the edges of the flaw with respect to the radiation pattern of the incident waves. As was mentioned in Chapter 4, the radiation pattern for P- and S-waves (Fig. 4.2) shows that the amplitude of the displacements in the P-wave is greatest at the center of the wavefront and gradually decrease along rays located at increasing angles from the centerline of the plate; displacements in an S-wave are zero at the center of the wavefront and increase to a maximum along rays located at approximately 40 degrees from the centerline of the plate (Poisson's ratio equal to 0.2). Therefore, a P-wave incident upon the edges of a small flaw, such as the 0.05 m and 0.1 m diameter flaws shown in Figs. 6.16(a) and (b), will produce large amplitude diffracted waves, while an S-wave incident upon the same flaws will produce diffracted waves of much lower amplitude. The edges of these small flaws (Figs. 6.16(a) and (b)) intersect rays located at 7.1 and 14 degrees from the centerline of the plate. In contrast, the 0.2 and 0.4 m diameter flaws (Fig. 6.16(c) and (d)) have edges intersecting rays located at 26.6 and 45 degrees from the center of the wavefront. In these cases, the amplitude of displacements in the diffracted waves produced by an incident S-wave will be near maximum; however, the amplitude of the displacements in the diffracted waves produced by an incident P-wave will be less than for a smaller diameter flaw.



In addition, each diffracted wave also has its own radiation pattern. (Radiation patterns have not been calculated for transient waves, but it can be assumed that they are similar to those for harmonic waves, just as the radiation patterns for P- and S-waves produced by a harmonic source were similar to those produced by a transient point source.) Thus the amplitude of the surface displacement caused by a diffracted wave will also depend upon where the displacement is being monitored relative to the edge of a flaw.

To show the effect of increasing depth on surface displacement waveforms, an analysis was carried out for a 0.1 m diameter flaw located 0.4 m below the top surface of the plate (D/T value of 0.25). All other parameters were the same as those shown in Fig. 6.16(b). The value of the  $t_c/t_{2p}$  ratio and the magnitude of the impact force-time history were also the same as in the previous analyses.

Fig. 6.17 shows the displacement waveform obtained from this analysis; for this flaw geometry the waveform was recorded directly over the edge of the flaw. Wave arrivals are difficult to identify in this waveform. Divergence due to beam spreading causes spherical waves to undergo attenuation at the rate inversely proportional to the distance traveled (Section 2.1.6). Compare this waveform to the waveform obtained from the 0.1 m flaw located at a depth of 0.2 m (Fig. 6.16(b)). By increasing the depth of the 0.1 m diameter flaw by a factor of two, the amplitude of reflected waves arriving at the top surface of the plate is reduced by a factor of two, making it difficult to detect a flaw that was easily detected at the shallower depth.

The flaw located at a depth of 0.4 m has a  $D/T$  value of 0.25, which is equal to the  $D/T$  value of the 0.05 m flaw shown in Fig. 6.16(a); both are difficult to detect. Thus, for a given duration impact, the  $D/T$  value is a useful parameter for determining whether a flaw can be detected. Additional studies showed that for a given depth,  $T$ , the critical value of the diameter,  $D$ , increases as the contact time of the impact increases. Thus, these three variables are integrally related.

### 6.5.3 Test Configuration

As mentioned in the previous section and in Section 5.3.2.2, surface displacement waveforms are affected by the test configuration; that is, they are affected by the locations of the impact point and the point where the displacement is being recorded relative to the location of a flaw. To study the effect of test configuration on displacement patterns, surface displacement waveforms were obtained at various distances ( $H$ ) from the impact point by recording the time-history of the displacements at nodes along the surface of the finite element model. Flaw diameter was 0.2 m and flaw depth was 0.2 m, giving a  $D/T$  value of 1. The contact time of the impact was 16  $\mu$ s.

Figs. 6.18(a)-(c) show displacement waveforms obtained for the following  $H$  values: 0.025, 0.10, and 0.15 m, respectively. The waveform shown in Fig. 6.18(a) was obtained at a point located over the flaw near the impact point; Fig. 6.18(b) shows a waveform recorded directly over the edge of the 0.2 m diameter flaw; and

Fig. 6.18(c) shows a waveform obtained at a point that was not located over the flaw. Wave arrival times are indicated on each waveform. The displacement patterns in this series of waveforms are discussed in the following paragraphs.

As  $H$  increases, the time lag between specular reflections and diffracted waves decreases. Each waveform represents the superposition of the displacements caused by both sets of waves; therefore, as  $H$  increases, the displacement pattern in the waveforms gradually changes as the arrival times of specularly reflected and diffracted waves shift relative to each other. In Fig. 6.18(a), specularly reflected and diffracted wave arrivals are distinct, and the displacements caused by each individual arrival can be discerned in the waveform. In Fig. 6.18(c), however, effects caused by specular reflections and the arrival of the corresponding diffracted waves are nearly exactly superimposed in time. For example, the downward displacement caused by the 2P-wave is reduced by the simultaneous arrival of the  $P_dP$ -wave which causes an upward displacement of the plate surface. Similarly, the PS- and  $P_dS$ -waves, and the 2S- and  $S_dS$ -waves arrive at about the same times, and the displacements that occur due to these simultaneous arrivals represent the superposition of the displacements caused by each wave.

The waveform obtained over the edge of the flaw (Fig. 6.16(b)) shows more perturbations than the waveform obtained over the flaw (Fig. 6.18(a)) and the waveform obtained at the point on the surface that was not over the flaw (Fig. 6.18(c)). This characteristic can be used to help locate the edges of a flaw.

As  $H$  increases, the amplitudes of the displacements caused by arrivals of specularly reflected, mode-converted, and diffracted waves change significantly (see Section 5.3.2.2).

## 6.6 SUMMARY AND CONCLUSIONS

This chapter has focused on the interaction of transient stress waves with planar flaws in plates. The elastic responses produced by surface impact on plates containing flat-bottom holes and planar disk-shaped flaws were studied. Surface displacement waveforms obtained from plates containing flaws were compared to waveforms obtained from solid plates to determine how surface displacement patterns are affected by the waves created by diffraction at the sharp edges of a discontinuity. It was shown that the displacement waveforms obtained from a plate containing a flat-bottom hole are very similar to those obtained from a plate containing a planar disk-shaped flaw.

Parameter studies of plates containing planar disk-shaped flaws were carried out to study the effect of test variables on surface displacement waveforms. The following conclusions were made:

- 1) The ratio of flaw diameter to flaw depth ( $D/T$ ) is a useful parameter for characterizing planar flaws. The larger the  $D/T$  value of a flaw, the easier it is to detect the flaw. The critical  $D/T$  value increases as the contact time of the impact increases.

- 2) If the diameter of a flaw is sufficiently large, accurate determination of the depth of a flaw from time domain analysis can



be made using surface displacement waveforms, if the contact time of the impact is less than approximately two-thirds of the time it takes for the first P-wave reflection from the flaw to arrive at the top surface of the plate.

3) A waveform recorded close to the impact is simpler to interpret and allows the most accurate determination of flaw depth.

In Chapters 4 and 6, comparisons of displacement waveforms obtained from finite element analyses to exact and experimentally obtained displacement waveforms established the validity of using finite element analysis for the study of transient wave propagation in elastic solids. This study lays the groundwork for finite element studies of elastic solids of arbitrary geometry and studies of solids containing a variety of types of flaws.

In the following chapter, these numerical studies will be used to help interpret experimental displacement waveforms obtained from controlled flaw studies.



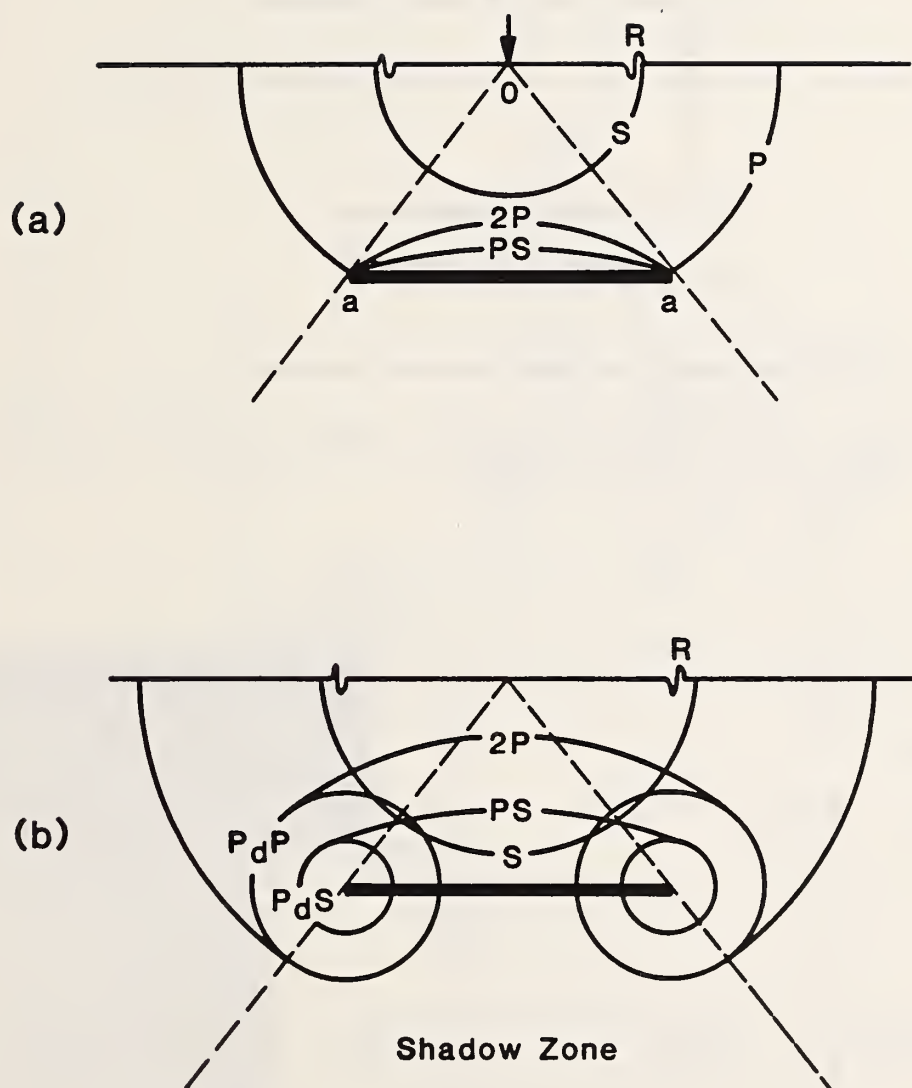


Figure 6.1 Diffraction at the edges of a crack: a) P-ray incident upon the edges of a crack; and, b) cylindrical wavefronts  $P_dP$  and  $P_dS$  emitted from tips.

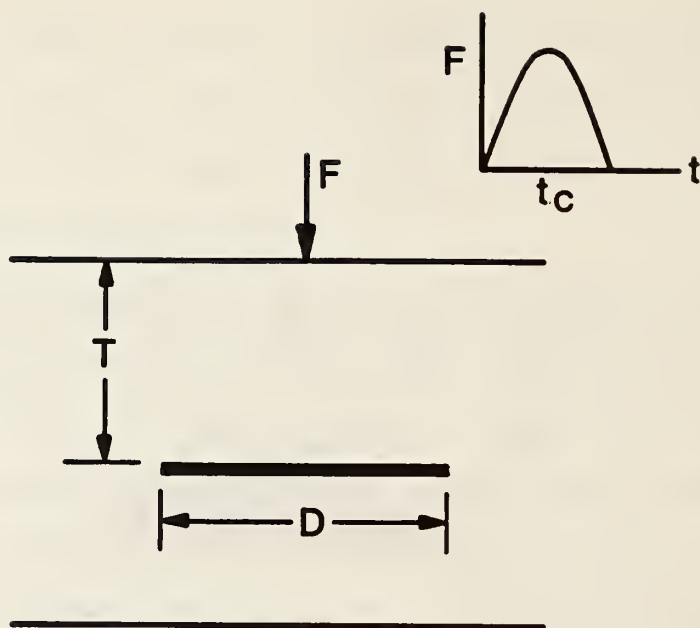


Figure 6.2 The important variables affecting the response of a planar disk-shaped void in a plate.

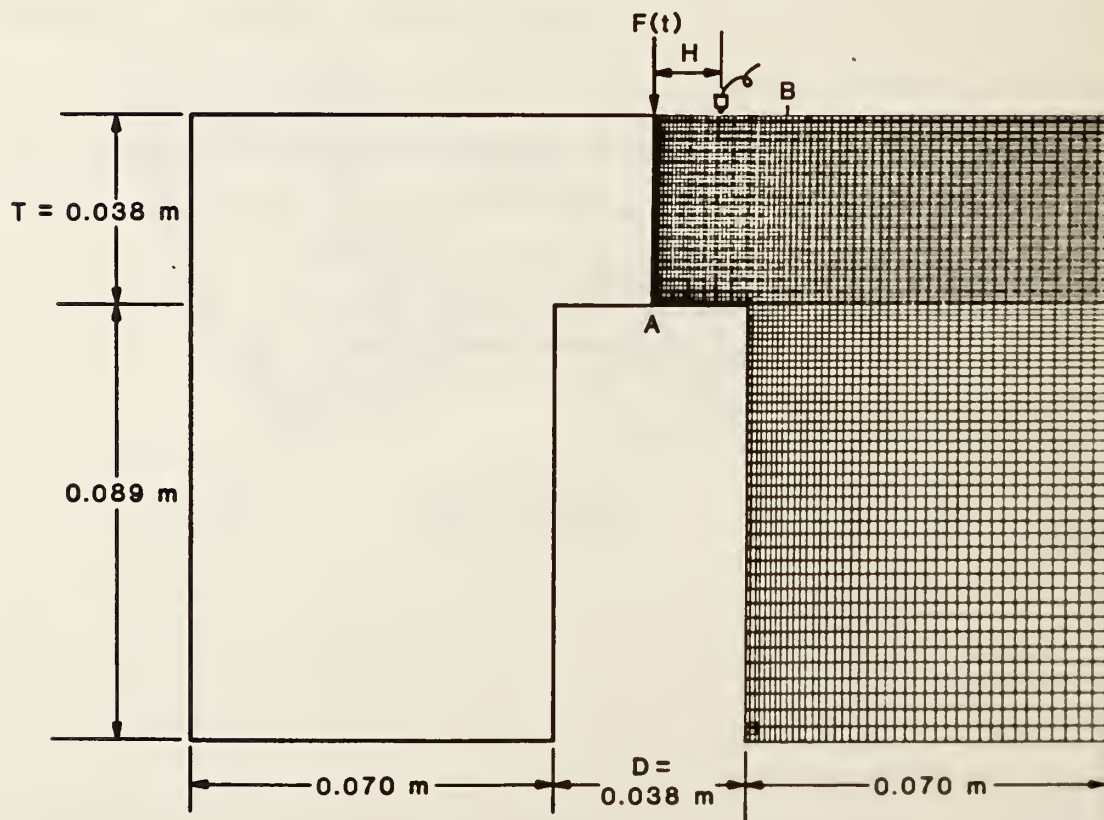


Figure 6.3 Finite element model of a plate with a flat-bottom hole.

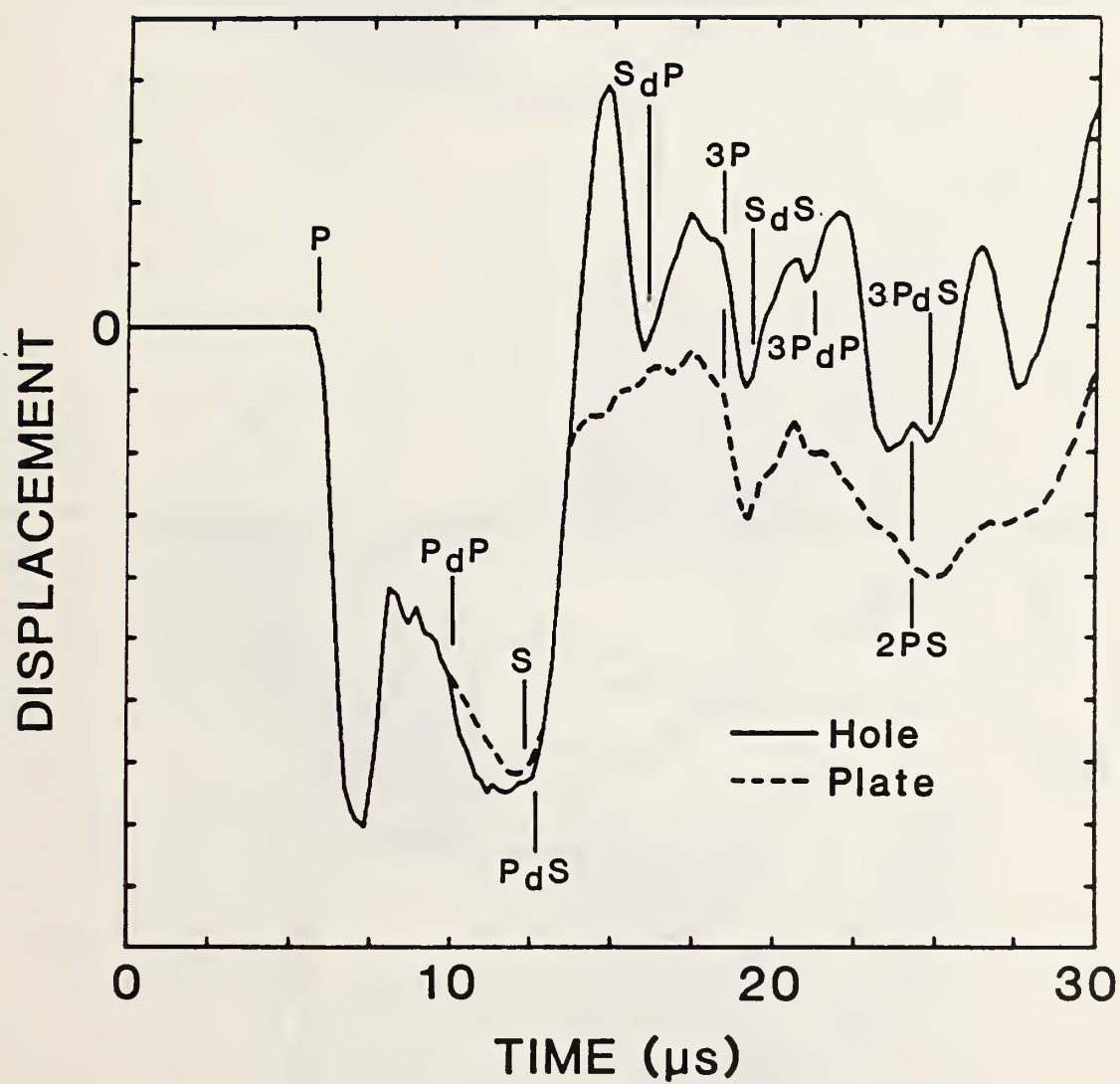


Figure 6.4 Displacement waveforms at the center of the flat-bottom hole and at the epicenter of a solid plate.

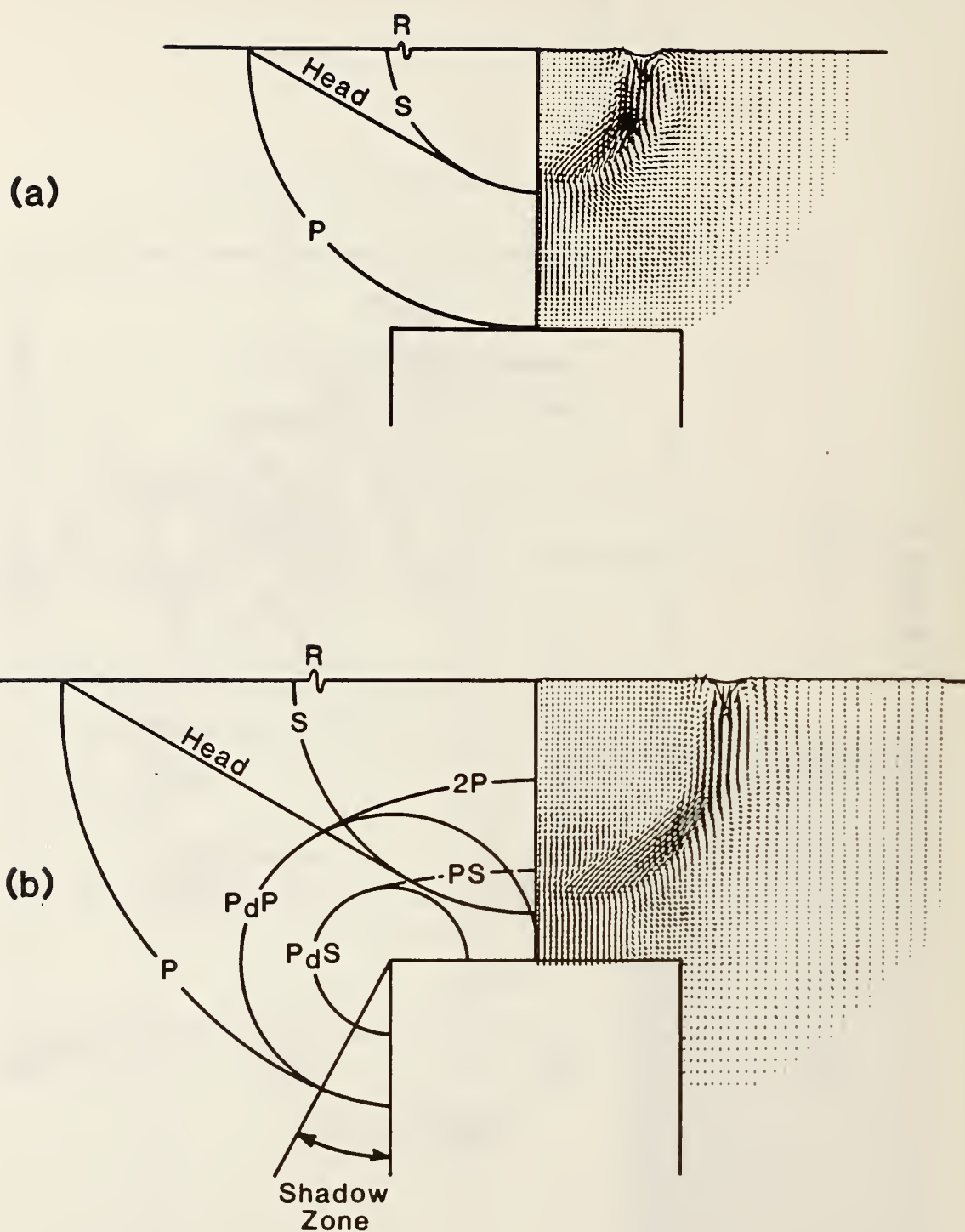


Figure 6.5 Vector plots of the displacement fields in a plate with a flat-bottom hole: a)  $6.1 \mu\text{s}$  after the start of impact; and b)  $10 \mu\text{s}$  after the start of impact.

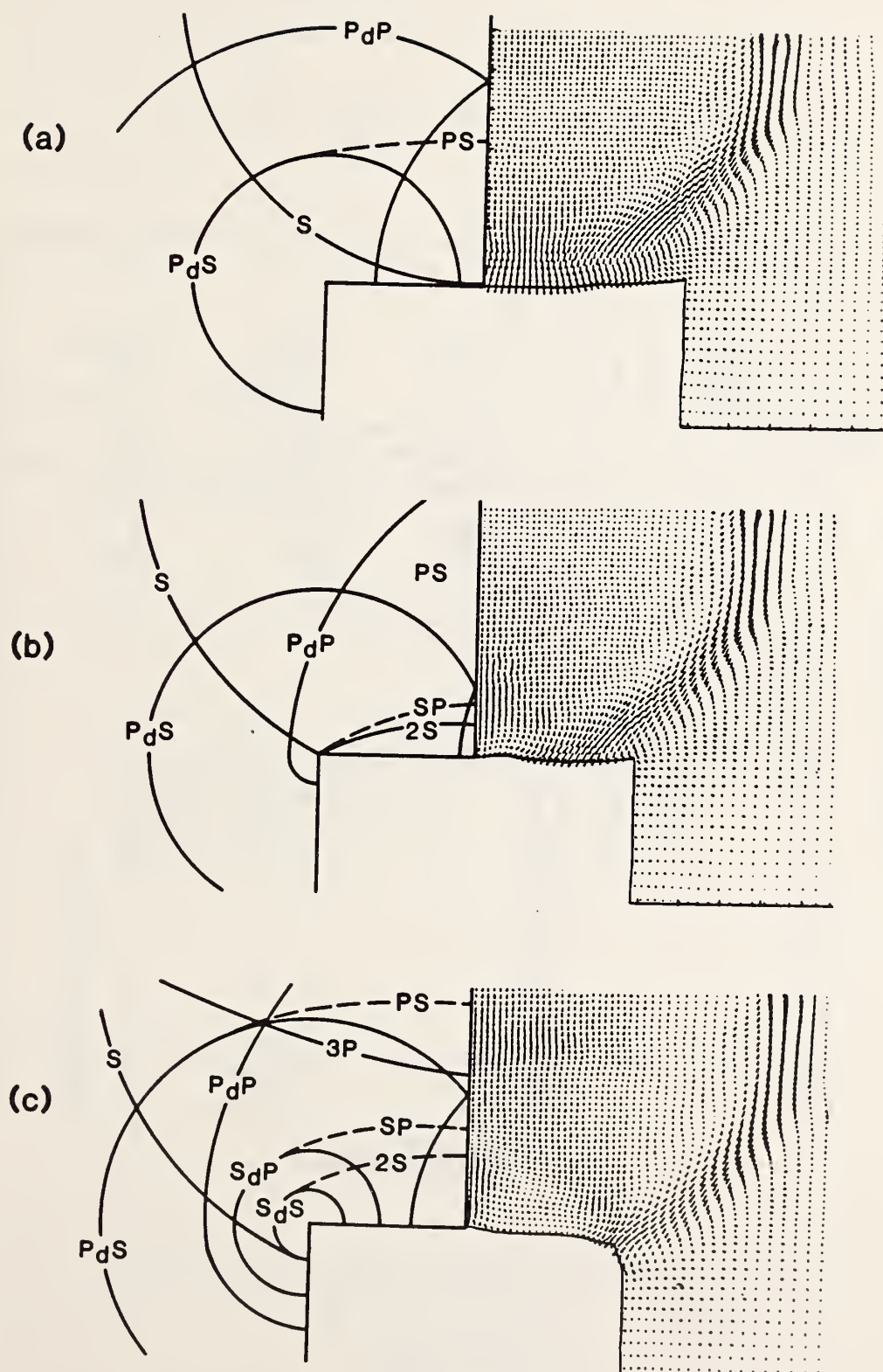


Figure 6.6 Close-ups of vector plots of displacement fields around the flat bottom hole at various times after the start of impact: a) 12  $\mu$ s; b) 13.5  $\mu$ s; and, c) 15  $\mu$ s.



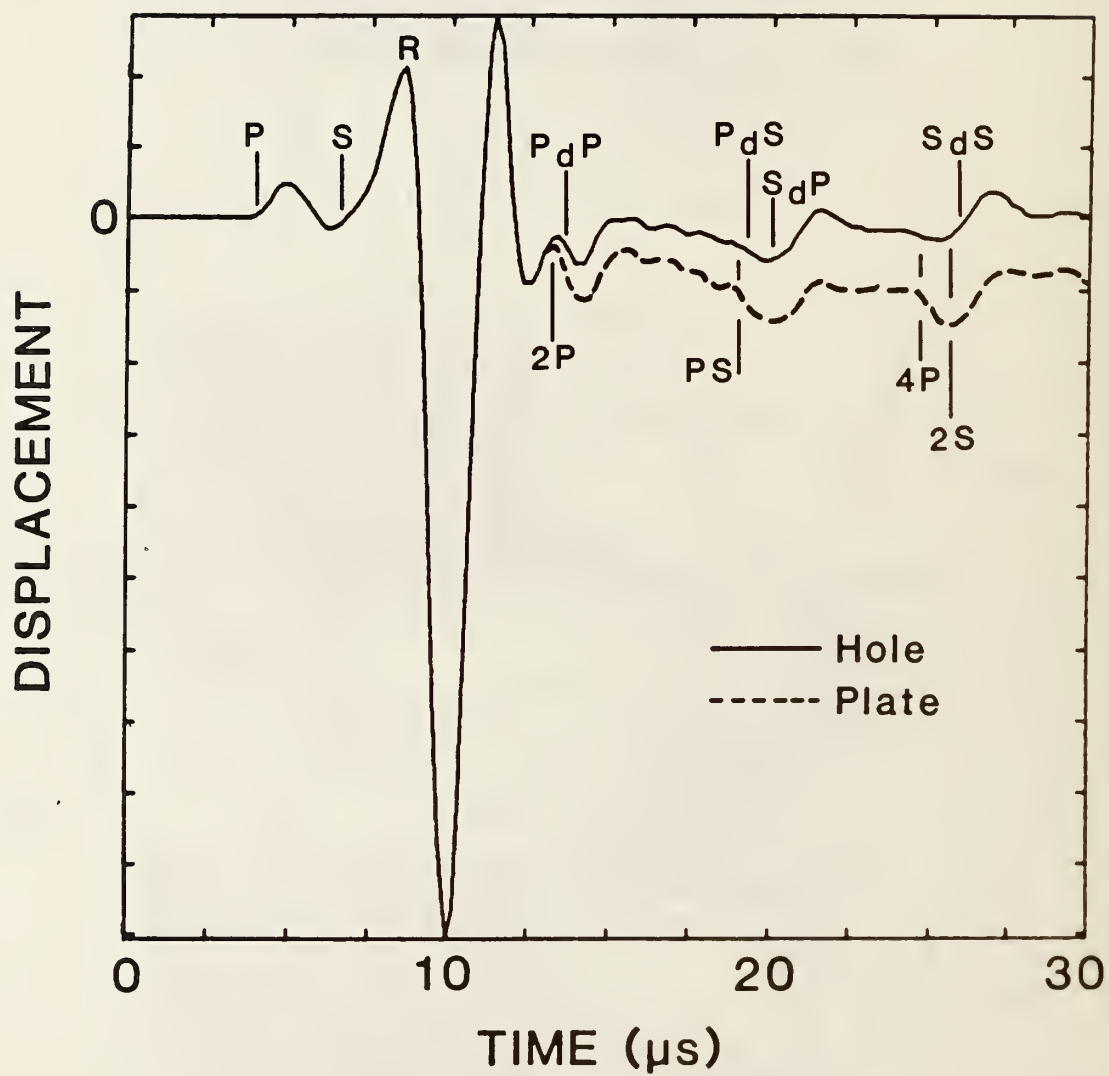


Figure 6.7 Impact-echo displacement waveforms from a plate with a flat-bottom hole and from a solid plate.

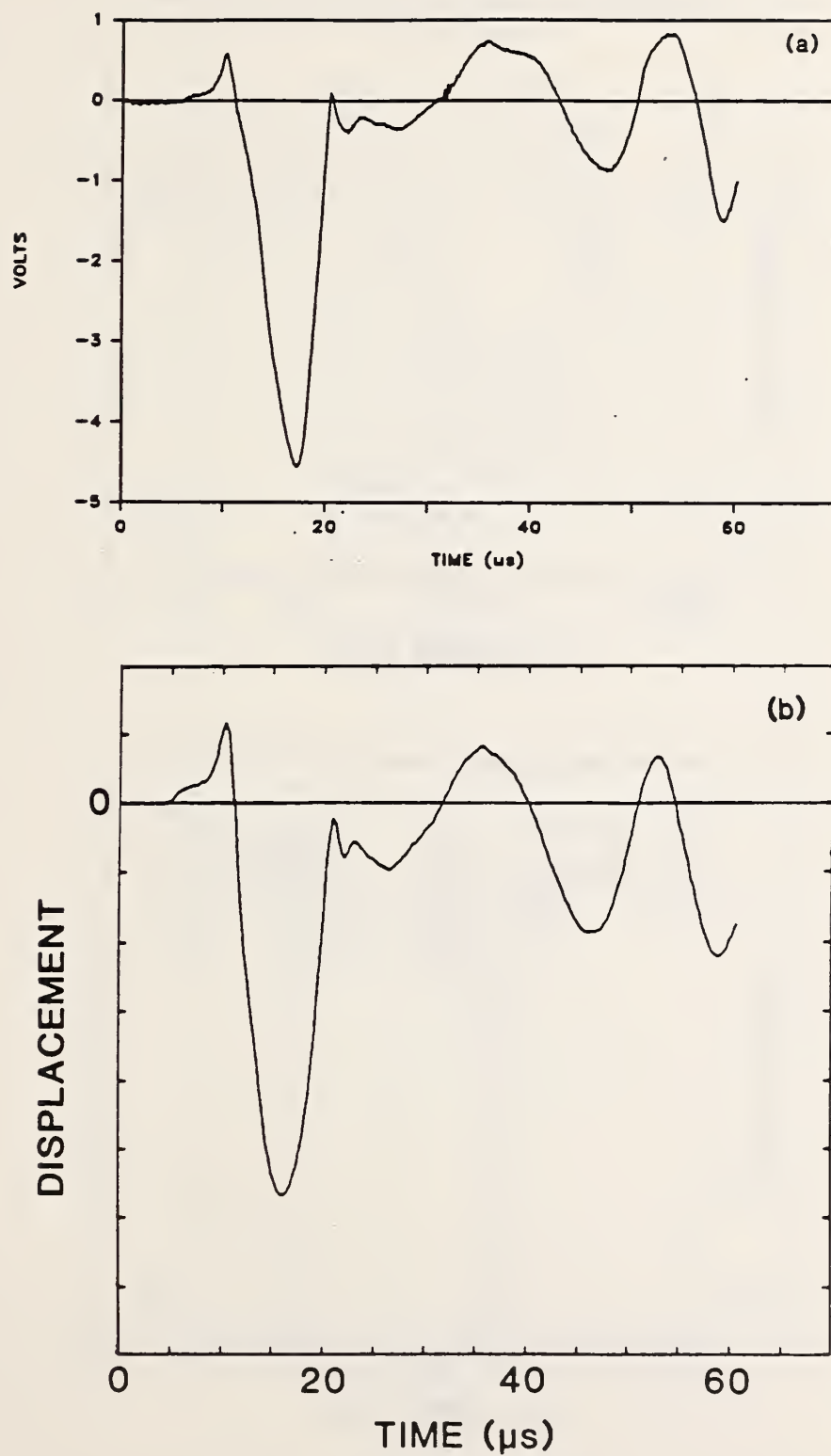


Figure 6.8 Comparison of analytical response with experimentally obtained response for a plate with a flat-bottom hole: a) experimental waveform; and, b) finite element waveform.

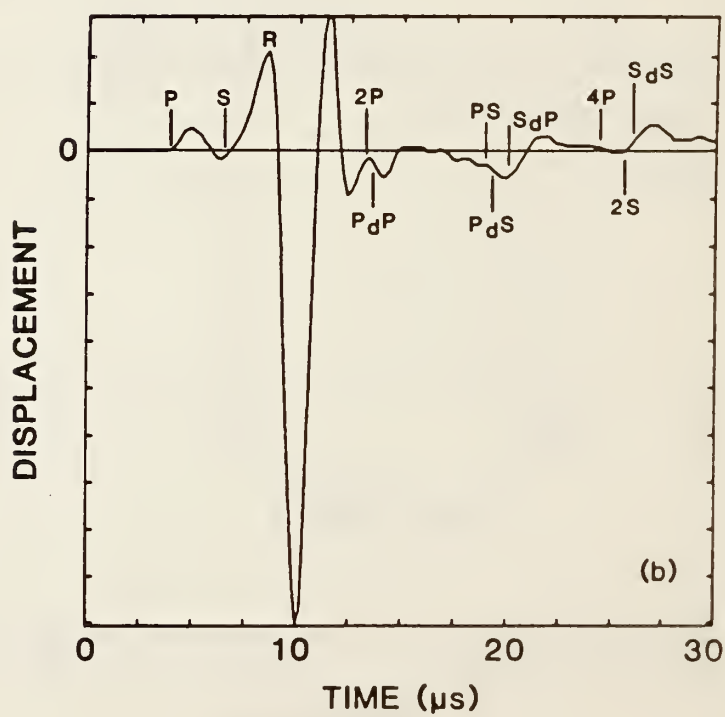
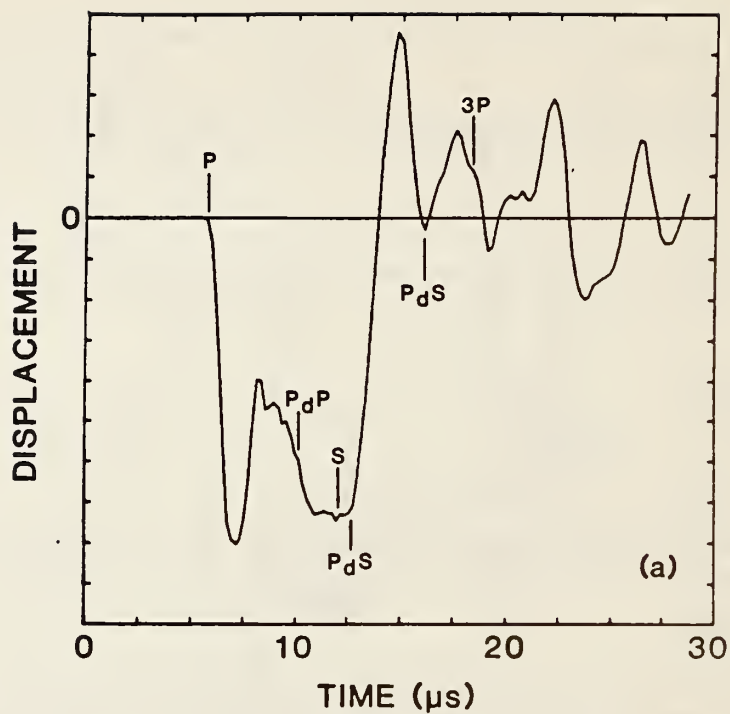


Figure 6.9 Planar disk-shaped flaw in an aluminum plate: a) displacement at the center of the top surface of the flaw; and, b) displacement at a point on the top surface of the plate.

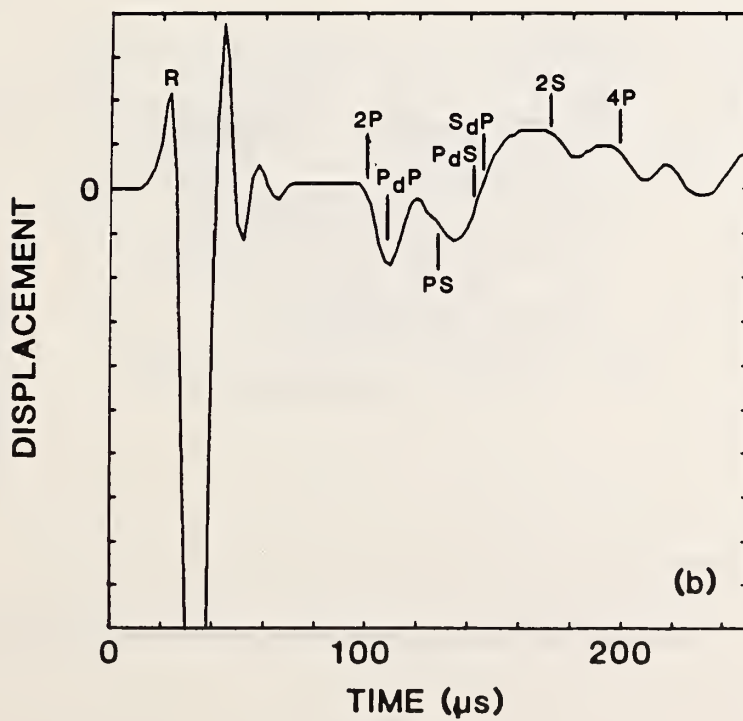
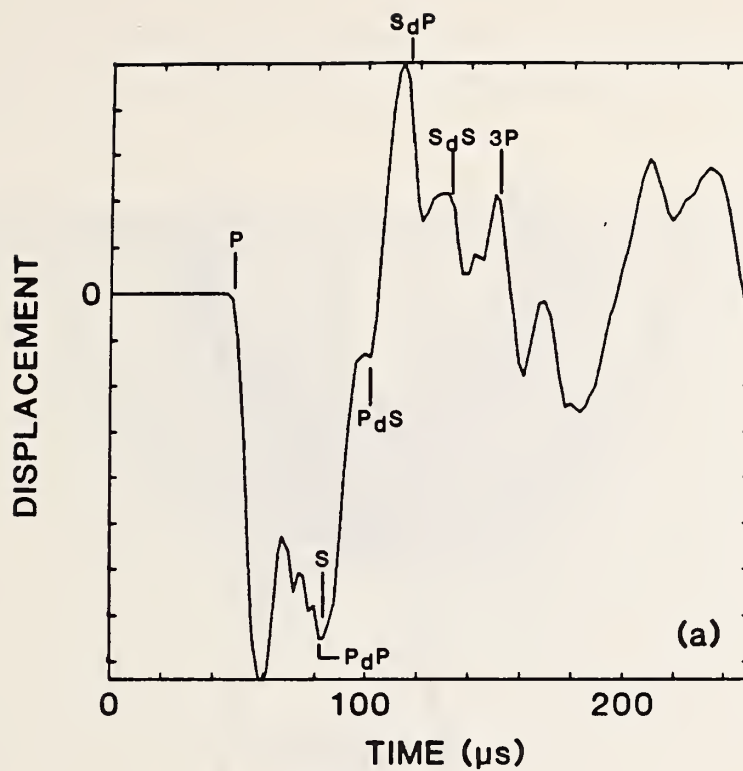


Figure 6.10 Planar disk-shaped flaw in a concrete plate: a) displacement at center of the top surface of the flaw; and, b) displacement at a point on the top surface of the plate.

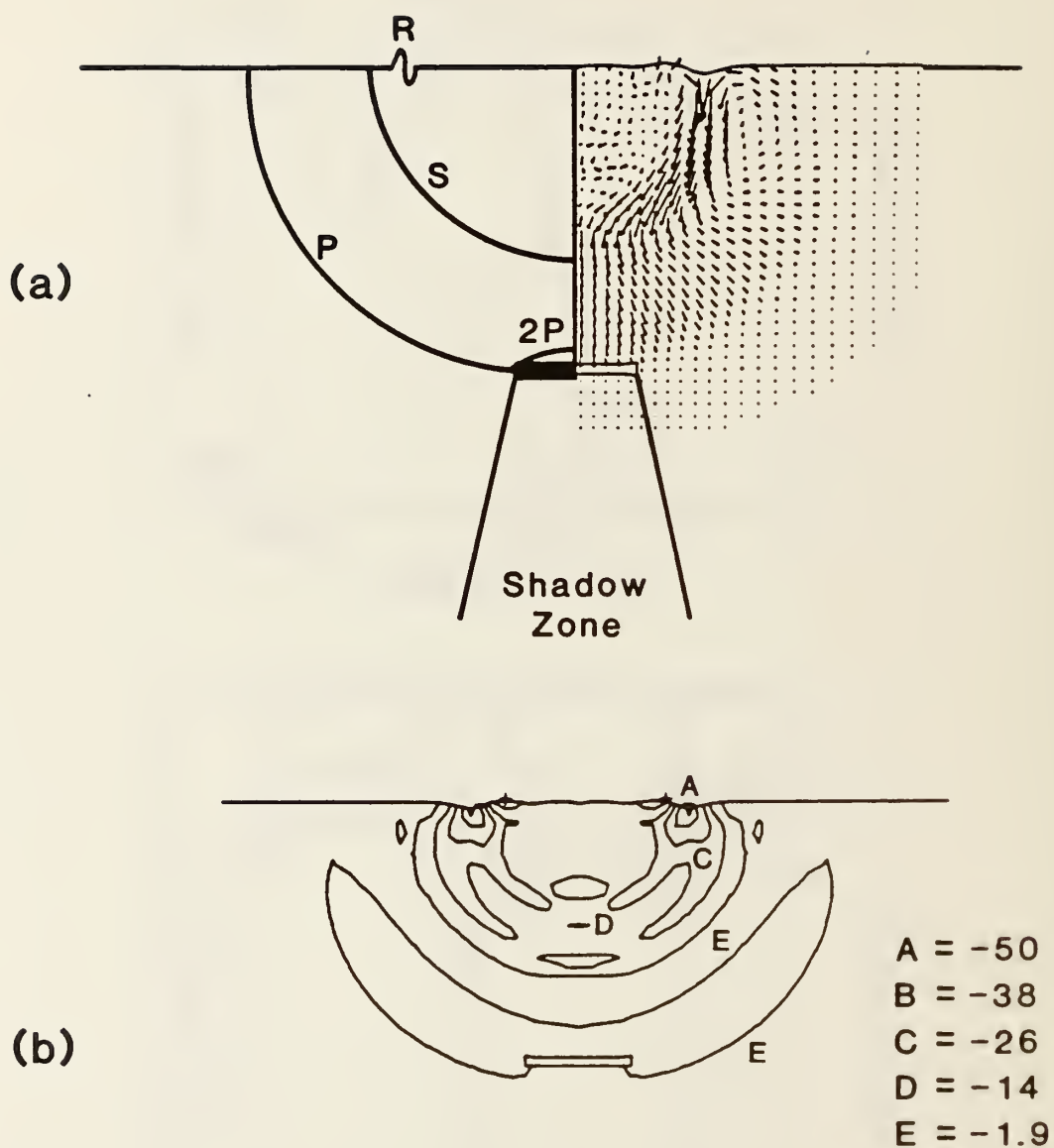


Figure 6.11 Displacement and stress fields in a plate containing a disk-shaped flaw 65  $\mu$ s after the start of the impact.



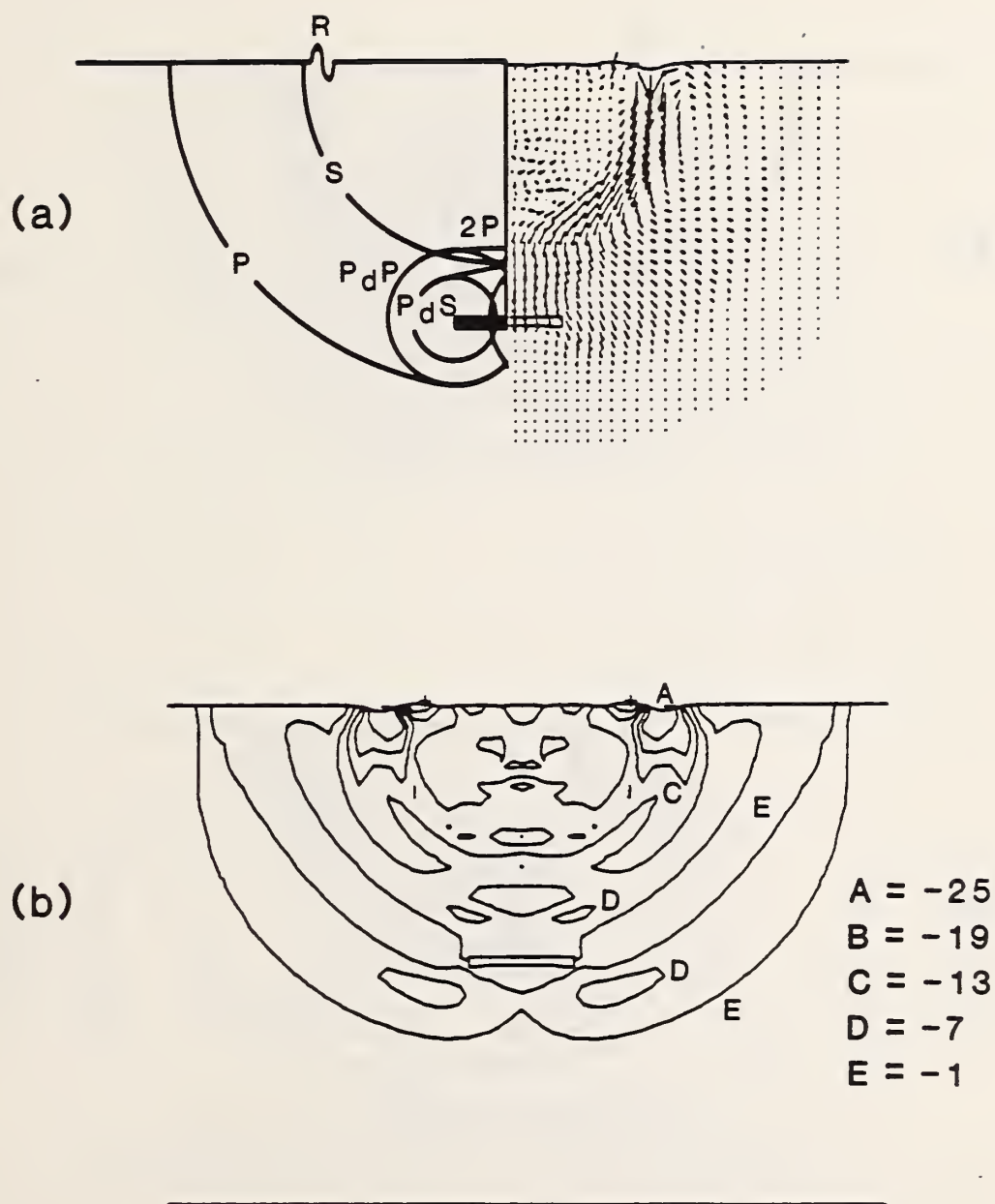


Figure 6.12 Displacement and stress fields in a plate containing a disk-shaped flaw 80  $\mu$ s after the start of the impact.

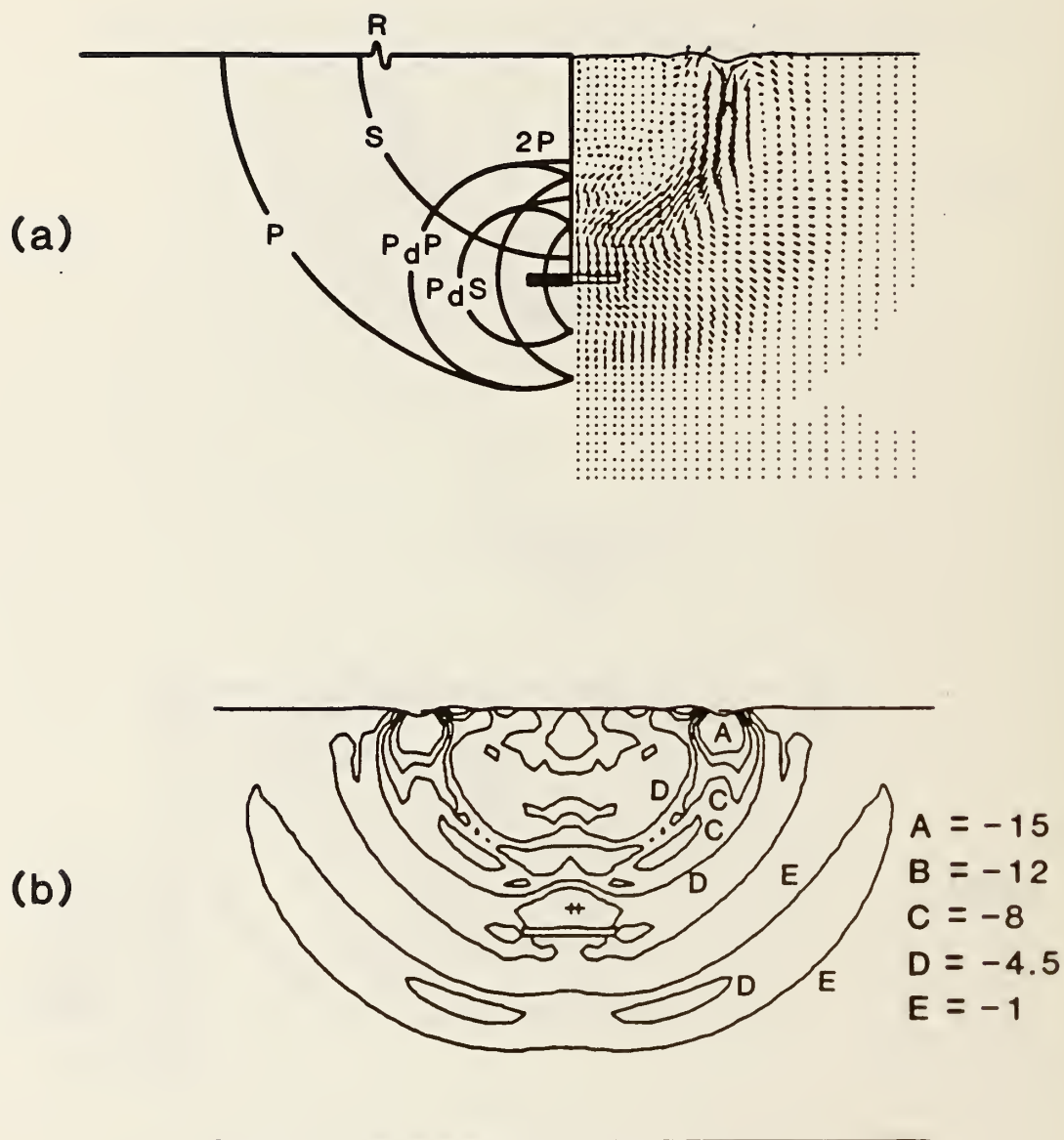


Figure 6.13 Displacement and stress fields in a plate containing a disk-shaped flaw 95  $\mu$ s after the start of the impact.

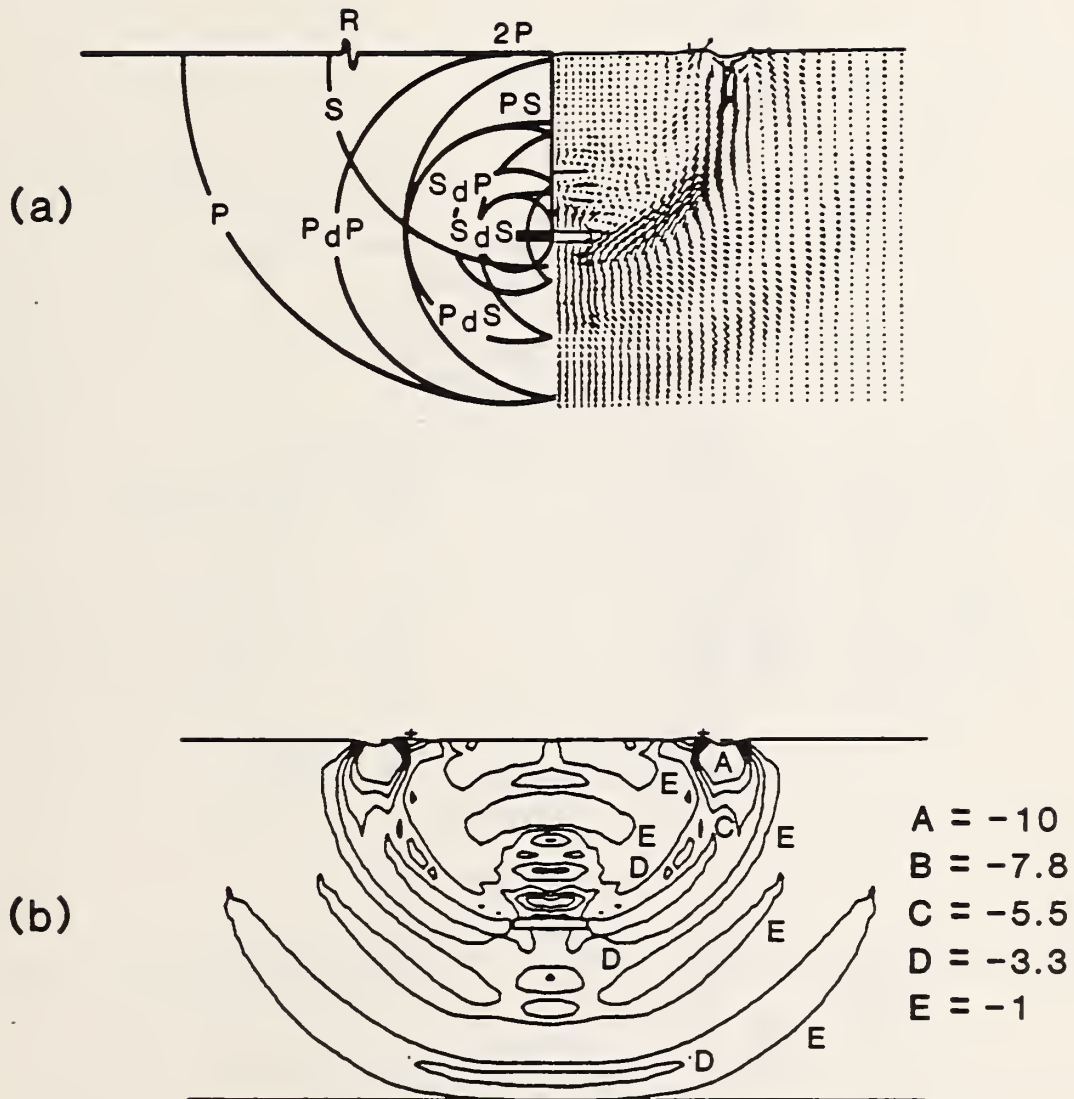


Figure 6.14 Displacement and stress fields in a plate containing a disk-shaped flaw 125  $\mu$ s after the start of the impact.

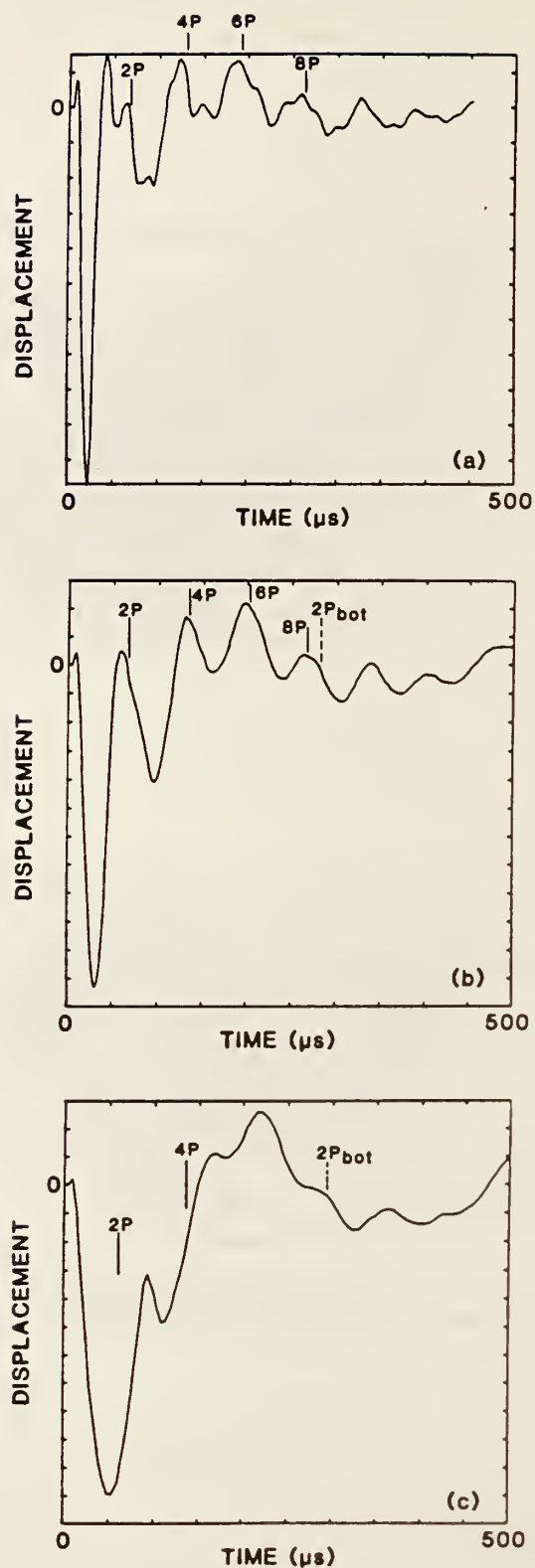


Figure 6.15 The effect on displacement waveforms caused by varying the contact time of the impact: a) 20  $\mu\text{s}$ ; b) 40  $\mu\text{s}$ ; and, c) 80  $\mu\text{s}$ .

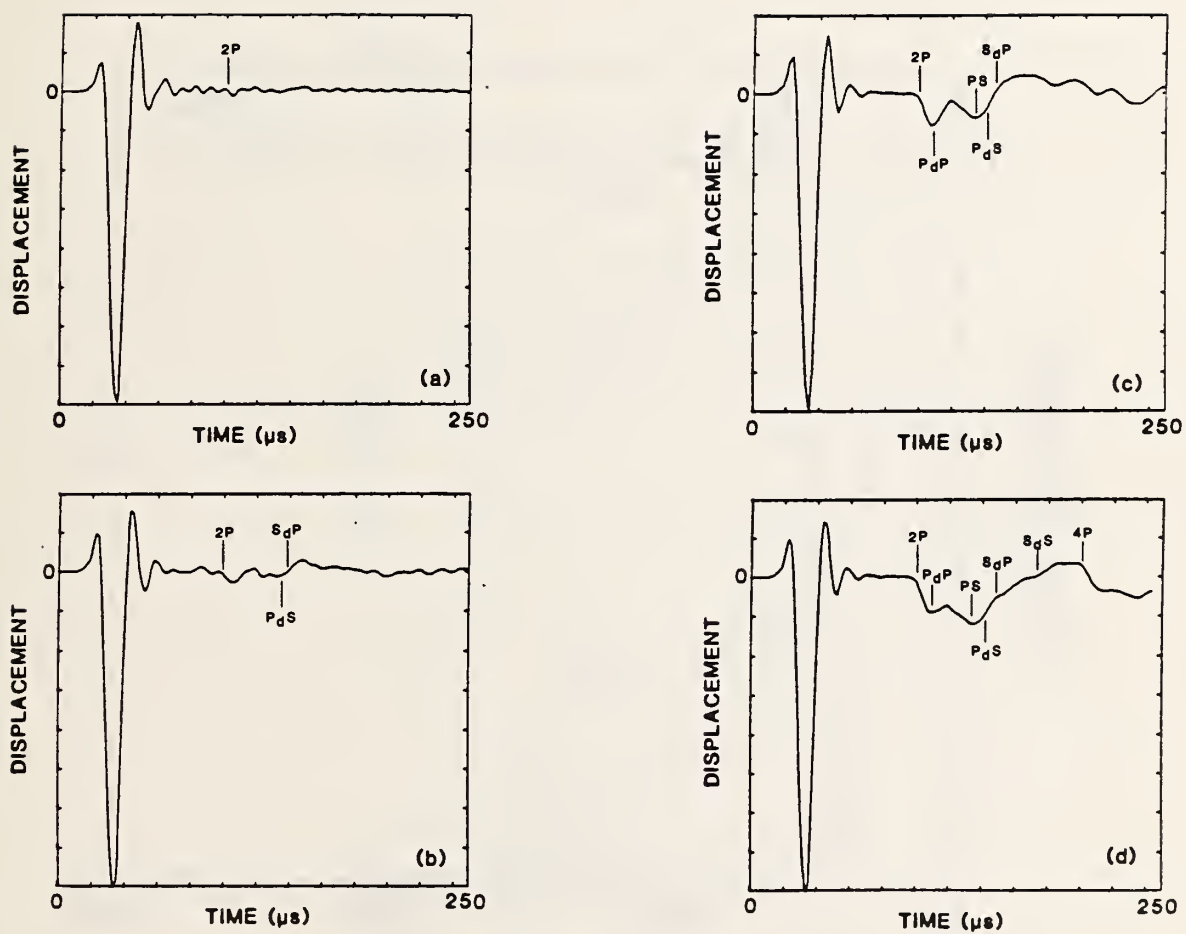


Figure 6.16 The effects on surface displacement waveforms caused by varying the diameter of the flaw. Flaw depth is 0.2 m. Flaw diameter is: a) 0.05 m; b) 0.1 m; c) 0.2 m; and, d) 0.4 m.



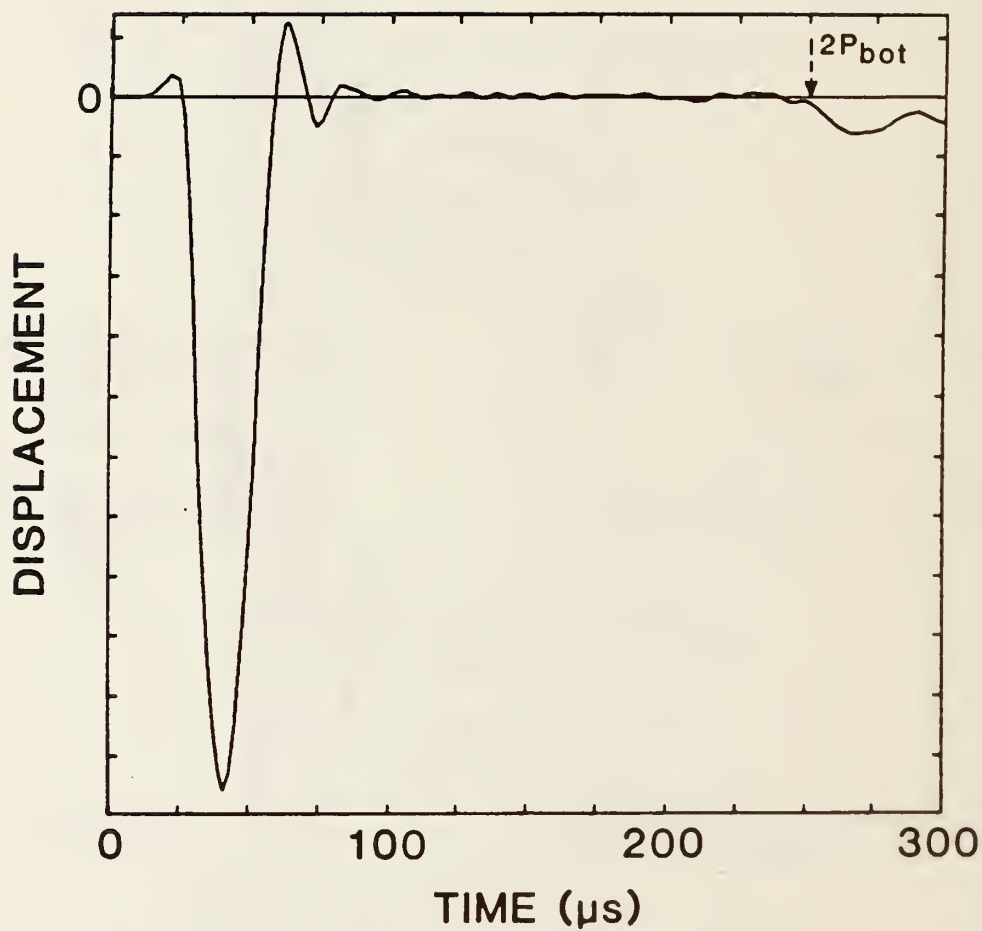


Figure 6.17 Surface displacement waveforms obtained from a plate containing a 0.1-m diameter flaw located 0.4 m below the top surface of the plate.

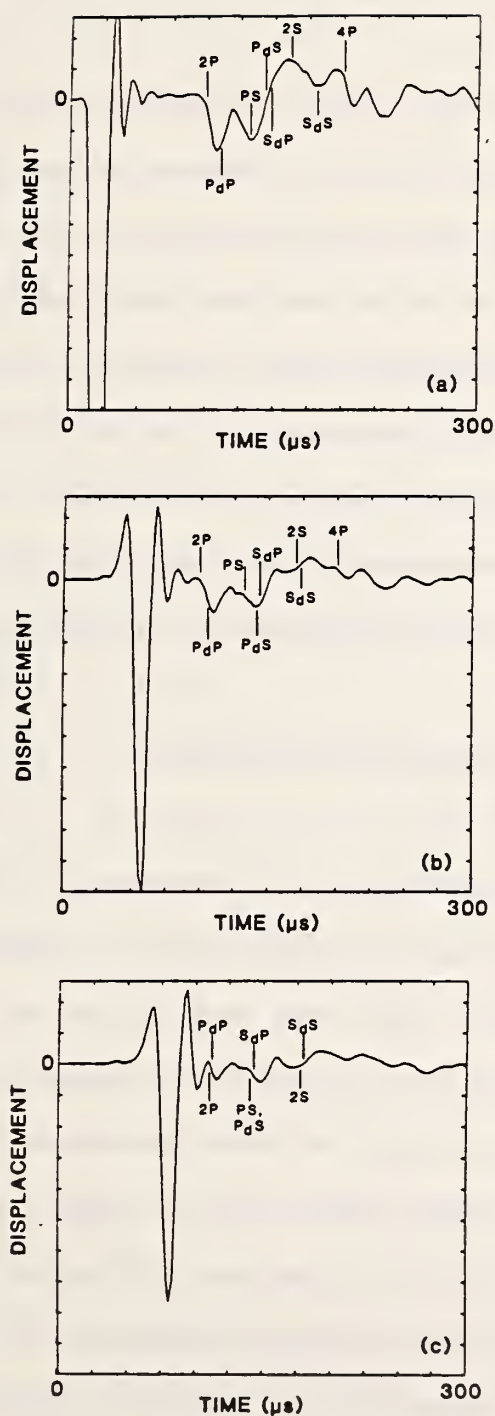


Figure 6.18 The effect on displacement waveforms of increasing the distance,  $H$ , between the impact point and the point where the surface displacement is measured: a)  $H = 0.025$  m; b)  $H = 0.1$  m; and, c)  $H = 0.15$  m.

## CHAPTER 7

### IMPLEMENTATION OF THE IMPACT-ECHO METHOD FOR FLAW DETECTION IN CONCRETE

#### 7.1 INTRODUCTION

The experimental phase of this work had two primary objectives: 1) to develop an impact-echo measurement technique (instrumentation and signal acquisition and processing) for finding flaws within plain and reinforced concrete; and 2) to confirm the observations and conclusions drawn from the analytical and finite element studies of solid plates and plates containing planar flaws.

This chapter describes the development of an impact-echo technique for concrete. Results obtained from controlled laboratory flaw studies in plain and reinforced concrete plates are presented.

#### 7.2 DEVELOPMENT OF A MEASUREMENT TECHNIQUE

##### 7.2.1 Impact Sources

Initially, small steel ball bearings, dropped from a height of 0.2 m, were used as the impact source. The contact times of 4- to 16-mm diameter, steel ball bearings on concrete ranged from approximately 20 to 90  $\mu$ s. The impact of these steel balls produced sufficient energy to penetrate 0.5-m thick concrete plate elements.

The contact time produced by the impact of steel balls on concrete was estimated by finding the difference between successive zeroes in the frequency spectrum (Section 5.3.1). Experimental contact times for a particular steel ball varied depending upon the condition of the concrete surface under the point of impact.

A hard, smooth surface produced contact times that were in almost exact agreement with Hertz elastic theory (Section 2.2.1). A rough textured surface tended to produce longer contact times than those predicted by elastic theory probably because local crushing of the paste phase of the concrete under the point of impact.

The contact time could also be estimated from the duration of the R-wave signal in the time domain waveform. Analytical and finite element studies showed that the time difference between the front and the back of the R-wave signal is approximately equal to the difference obtained from successive zeroes in the frequency domain; this time difference is therefore also an accurate estimate of the contact time of the impact.

Small diameter ball bearings are convenient to use in laboratory studies of horizontal concrete specimens. However, a more practical impact source would be needed for testing vertical surfaces and for field testing. Thus spring-loaded impactors (Equotip impactors, manufactured by Proceq SA, Zurich, Switzerland) designed for hardness testing of metals were adapted for use as impact sources. Two impactors were used: one had a 3-mm diameter, spherical steel tip attached to a 5.5-g spring-driven mass; the other had a 5-mm diameter tip attached to a 20 g mass. The contact times produced by the impactors ranged from approximately 40 to 80  $\mu$ s, depending on the condition of the concrete surface. Fig. 7.1 shows an impactor containing the spring-driven mass.

### 7.2.2 Transducer and Filter

The receiving transducer was a conical, broadband, displacement transducer which was recently developed at NBS for acoustic emission testing of metals [68]. This transducer, which is shown in Fig. 7.2, consists of a small conically shaped piezoelectric element cemented to a large brass backing. The output of the transducer is proportional to normal surface displacement. The brass backing damps out the ringing of the transducer element so that the recorded response is a faithful measurement of the surface displacement. Because of its small contact area the transducer closely approximates a point receiver.

As the transducer was developed for testing of metals, a thin sheet of metal foil had to be used between the conical element and the concrete surface to complete the transducer circuit. In the initial phase of the work, a sheet of aluminum foil was used. The foil was coupled to the concrete surface using water soluble gel. The transducer was designed for use of a polished metal surface; thus, grinding of the concrete surface was generally required to achieve proper coupling between the conical element and the surface when the aluminum foil was used. As grinding of the surface was tedious as well as impractical, the foil was replaced with a thin sheet of lead. Use of the lead, which is malleable and conforms to the concrete surface, eliminated the need for using the gel and for surface preparation, greatly simplifying the experimental procedure.

The transducer was protected from electromagnetic noise by



a metal shield. The shield was also used to house a unity gain amplifier. The transducer was used with a high pass filter which strongly attenuated frequencies less than 2 kHz. The filter was used to reduced the effects caused by a low frequency resonance of the transducer assembly (the large brass backing on the small conical element acting as a mass on a spring).

### 7.2.3 Oscilloscope

A digital storage oscilloscope operating at a 500 kHz sampling frequency (2  $\mu$ s sampling rate) was used to store and process received signals. Time domain signals contained 1024 sampling points; therefore, a 2  $\mu$ s sampling rate corresponds to a resolution of 0.488 kHz in the frequency domain (Section 5.2).

The oscilloscope was programmable which facilitated signal processing, and it was equipped with two disk drives so that data could be permanently stored. The oscilloscope was interfaced with a plotter so that waveforms, frequency spectra, etc., could also be plotted directly. Data could also be transferred to a personal computer for further analysis and/or plotting.

### 7.2.4 Concrete Specimens

Experimental displacement waveforms were obtained from large concrete plates, in which artificial flaws were embedded at known locations. Four plates were cast; these included:

- 1) a solid, 0.25-m thick plate, which was 1.125 x 1.125 m in plan.

- 2) a 0.2-m thick plate, 0.5 x 1 m in plan, which contained steel bars placed 0.06 m below the top surface of the plate. Plan and elevation views are shown in Fig. 7.3. Bar diameters ranged from 19.1 to 44.5 mm.
- 3) a 0.5-m thick plate, 2 x 4.5 m in plan, in which were embedded at various depths 25-mm thick disks cut from rigid, polyurethane foam insulation board. Disk diameters ranged from 0.05 to 0.5 m. Plan and elevation views of this plate are shown in Fig. 7.4. Fig. 7.5 shows the formwork for the plate with the flaws in place prior to casting of the concrete.
- 4) a 0.5-m thick plate, 2 x 2.25 m in plan, which contained a variety of artificial flaws, including: a thin metal duct partially filled with grout; 0.075-mm thick plastic sheets to simulate real cracks; and circular and rectangular flaws cut from the polyurethane foam board. A mat of steel reinforcing bars was placed over half the plate at a depth of approximately 5 cm below the top surface of the plate; bar diameters were 22.2 and 25.4 mm. Plan and elevation views of this plate are shown in Fig. 7.6. Fig. 7.7 shows the formwork for the plate with artificial flaws in place prior to casting of the concrete.

In plates Nos. 1 and 3, the coarse aggregate was crushed limestone with a nominal maximum size of 12 mm, and the average 28-day cylinder compressive strength was 25.9 MPa. In plate No. 2,

the coarse aggregate was rounded gravel with a maximum size of 12 mm; the 28-day cylinder compressive strength was 34 MPa. In plate No. 4, the coarse aggregate was crushed limestone with a maximum size of 19 mm; 28-day cylinder compressive strength was 28.4 MPa.

#### 7.2.5 Signal Acquisition and Processing

The test set-up is shown in Fig. 7.8. Data acquisition by the oscilloscope was triggered by the voltage produced by the transducer response to the arrival of the large amplitude R-wave. Once a waveform was acquired, it could be studied in the time domain or transformed into the frequency domain by use of the Fast Fourier Transform technique.

In time domain analysis, the exact time of the start of the impact (the beginning of the waveform) must be known so that the time of wave arrivals can be determined from the perturbations in the waveform. The time of the start of the impact was determined indirectly. Knowing the velocity of the R-wave in a concrete specimen and the distance between the impact point and the receiving transducer, the time required for the R-wave to travel from the impact point to the receiver can be calculated. (Recall from Section 2.1.2 that the R-wave speed is approximately equal to 0.56 times the P-wave speed.) As the arrival of the R-wave was easily identified in waveforms, the time of the impact can be determined.

The initial studies of displacement waveforms were carried out in the time domain. Later it was found that interpretation of displacement waveforms was simpler in the frequency domain.

In the following sections, both the displacement waveforms and frequency spectra are shown; however, most of the numerical results are based on frequency spectrum analyses.

#### 7.2.6 Determining Wave Speeds Through Concrete

To determine the location of a reflecting interface from the dominant peak in the frequency spectrum, the P-wave velocity in the test object must be known. Two methods were used for determining P-wave velocity in concrete: 1) the through transmission, pulse-velocity method (ASTM C 597 [4]); and 2) the impact-echo method. As discussed in Chapter 3, in the pulse-velocity method, the transmitter and the receiver are located on opposite sides of the test object and the time for an ultrasonic P-wave pulse to travel from transmitter to receiver through the test object is measured. The ultrasonic pulse-velocity is obtained by dividing the distance between the transducers by the travel time. The commercial test apparatus uses lightly damped transducers; therefore the pulse that is generated contains multiple cycles of P-waves. The transit time is based on detecting the arrival of the leading edge of the pulse. In the impact-echo method, the transient response of a test object of known thickness subjected to surface impact is recorded. Then the peak frequency in the amplitude spectrum obtained from transforming the time domain waveform is used to calculate the wave velocity using Eq. (5.7). Thus the P-wave velocity is calculated indirectly.

Previously, it was thought that the pulse-velocity method



could be used to independently measure P-wave velocities in concrete. However, a discrepancy was found when pulse velocities determined from ultrasonic pulse-velocity measurements (obtained using 54 kHz transducers, 5 cm in diameter) were used in frequency spectrum analyses. When the ultrasonic pulse velocity was used to calculate the depths of reflecting interfaces using the peak frequency in the amplitude spectra, the calculated depths exceeded the actual depths in all test situations. When direct comparisons were made between ultrasonic pulse velocities measured through the thickness of solid concrete plates and the velocity calculated from peak frequencies obtained from impact-echo tests on the same slabs, it was found that the P-wave velocities calculated by the impact-echo method were approximately 10 percent slower than the velocities determined by the pulse velocity method.

A time domain study of waveforms obtained from interfaces of known depth showed that the onset of the downward displacements in the waveforms agreed with wave arrival times computed using the P-wave velocity obtained from the impact-echo method. Results of tests on the 0.25-m thick concrete plate illustrate the difference between the two velocities. Pulse-velocity measurements, taken at the center of the plate, indicated a wave speed of 4020 m/s. Fig. 7.9 shows the waveform obtained from an impact-echo test (H/T value of 0.2) carried out at the same point. The peak in the corresponding frequency spectrum was 7.32 kHz, which gives a computed P-wave velocity of 3660 m/s. For a velocity of 3660 m/s, the arrival times of the first (2P), second (4P), and third (6P) P-waves are



137, 274, and 410  $\mu\text{s}$ , respectively, and for a velocity of 4020 m/s, the arrival times are 124, 249, and 374  $\mu\text{s}$ . Arrows indicating the arrival of P-waves corresponding to these velocities are superimposed on the waveform. Notice that the arrival times corresponding to the velocity of 3660 m/s have better overall agreement with the beginning of the sudden downward displacements that characterize P-wave arrivals.

Similar results indicating a difference between P-wave velocities obtained using pulse-velocity and resonance measurements were obtained by others [66] when dynamic modulus of elasticity values obtained from through-transmission, pulse-velocity tests were compared to values obtained by resonant frequency testing (ASTM C 215 [4]). It was found that the elastic modulus values based on resonance measurements were 8 to 23 percent less than those based on pulse-velocity measurements. Since P-wave velocity is proportional to the square root of the elastic modulus, this difference in modulus values corresponds to a 4 to 12 percent difference in P-wave velocities obtained using the two methods. To the author's knowledge there is no verifiable explanation for this difference.

Thus, for accurate determination of flaw depth, the P-wave velocity must be determined from an impact-echo test on a part of the structure being evaluated where the thickness is known. This velocity can then be used to accurately determine the depth of internal interfaces in other parts of the structure based on the peak frequencies obtained from impact-echo tests.

### 7.3 WAVEFORMS AND FREQUENCY SPECTRA OBTAINED FROM A SOLID PLATE

The impact-receiver configuration for tests carried out on the solid plate (Plate No. 1) is shown in Fig. 4.3(b). For the results presented in this section, the thickness of the plate ( $T$ ) is equal to 0.25 m; thus, the only two variables in this test configuration are the contact time of the impact ( $t_c$ ) and the distance between the impact point and the receiving transducer ( $H$ ). The effect on experimental waveforms and frequency spectra caused by varying these two parameters are shown in the following sections. Experimental observations are compared to observations drawn from the studies of theoretical waveforms and spectra (Chapter 5).

The P-wave speed in the plate was 3660 m/s. Note that in the experimental waveforms shown in this chapter, R-wave signals are clipped so that displacement patterns produced by internal reflections are accentuated and interpretation of frequency spectra is simplified (see Section 5.4.3). The frequency spectra shown in this chapter are arbitrarily limited to a range of 0 to 50 kHz; this was done to clearly show peak frequencies which, for the specimens tested, are in the range of 0 to 25 kHz.

#### 7.3.1 Effect of Contact Time of the Impact

In Section 5.3.2.1, it was shown that as the contact time of the impact increases, the perturbations in theoretical displacement waveforms, computed using Green's function solutions, become smoothed out. For impacts having contact times approaching the arrival time of the 2P-wave reflected from the bottom of the

plate, wave arrival times do not agree with the beginning of the downward displacements in the waveform. However, it was shown that in the frequency domain, a short contact time is not essential. In fact, an impact having a longer contact times produces a higher amplitude peak in the frequency spectrum at a value corresponding to the frequency of P-wave arrivals from the bottom surface of the plate, because more energy is confined in the frequency which has a wavelength corresponding twice the thickness of the plate ( $2T = \lambda$ , see Section 3.2.3). These observations were based on studies of theoretical displacement waveforms and their frequency spectra. To verify these observations, experimental results are presented.

Fig. 7.10 shows a series of displacement waveforms and the corresponding frequency spectra obtained for various contact times. Contact time was varied by using spheres 6.35, 8, and 16 mm in diameter (contact times of 34, 48, and 90  $\mu\text{s}$ ). The distance between the impact point and the receiver was 0.05 m (H/T value of 0.2). The 2P-wave arrival time was 137  $\mu\text{s}$ ; thus, the contact times correspond to  $t_c/t_{2P}$  values of 0.25, 0.35, and 0.66, respectively. Calculated wave arrival times are indicated on the waveforms.

For the P-wave speed of 3660 m/s, the 0.25-m thickness of the plate corresponds to a resonant frequency of 7.06 kHz. For the 2  $\mu\text{s}$  sampling rate used in capturing experimental waveforms, the possible values in the frequency spectrum occur at 6.84 and 7.32 kHz. The value of 7.06 kHz falls almost exactly between these two possible values. Therefore, the peak in spectra obtained for a thickness of 0.25 m, can occur at either 6.84 or 7.32 kHz.

There is a noticeable difference in the experimental waveforms obtained from the concrete plate as compared to the theoretical waveforms computed using Green's function solutions (Chapter 5). In the theoretical solutions, except for the initial upward displacements caused by the surface waves, the surface of a solid plate is never displaced above its undisturbed position (e.g., see Figs. 5.5 and 5.6). However, in experimental waveforms, the large amplitude R-wave appears to cause an overshoot response of the transducer, which occurs just after the R-wave passes by the transducer. This overshoot causes the displacement pattern produced by internal reflections to be shifted upward.

As the contact time of the impact increases (Figs. 7.10(a)-(c)), the displacement response becomes smoother. For the longest contact time (Fig. 7.10(c);  $t_c/t_{2p}$  value of 0.66) the calculated wave arrivals times no longer agree with the start of the downward dips in the waveform; however, the 6.84 kHz peak in the frequency spectrum can still be used to determine the thickness of the plate regardless of the contact time. This is because the periodicity of the major perturbations in the waveform is determined by the thickness of the plate. As expected, the amplitude of the peak in the frequency spectrum increases as the contact time increases. These experimental observations verify those drawn from the theoretical study.

### 7.3.2 Test Configuration

In Section 5.3.2.2, it was shown that interpretation of



waveforms and frequency spectra is simpler for test configurations where the distance between the impact point and the receiver is small relative to the thickness of the plate (small  $H/T$  value). This was because a small  $H/T$  value minimizes the complications caused by large amplitude R-wave signals and those caused by S-wave reflections.  $H/T$  values less than approximately 0.5 were shown to give interpretable results. These theoretical observations are compared to experimental results in the following discussion.

Figs. 7.11(a)-(d) show a series of displacement waveforms and their corresponding frequency spectra for distances of 0.025, 0.05, 0.125, and 0.25 m between the impact point and the receiving transducer. These distances correspond to  $H/T$  values of 0.1, 0.2, 0.5, and 1, respectively. An 8-mm diameter sphere (contact time approximately 50  $\mu$ s) was used for all the test configurations. Note that 0.025 m is the smallest practical spacing between the impact point and the receiver because of the 0.02 m radius of the transducer backing.

Waveforms and frequency spectra obtained for  $H/T$  values of 0.1 (Fig. 7.11(a)) and 0.2 (Fig. 7.11(b)) are similar. However, as the  $H/T$  value increases from 0.2 to 0.5 (Fig. 7.11(b) and (c)), both the displacement waveforms and the frequency spectra become more complicated. For an  $H/T$  value of 1 (Fig. 7.11(d)), the peak frequency in the spectrum is not as pronounced and its value shifts from 7.32 to 7.81 kHz; a depth determination based on this higher value would be incorrect. As discussed in Section 5.3.2.2, this trend is observed because the amplitude of P-wave reflections



decreases relative to the amplitude of S-wave reflections. Therefore, S-wave arrivals have a significant influence on the displacement response, complicating both the waveform and the frequency spectrum. In addition, as observed in the theoretical frequency spectra in Fig. 5.6, the amplitude of the peak in the frequency spectrum decreases as  $H$  increases, because the amplitude of the displacements caused by the arrival of P-waves decreases as the receiver gets farther from the impact point.

In summary, experimental results obtained from solid plates are in agreement with observations drawn from Green's function solutions for an infinite plate.

#### 7.4 PLANAR DISK-SHAPED FLAWS IN A PLATE

Studies of planar disk-shaped flaws in a 0.5-m thick plate (plate 3) were carried out. The diameters and locations of these flaws were shown in Fig. 7.4. The impact-receiver configuration for tests carried out over the flaws is shown in Fig. 7.12. The distance between the impact point and the receiver was 0.05 m.

The P-wave speed in the concrete was 3530 m/s. This speed was an average speed which was determined from impact-echo tests carried out over interfaces located 0.13, 0.25, 0.38, and 0.5 m below the top surface of the plate. Fig. 7.13 shows the known depths plotted versus the inverse of twice the peak frequencies in the corresponding spectra. A linear regression analysis was carried out to determine the best fit line through these points. The slope of this line is the P-wave speed (Eq. 5.8).

To determine the reliability and the sensitivity of the impact-echo technique for locating planar flaws in concrete, the effects on surface displacement waveforms and their corresponding frequency spectra of the following test variables were studied: 1) contact time of the impact; 2) flaw diameter; and, 3) flaw depth.

To establish the baseline response of the solid 0.5-m thick plate for comparison with responses obtained from portions of the plate containing internal flaws, Fig. 7.14 shows a waveform and the corresponding frequency spectrum obtained over a solid portion of the plate for impact produced by a 12.7-mm diameter sphere (contact time approximately 60  $\mu$ s). The peak amplitude in the frequency spectrum which corresponds to the frequency of P-wave reflections from the bottom surface of the plate occurs at a value of 3.42 kHz.

#### 7.4.1 Effect of Test Variables on Impact-Echo Waveforms

In Section 6.5, the finite element method was used to study the effects on impact-echo waveforms caused by changing the contact time of the impact, the diameter and the depth of a flaw, and the spacing between the impact point and the point where the displacement was monitored. These studies showed that for a given impact, the diameter to depth ratio of a flaw ( $D/T$ ) is a useful parameter for determining whether or not a flaw will be detected. For flaws at a given depth, the critical value of flaw diameter increases as the contact time of the impact increases. If the diameter of a flaw was sufficiently large, it was found that the depth of a flaw

could be determined accurately from time domain analysis of displacement waveforms if the contact time of the impact was less than or equal to two-thirds of the arrival time of the 2P-wave reflected from the surface of the flaw.

In the following sections, the observations drawn from the finite element analyses are verified by observations drawn from experimental results. In addition, interpretation of experimentally obtained waveforms by frequency spectrum analysis is emphasized.

#### 7.4.1.1 Contact Time of the Impact

Fig. 7.15 shows a series of displacement waveforms and the corresponding frequency spectra which were recorded over a 0.2-m diameter flaw located 0.127 m below the top surface of the concrete plate. The H/T value for this test configuration was 0.38. The contact times of the impacts in Figs. 7.15(a)-(c) were varied by dropping 4-, 8-, and 16-mm diameter spheres (contact times of 26, 40, and 80  $\mu$ s). The arrival time of the 2P-wave reflected from the flaw was 74  $\mu$ s, which resulted in  $t_c/t_{2p}$  values of 0.35, 0.54, and 1.08.

In the spectrum obtained for the shortest contact time (Fig. 7.15(a)), the peak amplitude at 14.2 kHz gives a calculated flaw depth of 0.124 m (Eq. (5.8)). Notice that in Fig. 7.15(a) there is also a lower amplitude peak at 3.42 kHz which is the frequency of P-wave reflections from the bottom surface of the plate (see Fig. 7.14). Recall from the displacement and stress fields obtained from the finite element analyses (Section 6.4.2.2) that waves

diffract around the edges of a small flaw, reform below the flaw, and are subsequently reflected by the bottom surface of the plate. Thus, the frequency spectrum would be expected to contain a high amplitude peak at a frequency value corresponding to the frequency of wave reflections from the bottom surface of the plate.

As observed in the finite element study, the smoothing effect on waveforms produced by increasing the contact time is evident in the waveforms shown in Fig. 7.15(b) and (c). In the waveforms shown in Figs. 7.15(a) and (b), P-wave arrivals from the surface of the flaw dominate the displacement pattern.

Notice that in the frequency spectra shown in Fig. 7.15, the amplitude of the 14.2 kHz peak decreases, and the amplitude of the 3.42 kHz peak increases as the contact time increases, until in Fig. 7.13(c) there is only a very low amplitude remnant of a peak at 14.2 kHz. For the 0.2-m diameter flaw to be detected using the "one-wavelength" criterion (Section 6.5.1), the stress waves produced by impact must contain frequencies of 18 kHz or higher (wavelengths of 0.2 m or less). For the 20, 40, and 80  $\mu$ s duration impacts, the first zero in the frequency spectrum of the input pulse occurs at 58, 38, and 19 kHz, respectively (see Fig. 5.2(b)). Thus, the pulse produced by the 80  $\mu$ s duration impact contains very little energy in the frequency range of 18 kHz and higher; therefore, there is no large amplitude peak at 14.2 kHz - the frequency of P-wave reflections from the surface of the flaw.

An accurate determination of the depth of the flaw can be made using the frequency spectra shown in Figs. 7.15(a) and (b).



The flaw would not be detected using the spectrum shown in Fig. 7.15(c). However, the effects on the waveform in Fig. 7.15(c) caused by diffraction indicate that a flaw or some other irregularity is present. As shown in waveforms obtained from finite element analyses, diffraction effects make the waveform appear very different from a waveform obtained from a solid plate subjected to an impact having approximately the same contact time. In the waveform in Fig. 7.15(c), there are higher frequency oscillations superimposed upon the lower frequency oscillations caused by P-wave reflections from the bottom surface of the plate. In this waveform, the effects produced by reflections from the bottom surface of the plate and the effects caused by the presence of the flaw are both clearly evident.

#### 7.4.1.2 Flaw Diameter

Figs. 7.16(a)-(c) show waveforms and their corresponding frequency spectra obtained over 0.1, 0.2, and 0.5-m diameter flaws located 0.25 m below the top surface of the plate. These flaw geometries resulted in D/T values of 0.4, 0.8, and 2, respectively. Impacts were produced by a 8-mm diameter sphere (contact times of approximately 40  $\mu$ s). The arrival time of the 2P-wave reflection from the surface of the flaw was 142  $\mu$ s, for a  $t_c/t_{2P}$  value of 0.28.

The waveform and the frequency spectrum obtained from the solid 0.25-m thick plate subjected to approximately the same duration impact ( $t_c/t_{2P}$  value of 0.25) was shown in Fig. 7.10(b). (The P-wave speed in this plate was not significantly different than the P-wave



speed measured in the 0.5-m thick plate which contained the flaws. Both plates were made from the same batch of concrete.) This waveform and spectrum represent the baseline response of a plate of the same thickness as the depth of the flaws in this study; that is, it is the response caused by specularly reflected and mode-converted waves.

The waveform and spectrum obtained from the 0.5-m diameter flaw (Fig. 7.16(c)) are very similar to those obtained from the solid plate (Fig. 7.10(b)) because the diameter of the planar flaw is large relative to the depth of the flaw ( $D/T$  equal to 2). Notice that the displacement waveform in Fig. 7.16(c) exhibits a series of low amplitude oscillations that are not present in Fig. 7.10(b). These oscillations are due to the effects caused by waves diffracted from the edges of the disk-shaped flaw. In the frequency spectrum these oscillations produce several lower amplitude peaks in the range of 20 to 25 kHz that were not present in the frequency spectrum obtained from the solid plate (Fig. 7.10(b)).

In the spectrum obtained from the 0.2-m diameter flaw (Fig. 7.16(b)) there is a single dominant peak in the spectrum at a frequency which corresponds to the depth of the flaw. However, the amplitude of this peak is significantly less than the amplitude of the peak obtained from the 0.5-m diameter flaw, which in turn is less than the amplitude of the peak in the spectrum obtained from a solid plate. This indicates that the specular reflections produced by smaller flaws are lower in amplitude from those produced by larger flaws or the bottom surface of a plate of the same

thickness as the depth of the flaw. The decrease in the amplitude of specular reflections is directly related to the amount of energy contained in the frequencies having wavelengths equal to or less than the diameter of the flaw (one-wavelength criterion). As flaw diameter decreases, less energy is reflected.

An accurate determination of the depth of both the 0.2 and 0.5-m diameter flaws ( $D/T$  values of 0.8 and 2) can be made from the spectra in Figs. 7.16(b) and (c). This is not the case for the 0.1-m diameter flaw ( $D/T$  value of 0.4).

The amplitude of the peak in the frequency spectrum produced by specular reflection from the surface of the 0.1-m diameter flaw (Fig. 7.16(a)) is much less than that obtained from the 0.2-m diameter flaw. Therefore, the other frequencies, which are also present in the spectra obtained from the 0.2- and 0.5-m diameter flaws, appear much larger relative to the 7.32 kHz peak. For example, in Fig. 7.16(a), a peak at 9.76 kHz has become larger than the peak corresponding to the depth of the flaw. Using this spectrum, the presence of the flaw would be detected, but an accurate determination of the depth of the flaw could not be made.

Just as in the waveforms obtained from finite element analyses, it is observed that as the flaw diameter decreases, the amplitude of specular reflections from the flaw decreases and the displacements caused by diffracted waves have a more significant effect on the waveform. Therefore, effects produced by diffracted waves in displacement waveforms can be used to gain information about the relative sizes of flaws.

### 7.4.1.3 Flaw Depth

A series of waveforms obtained over flaws located at different depths, and the corresponding frequency spectra, are shown in Fig. 7.17. Fig. 7.17(a) was obtained over a 0.2-m diameter flaw located 0.127 m below the top surface of the plate (D/T value of 1.6). Figs. 7.17(b) and (c) were obtained over 0.5-m diameter flaws located 0.25 and 0.38 m below the top surface of the plate (D/T values of 1.9 and 1.3, respectively). Fig. 7.17(d) was obtained from a solid section of the 0.5-m thick plate. The contact time of the impact was approximately 40  $\mu$ s for the 0.127- and 0.25-m deep flaws, and 60  $\mu$ s for the 0.38-m deep flaw and the 0.5-m thick plate. A longer duration impact was used in the tests carried out over the deeper flaw so that the input pulse had greater penetrating ability. These contact times corresponded to  $t_c/t_{2p}$  values of 0.5, 0.3, 0.3, and 0.2, respectively.

As expected, the peak in the frequency spectra in Figs. 7.17(a)-(d) shifts to a lower frequency value as the depth of the reflecting interface increases. Using Eq. (5.8), the frequency values of 14.2, 7.08, 4.39, and 3.42 kHz correspond to depths of 0.124, 0.25, 0.40, and 0.52 m, respectively. These calculated values are very close to the depths that were measured prior to casting the concrete. As depth increases, the 0.488 kHz resolution in the frequency spectrum (2  $\mu$ s sampling rate) results in calculated depths that are not as precise. For example, at a depth of 0.127 m, adjacent points in the frequency spectrum correspond to a 0.004 m difference in depth; at a depth of 0.5 m, adjacent points in the

frequency spectrum correspond to a 0.048 m difference in depth. Thus, the peak frequency values obtained from the spectra in Fig. 7.17 are the closest frequencies to the values that correspond to the measured depths of the flaws. When probing thicker elements, more precise depth measurements can be made by using a slower sampling rate in the time domain (see Section 5.2).

For the 0.2-m diameter flaw located close to the surface (Fig. 7.17(a)) two peaks are present at frequencies corresponding to P-wave reflections from the surface of the flaw (14.2 kHz) and from the bottom of the plate (3.42 kHz). Compare this spectrum to that shown in Fig. 7.17(d); the 0.5-m thick plate produces a single peak at the 3.42 kHz frequency value.

#### 7.4.2 Sensitivity of the Impact-Echo Method for Detecting Planar Flaws

In the previous section, the effects of various test parameters on impact-echo waveforms have been shown. In this section, the results of a frequency domain study of waveforms obtained over all the various planar flaws in the concrete plate will be summarized and the sensitivity of the impact-echo method for detecting planar flaws will be discussed.

The sensitivity study involved determining the depths of flaws from the peak amplitude in frequency spectra. Flaw diameters ranged from 0.05 to 0.5 m and were located 0.127 to 0.38 m below the surface of the plate (see Fig. 7.4). The contact times of the impacts ranged from 20 to 90  $\mu$ s. The spacing between the impact point and the receiving transducer was 0.05 m in every test.



Three criteria were established for categorizing the results of each impact-echo test. These criteria were as follows:

- 1) If a flaw could be detected and its depth accurately determined, then the test result was labeled with a "YES";
- 2) If a flaw could be detected, but an accurate determination of its depth could not be made, then the test results was labeled with a "?"; and,
- 3) If a flaw could not be detected from a frequency domain analysis, then the test result was labeled with a "NO".

The results of all tests performed are shown in Fig. 7.18. Each test is plotted in terms of the  $t_c/t_{2p}$  value of the impact and the D/T value corresponding to the flaw geometry and the type of symbol identifying the results of each test<sup>1</sup>. The results fall into three distinct regions.

- 1) If the D/T value is greater than approximately 0.6 and the  $t_c/t_{2p}$  value is approximately less than 0.75, then all the results fell into the "YES" category - the flaw could be detected and its depth accurately determined. Examples of results which fall into this category are the frequency spectra shown in Figs. 7.17(a)-(d).

- 2) If, however, the D/T value becomes less than 0.6, then the results fell into the category labeled with a "?", in which a flaw could still be detected, but an accurate determination of

---

<sup>1</sup>A square corresponds to a YES; a diamond corresponds to a '?' and, an X corresponds to a NO.



its depth could not be made. Fig. 7.16(a) is an example of a frequency spectrum that falls into this category.

3) If the  $t_c/t_{2p}$  value becomes greater than approximately 0.75 for any value of  $D/T$ , then the results fell into the "NO" category - the flaw could not be detected from a frequency domain analysis. Fig. 7.15(c) is an example of a spectrum that falls into this category.

These results are valid for the range of  $D/T$  values considered in these tests ( $D/T$  values less than or equal to 2).

In concluding this discussion, it should be mentioned that the depth of a flaw or the bottom surface of a plate can be accurately determined from the peak in the frequency spectrum even for tests carried out near the edges of the plate. In the time domain, displacements due to reflections of P-, S-, and R-waves from the edges of a plate are superimposed upon the displacements due to reflections from internal flaws or the bottom surface of the plate, making a surface displacement waveform difficult to interpret. However, the frequency domain analysis is a simple technique for separating effects that are superimposed in the time domain. Generally, in a frequency spectrum obtained from a waveform that contains multiple R-wave reflections, the multiple reflections from an internal flaw or from the bottom surface of the plate will produce a peak at the frequency corresponding to the depth of the reflecting interface that is distinct from the frequencies corresponding to multiple R-wave reflections.

## 7.5 FLAWS IN REINFORCED CONCRETE

The results presented in the previous sections have demonstrated that the impact-echo technique can be used successfully to locate flaws within plain concrete. However, before the test technique could be considered as a possible field-worthy technique, it also had to be demonstrated that the technique can be used to detect flaws within reinforced concrete. Tests were carried out on a 0.2-m thick plate containing solid steel bars of various diameters (Fig. 7.3), and the effects caused by the bars on waveforms and frequency spectra were determined. Subsequently, a 0.5-m thick, reinforced concrete plate was cast in which were embedded a variety of artificial flaws (Figs. 7.6 and 7.7). Results obtained from impact-echo tests on this plate were used to determine whether flaws could be detected under layers of reinforcing steel.

Before presenting experimental results, the wave reflection from a concrete/steel interface is discussed.

### 7.5.1 Wave Reflection from a Concrete/Steel Interface

As discussed in Section 2.1.3, both reflection and refraction occur at an interface between two solids. The portions of the incident energy that are reflected and refracted depend upon the angle of the incident wave and the acoustic impedance of the two solids. Previously, reflection from concrete/air interfaces (stress free boundaries) has been discussed; for normal incidence, almost total reflection occurred because the acoustic impedance of air was negligible compared to that of concrete. However, the acoustic

impedance of steel is higher than that of concrete; therefore, the type of wave reflection that occurs from a concrete/steel interface is different from the type of reflection that occurs from a concrete/air interface. This difference is explained qualitatively in Fig. 7.19. Fig. 7.19(a) shows an infinite concrete plate bounded by air; Fig. 7.19(b) shows an infinite concrete plate bounded on the bottom by steel and on the top by air.

First consider the case where impact occurs on a plate with stress free boundaries (Fig. 7.19(a)). The P-wave generated by the impact is a compression wave. When this wave is incident upon the bottom surface of the plate, it is reflected as a tension wave. This tension wave propagates back up through the plate to be reflected at the top surface as a compression wave, and the cycle begins again. Every P-wave arriving at the top of the plate is a tension wave which causes a downward displacement of the surface. The period between successive downward dips in the waveform is the time between successive P-wave arrivals, that is, the time for a P-wave to travel twice the thickness of the plate. Thus, if a frequency spectrum were computed, the value of the peak in the frequency spectrum would correspond to twice the plate thickness (Eq. (5.8)).

Next, consider impact on the top surface of a concrete plate which is in contact with a thick layer of steel at its bottom surface (Fig. 7.19(b)). When the initial compression wave generated by the impact is incident upon the concrete/steel interface it does not change sign; that is, it is reflected as a compression wave.

When this compression wave reaches the top surface of the plate it causes an upward displacement of the surface. However, since the top surface of the plate is a stress free boundary, the incident compression wave is reflected as a tension wave. This wave propagates down through the plate and is reflected at the concrete/steel interface unchanged. When this tension wave reaches the top surface of the plate it causes a downward displacement of the surface. The incident tension wave is reflected as a compression wave and the cycle begins again. Therefore, in the surface displacement waveform (Fig. 7.19(b)), the periodicity of displacements (time between successive upward or downward displacements) is twice as long as in waveform obtained from the plate with free boundaries (Fig. 7.19(a)). This explanation was verified by a finite element analysis of a layered (concrete/steel) plate.

The period in the waveform shown in Fig. 7.19(b) is equal to the time it takes for a wave to travel four thicknesses of the plate. Therefore, the value of the peak in the frequency spectrum obtained by transforming this waveform would correspond to four plate thicknesses; the peak frequency value will be half that obtained from the waveform shown in Fig. 7.19(a).

Based on this qualitative analysis, the peak amplitude produced by reflections from steel bars would be expected to occur at a frequency value that is approximately one-half the value that would be obtained from a concrete/air interface. Therefore, to determine the depth of a concrete/steel interface from the peak



in the frequency spectrum, Eq. (5.8) (derived for a plate with stress free boundaries) can be modified:

$$T = \frac{1}{2} \frac{[C_p]}{2F} \quad (7.1)$$

#### 7.5.1.1 Interaction of Waves with a Steel Bar Embedded in Concrete Plate

The amplitudes of the measured surface displacements caused by waves reflected from the surface of a steel bar embedded in a concrete plate are much less than the amplitudes of waves reflected from the surface of a planar flaw (concrete/air interface) for the following reasons: (a) a cylindrical inclusion reflects less energy than a planar interface with lateral dimensions equivalent to the diameter of the cylindrical inclusion [48]; and, (b) for normal incidence upon a concrete/steel interface, approximately 45 percent of the incident energy is reflected, as compared to approximately 100 percent reflection that occurs at a concrete/air interface. (Reflection and refraction coefficients for a plane wave incident upon a planar concrete/steel interface were calculated using the equations given in Ref. [48].) The remainder of the incident energy is refracted into the bar.

The portion of the wave that is refracted into the bar undergoes additional reflection and refraction at the steel/concrete interface. Thus, multiple reflections occur within the bar, and additional reflected and refracted waves are produced each time a wave is incident upon a steel/concrete or concrete/steel boundary. When waves that are propagating within the plate are incident upon



a cylindrical inclusion, the waves will also bend around the inclusion; this phenomenon is similar to the process that occurred for a wave incident upon a planar flaw. Thus, the displacement and stress fields produced by transient waves incident upon a steel bar embedded in a concrete plate are more complicated than those produced by the interaction of transient waves with a planar disk-shaped flaw (concrete/air interface).

To show the effect of steel bars on waveforms and frequency spectra, selected results obtained from a 0.2-m thick plate in which were embedded various diameter steel bars (Fig. 7.3) are discussed in the following section.

#### 7.5.2 Waveforms and Frequency Spectra Obtained from a Concrete Plate Containing Steel Bars

Impact-echo tests were carried out over 25.4-, 38.1-, and 44.5-mm diameter bars. Fig. 7.20 shows waveforms and frequency spectra generated by impacts having contact times of approximately 20  $\mu$ s, and Fig. 7.21 shows waveforms and spectra generated by impact having contact times of approximately 54  $\mu$ s. The distance from the top surface of the plate to the top of the bars was 0.06 m. The arrival time of the 2P-wave reflected from the top of the bar was 29  $\mu$ s.

The distance between the impact point and the receiving transducer was 0.05 m. Both the impact point and the receiver were located over the centerline of the bar. The peak frequency obtained from an impact-echo test over a solid portion of the 0.2-m thick plate was 10.25 KHz, which results in a computed P-wave speed of

4100 m/s. Using Eq. (7.1), the frequency corresponding to P-wave reflections from the top of the bars would be expected to be about 17 KHz.

In the waveforms shown in Fig. 7.20, the effect of the bars appears as higher frequency oscillations superimposed on the lower frequency oscillations caused by waves reflected from the bottom surface of the plate. In the frequency spectra, it is seen that the reflections from the bars give rise to multiple peaks. These frequency peaks occur at values ranging from 17 to 23 kHz. Reflections from the bottom of the plate produce a frequency peak at a value slightly less than the 10.25 kHz obtained from a solid part of the plate. In Fig. 7.20(c) (4.45-cm bar), there are a group of lower frequency peaks. These peaks could be produced by the interaction of P-and S-waves with a larger diameter bar. For small diameter bars, P-wave reflections dominate the waveform. For a larger diameter bar, the S-waves that are incident upon the bar are larger in amplitude (see Fig. 4.2); therefore, diffracted and reflected S-waves have a more significant effect on the displacement waveform and thus the frequency spectrum.

Notice that in Fig. 7.20, the amplitudes of the peak (or peaks) corresponding to the frequency of waves reflected from the bottom surface of the plate decreases and the amplitudes of the peaks corresponding to the frequency of waves reflected by the bar increases with increasing bar diameter. The group of peaks produced by the bar changes from being a secondary effect in Fig. 7.20(a), to being the dominant effect in Fig. 7.20(c), because the portion

of the incident energy that is reflected by the bar increases as the bar diameter increases. A plot of the amplitude versus the wavelength of each component wavelength in the pulse produced by a 20  $\mu$ s duration impact is shown in Fig. 7.22(a). It is seen that the pulse contains sufficient energy in the range of frequencies having wavelengths that are approximately equal to or smaller than the diameter of all three bars.

Notice that in Fig. 7.21, the displacement waveforms are characterized by the broad, large amplitude oscillations which are produced by a longer duration impact. Waves produced by 54- $\mu$ s duration impacts contain a much narrower range of frequencies. As shown in Fig. 7.22(b), there is little energy in the range of frequencies having wavelengths that are approximately equal to or smaller than the diameters of the bars. Therefore in the frequency spectrum shown in Fig. 7.21, the amplitudes of the frequencies associated with reflections from the bars are very small.

In Fig. 7.21(c), the effects produced by the bar are more apparent because of the multiple peaks that appear which correspond to frequencies of waves reflected from the bottom of the plate. If the bar were not present there would only be a single peak. This phenomenon may be useful as an indication of bar size.

These results show that by increasing the contact time of the impact, the effects produced by bars on waveforms and frequency spectra can be significantly reduced. This is important because the primary purpose of impact-echo testing will be to detect flaws located beneath reinforcing bars, not to locate the bars themselves.

Conversely, if one wishes to interrogate for the existence of bars, then short duration impacts must be used. Note that using longer contact times to reduce the effects caused by bars, limits the size of the flaws that can be detected within reinforced concrete; flaws on the order of the size of the bars will not be detected. However, flaws of this size are usually not a concern in concrete structures.

In the following section waveforms and the corresponding frequency spectra generated by impacts on a reinforced concrete plate containing planar disk-shaped flaws are presented. Longer duration impacts are used to reduce the effects caused by the steel reinforcing bars on measured signals.

### 7.5.3 Planar Disk-Shaped Flaws in Reinforced Concrete

Results discussed in this section were obtained from the 0.5-m thick concrete plate shown in Figs. 7.6 and 7.7. Steel reinforcing bars were placed over one-half of the plate, parallel to both sides of the plate, and spaced 20 cm on center. Bars, 22.2 mm in diameter, were placed 73 mm below the top surface of the plate; on top of these bars was placed a layer of 25.4-mm diameter bars. The depth of the 25.4 mm bars was 48 mm.

The P-wave speed was obtained from an impact-echo test over the 0.5-m thickness of the plate, using a sampling rate of 5  $\mu$ s. The peak frequency was 4.10 kHz and the computed P-wave speed was 4100 m/s (Eq. 5.8). To establish the baseline response of the plate, Fig. 7.23 shows a waveform and frequency spectrum obtained over a solid portion of the 0.5-m thick plate. The sampling rate in



this case was 2  $\mu$ s, as will be the case for all of the other results that will be presented in this and the following section. For a 2  $\mu$ s sampling rate, the peak amplitude occurs at a frequency of 3.91 kHz.

Figs. 7.24 and 7.25 show waveforms and frequency spectra obtained over a 0.35-m diameter flaw which was located 0.26 m below the top surface of the plate (H/T value of 0.19). The 5.5 g impactor was used as the impact source (contact times approximately 70  $\mu$ s). The arrival time of the 2P-wave reflected from the surface of the flaw was 125  $\mu$ s. In part (a) of each figure, the test configuration is shown; that is, the locations of the impact point and the receiving transducer relative to the reinforcing bars and to the flaw are shown.

As shown in Fig. 7.24(a), the receiver was located over a 25.4 bar and the impact point was 0.05 m away from the centerline of the bar. In the spectrum shown in Fig. 7.24(b), there is a peak at 2.44 kHz which corresponds to the frequency of P-waves diffracted around the flaw and reflected from the bottom of the plate, and a peak at 7.81 kHz which is the frequency of P-waves reflections from the surface of the 0.26-m deep flaw (Eq. (5.8)). There are also minor peaks at 14.6 and 21 kHz. These are the frequencies of reflections from the top of the bars. Using Eq. (7.1), these frequencies give depths of 71 and 49 mm, respectively; these depths are in good agreement with the known depths of 73 and 48 mm.

The test configuration in Fig. 7.25(a) was similar to that in Fig. 7.24(a), except that the impact point was also located over



a 25.4-mm diameter reinforcing bar. The frequency spectrum obtained for this test configuration is similar to that shown in Fig. 7.24(b), except that the secondary effects caused by the presence of the bars are different; the frequencies near 21 kHz are larger than the 14.6 kHz peak.

The key point is that the effects caused by the reinforcing steel are secondary and the disk-shaped flaw embedded in the reinforced concrete plate was easily detected. Similar results were obtained for the 0.205-m diameter flaws which were located 0.26 and 0.13 m below the top surface of the reinforced concrete plate (see Fig. 7.6). In the following section results obtained from a part of the reinforced concrete plate that contained a planar crack-like flaw are discussed.

#### 7.5.4 A Simulated Crack in Plain and Reinforced Concrete

Wave reflection from an actual crack in concrete is more complicated than the reflection that occurs from planar disk-shaped flaws. For the case of a disk-shaped flaw, the reflecting interface was a relatively smooth concrete/air interface, which reflects almost 100 percent of an incident wave's energy. The surfaces of a crack are rough and may be partially in contact with each other because of interlocking of aggregate particles. If contact between crack surfaces exists or is caused by the displacements produced by incident waves, then only a portion of the energy will be reflected; the remainder will be transmitted into the underlying concrete.

To simulate a crack, a 0.075-mm thick plastic sheet was

embedded in the plain and reinforced sections of the concrete plate (see Fig. 7.6). The sheet was 0.3 by 1 m in dimension. It was placed on the fresh concrete during casting of the plate after the concrete had been placed in the form to a level of approximately 0.18 m (0.32 m from the top of the form). Concrete was then placed on top of the sheet and casting of the plate was completed. (The depth of the crack was not known as precisely as for the planar disk-shaped flaws which were fixed in place prior to placement of the concrete.) The plastic conformed to the surfaces of the concrete between which it was placed.

Figs. 7.26 and 7.27 show results obtained from the simulated crack in a plain section of the plate and in a reinforced section of the plate. Fig. 7.26(a) shows the test configuration for an impact-echo test carried out over the crack-like flaw in plain concrete; Fig. 7.26(b) shows the waveform and frequency spectrum that were obtained. The impact source was the 20-g impactor (contact time approximately 80  $\mu$ s). A single peak occurs in the frequency spectrum at a value of 6.84 kHz. This frequency value corresponds to a depth of 0.30 m, which is close to the approximate depth of the crack that was measured during casting of the plate. There is also a lower amplitude peak at a frequency value of 3.42 kHz. This peak is related to the frequency of P-waves diffracted around the edges of the crack and reflected from the bottom surface of the plate. The fact that this lower frequency peak is shifted to a value less than the 3.91 kHz value corresponding to P-wave reflected directly from the bottom surface of a solid plate (Fig.

7.23), indicated that waves were diffracted around the edges of the crack and not transmitted across the crack.

Fig. 7.27(a) shows the test configuration for an impact-echo test carried out over the crack-like flaw in reinforced concrete; Fig. 7.27(b) shows the waveform and frequency spectrum that were obtained. As in the previous case, the impact source was the 20-g impactor (contact time approximately 80  $\mu$ s). The highest amplitude peak in Fig. 7.27(b) occurs at a value of 7.32 kHz instead of 6.84 kHz as in Fig. 7.26(b). A frequency of 7.32 kHz corresponds to a depth of 0.28 cm which is still close to the approximate depth of the crack measured during placement of the concrete. The lower frequency peak occurs at 3.91 kHz, the frequency of P-waves reflected from the bottom surface of the plate. There are also additional peaks that occur at values slightly higher than the 3.91 and 7.32 kHz peaks. These multiple peaks are thought to be caused by the presence of the reinforcing bars, as they are similar to the multiple peaks that were observed in the frequency spectra obtained from the plate containing bars (Figs. 7.20 and 7.21).

This result is encouraging as it appears to show that the impact-echo method will be able to locate cracks in plain and reinforced concrete. To extend the scope of the flaw studies, prior to field testing the method, other types of flaws were simulated. The results of these studies are discussed in the following section.

## 7.6 STUDIES OF OTHER TYPES OF FLAWS

In the 0.5-m thick concrete plates, several other types of

flaws that may be encountered in concrete structures were simulated. Results are presented for a simulated, vertical surface opening crack, a disk-shaped flaw inclined at an angle to the surface, and a thin metal duct, partially filled with mortar grout.

#### 7.6.1 Depth of a Surface Opening Crack

To simulate a vertical crack in concrete, a 0.075-mm thick plastic sheet was hung between two vertical metal supports which were spaced 0.4 m apart. The supports were fixed to the bottom of the form prior to casting the 0.5-m thick concrete plate (Fig. 7.7). The plastic sheet was 0.21 m deep. The objective was to locate the depth of a visible surface opening crack.

The impact point was located on one side of the crack and the receiving transducer was placed on the opposite side. Both the impact point and the receiver were located 0.06 m away from the crack. The test configuration is shown in Fig. 7.28(a). The impact source was the 5.5-g impactor (contact time approximately 72  $\mu$ s).

Diffraction of waves incident upon the bottom edge of the crack causes the edge to act as a source of cylindrical waves. Fig. 7.29(a) shows a P-wave incident upon the bottom edge of a vertical surface opening crack. Fig. 7.29(b) shows the diffracted P- and S-waves that are produced by the incident P-wave. The region behind the crack is a shadow zone - only diffracted waves can penetrate this zone. These diffracted waves are the first waves to arrive at the receiving transducer. Reflection of these



diffracted waves occurs at the top surface of the plate. As these reflected waves propagate down through the plate they are incident upon the bottom edge of the crack giving rise to new diffracted waves. Thus, the cycle of diffraction at the bottom edge of the crack and reflection at the top surface of the plate begins again; this cycle gives rise to a resonance condition with a frequency of wave arrivals at the receiver which corresponds approximately to twice the depth of the crack. In addition, diffracted waves are reflected by the bottom surface of the plate, as are the direct P- and S-waves that propagate past the crack. As these reflected waves propagate back up through the plate, they are incident upon the bottom edge of the crack giving rise to additional diffracted waves. Therefore there are additional resonances that are set-up between the bottom surface of the plate and the bottom edge of the crack, the top and bottom surfaces of the plate. Thus, in a frequency spectrum, it would be expected that these different resonances would give rise to multiple high amplitude peaks.

The waveforms and frequency spectrum obtained from the impact-echo test are shown in Fig. 7.28(b). As expected, the spectrum looks different from those presented in previous sections. There are three closely spaced peaks at 3.42, 4.88, and 6.35 kHz and a lower amplitude peak at 9.27 kHz. Each of these peaks corresponds to various periodicities of waves reflected between the surfaces of the plate and the bottom edge of the crack.

The peak occurring at the highest frequency value (9.27 kHz in this case) is the frequency that the cycle of P-wave reflection



from the top surface of the plate and diffraction from the bottom edge of the crack occurs. For a relatively close spacing between the impact point and the receiver, this frequency corresponds approximately to twice the depth of the crack (Eq. (5.8)). For this example, a frequency of 9.27 kHz corresponds to a depth of 0.22 m, which is close to the measured depth of 0.21 m.

#### 7.6.2 Flaw Oriented at an Angle to the Surfaces of a Plate

A 0.5-m diameter disk-shaped flaw was embedded in the 0.5-m thick plain concrete plate at an angle of 30 degrees to the top and bottom surfaces of the plate (see Figs. 7.4 and 7.5). Fig. 7.30 shows an elevation view of the cross-section of the plate containing the inclined flaw. The location of the disk prior to placement of the concrete is shown by the dashed line. During concrete placement, the disk broke, creating a discontinuity in the surface of the flaw. Thus the inclined flaw actually consisted of two discontinuous pieces.

Impact-echo tests were carried out at points A through E shown in Fig. 7.30; these points were spaced 0.1 m apart on the surface of the plate over the centerline of the flaw. The impact sources for the tests were 8- or 9.5-mm diameter spheres (contact times of 44 to 52  $\mu$ s). The receiver was located at points A through E and the impact point was located 0.03 m to the right of the receiver, as shown in Fig. 7.30.

Fig. 7.31 shows the waveform and the corresponding frequency spectrum obtained at each test point. The frequency value of the

peak amplitude in each spectrum was used to calculate the depth of the reflecting interface at each point (Eq. 5.8). The fact that the frequency peak shifts to higher and higher values in Figs. 7.31(a) through (e) indicates that the flaw is not parallel to the top surface. Therefore, the calculated depths of the reflecting interfaces are not vertical depths, but are perpendicular distances from the impact point to the plane of the flaw. At each test point, an arc with a radius equal to the calculated depth at that point is drawn. The location of the interface is found by drawing a tangent the arcs, as shown in Fig. 7.30. Note that at point C there are two peaks in the frequency spectrum (Fig. 7.31(c)); each of these peaks was used to calculate two radii to be drawn from point C. The arc calculated from the frequency of 7.81 kHz was consistent with the tangent drawn through points D and E, while the arc calculated from the frequency of 6.84 kHz was consistent with the tangent drawn through points A and B. Therefore, it appears that the disk broke near point C.

In this study, tests were also carried out for the impact point located to the left of the receiver and adjacent to the receiver on a line perpendicular to the cross-section shown in Fig. 7.30. In some cases, the value of the peak frequency shifts to a slightly lower value; this is expected since the point of ray reflection is at a lower point on the flaw. In all cases, the reflecting interface was easily detected and it could be determined that the interface was inclined.

### 7.6.3 Grouted and UngROUTED Metal Duct

In post-tensioned concrete structures, a common concern is whether the ducts containing the post-tensioning strands have been fully filled with mortar grout after the post-tensioning operation is completed. A nondestructive test method is needed to determine the extend of grout penetration in these ducts. As a first look at this problem, a thin galvanized sheet metal duct, 0.1 m in diameter and 1.52 m long, was partially filled over a length of 0.58 m with mortar grout. After the mortar hardened, the partially filled duct was embedded in the 0.5-m thick reinforced concrete plate. The distance from the top surface of the plate to the top of the duct was 0.15 m (Fig. 7.6 and 7.7).

A brief discussion of the nature of wave reflection from a thin steel interface between concrete and air and between concrete and mortar is followed by a discussion of the experimental results.

When an interface is very thin (an interface is considered thin when its thickness is small compared to the component wavelengths in the propagating wave [43]), as is the case for the 0.5-mm thick steel duct, then the nature of wave reflection is different than that discussed in Section 7.5.1. Consider a concrete plate bonded to a thin steel layer which has a stress-free boundary at its lower surface (a hollow duct). Since the stresses are zero at the steel/air interface, and the steel is thin, then the stresses are also approximately zero at the concrete/steel interface. Thus the presence of the thin steel layer will not affect the propagating

wave, and wave reflection occurs as from an air interface; incident waves are reflected at the air interface as waves of opposite sign.

If the thin layer of greater acoustic impedance (rigidity) is between two solids of like acoustic impedances (steel duct between concrete and mortar in the case of a fully grouted duct), then the thin layer is in effect transparent to the incident waves. The interface does not interfere with stress wave transmission [43]; thus, the waves propagate directly through the fully grouted duct. Note that the thin sheet of plastic placed in the concrete reflected incident waves. Although the layer was thin, it was composed of a material that had a lower acoustic impedance (lower rigidity) than the concrete on either side of it; therefore, the layer of plastic was not transparent to the propagating waves.

Figs. 7.32 and 7.33 show waveforms and frequency spectra obtained by transforming waveforms recorded over the grouted and hollow sections of the duct. The results shown in Fig. 7.32 were generated by the 20-g impactor (contact times approximately 70  $\mu$ s). The results shown in Fig. 7.33 were generated by a 7-mm diameter sphere (contact times approximately 44  $\mu$ s). Both the impact point and the receiver were located over the centerline of the duct. The distance between the impact point and the receiver was 0.05 m.

The waves generated by the 70- $\mu$ s duration impact contained very little energy in the frequency range that would be reflected by the duct. However, effects caused by the presence of the duct can be seen in the frequency spectra. In the spectrum obtained from the hollow duct (Fig. 7.32(b)), there is a single peak at 3.42



kHz; this value is related to the frequency of P-waves diffracted around the hollow duct and reflected from the bottom of the plate. If Figs. 7.32(a) and (b) are compared, two differences are apparent: 1) the relative amplitude of the 3.42 kHz peak as compared to the other frequencies that are present in the spectrum in Fig. 7.32(b) is much higher than the relative amplitude of the 3.92 kHz peak as compared to the other frequencies that are present in the spectrum in Fig. 7.32(a). In addition, the amplitude of the 3.42 kHz peak is approximately three times greater than the amplitude of the peak in the spectrum obtained from the grouted duct. These differences in amplitude indicate that losses occur as the waves propagate through the grouted duct. Losses probably result from the fact that the actual test situation - thin steel layer between mortar and the concrete - is not an ideal case of a thin, higher acoustic impedance layer between two materials with the same impedance. The acoustic impedance of the mortar was somewhat less than that of the concrete; thus, wave traveling through the duct also undergo multiple reflections within the duct, scattering the wave energy. 2) The highest amplitude occurs at a frequency of 3.91 kHz, the value obtained from a solid plate, rather than 3.42 kHz. This indicates that the waves traveled directly through the grouted duct rather than around the duct as was the case for a hollow duct.

The 44- $\mu$ s duration impact generated waves containing a broader range of frequencies than the 70- $\mu$ s duration impact; thus, the effects caused by waves reflected from the surface of the duct could be studied. In the spectrum obtained from the hollow duct (Fig.



7.33(b)), in addition to the 3.42 kHz peak produced by waves reflected from the bottom surface of the plate, there is a high amplitude peak at 13.7 kHz which corresponds to a depth of 0.15 m (Eq. (5.8)), the measured distance to the top of the duct. However, in the spectrum obtained from the grouted duct (Fig. 7.33(a)), the only peak occurs at 3.91 kHz. Because of the relatively low amplitude of this peak, the frequencies produced by the R-wave (Chapter 5) are apparent in the spectrum. Thus, the hollow duct acts like a cylindrical air void and produces high amplitude reflections, while the grouted duct cannot be detected because the thin interface is transparent to the propagating waves.

Thus, it appears possible to distinguish ducts that are hollow or only partially grouted (air voids exist) from ducts that are fully grouted using frequency spectra obtained from impact-echo testing carried out directly over the ducts. For impacts having longer contact times, it seems that the absence of the grout can be inferred from the difference in the relative amplitudes of the peaks that are related to the plate thickness. For impacts having shorter contact times, the absence of the grout can be inferred by a peak at a frequency corresponding to the depth of the duct.

## 7.7 SUMMARY and CONCLUSIONS

This chapter has described the development and implementation of an impact-echo technique for flaw detection in plain and reinforced concrete.

To confirm the conclusions drawn from the studies of

theoretical displacement waveforms and their corresponding frequency spectra (Chapters 4 and 5), experimental studies on solid plates were carried out. The effects caused by changing the test configuration (impact source - receiver spacing) and by varying the contact time of the impact on waveforms and frequency spectra were studied. To determine the thickness of plate elements, it was found that it was necessary to keep the distance between the impact point and the receiving transducer less than approximately 0.5 times the thickness of the plate. The contact time of the impact is of minor importance as long as the stress pulse produced by the impact contains sufficient energy in the range of frequencies that have wavelengths corresponding to twice the plate thickness. These results were as expected based on the results presented in Chapters 4 and 5.

To confirm conclusions drawn from time domain studies of plates containing planar flaws (Chapter 6), experimental studies were carried out on a plate containing planar disk-shaped flaws. The effects on waveforms caused by varying the contact time of the impact, and the diameter and depth of planar, disk-shaped flaws verified observations drawn from the finite element analyses presented in Chapter 6. In the experimental studies, frequency spectrum analysis was emphasized, and the effects of the above-mentioned variables on frequency spectra were also discussed. From frequency spectrum analysis, it was found that a flaw will be detected and accurately located using impacts having contact times ranging from 20 to 80  $\mu$ s and D/T values less than or equal

to 2 if the following two conditions are satisfied: 1) the ratio of the diameter of the flaw to the depth of the flaw ( $D/T$ ) must be greater than approximately 0.6; and, 2) the ratio of the contact time of the impact to the arrival time of the 2P-wave reflected from the surface of the flaw ( $t_c/t_{2p}$ ) must be less than approximately 0.75.

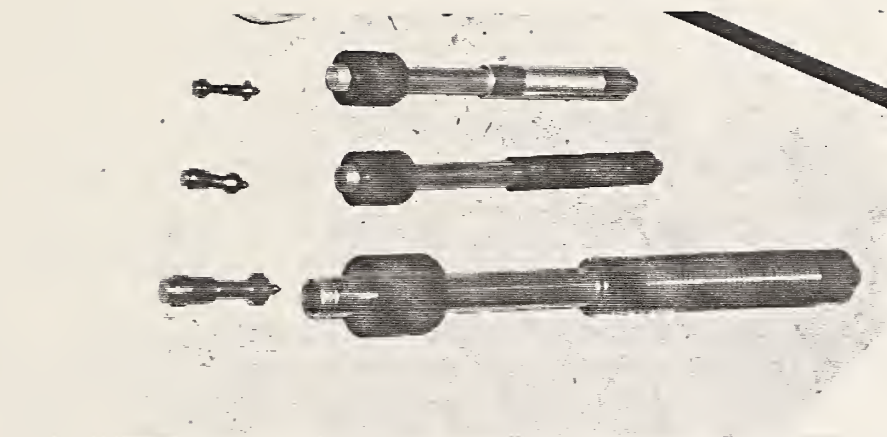
Wave reflection from a concrete/steel interface was discussed and the effects on waveforms and frequency spectrum produced by steel bars embedded in concrete were determined. It was shown that flaws within reinforced concrete could be detected by using longer contact times to minimize the effects caused by the reinforcing bars.

The results of several other types of flaw studies were presented. It was shown that the depths of simulated horizontal cracks in plain and reinforced concrete, the depth of a vertical surface opening crack, and the orientation of a flaw placed at an angle to the surfaces of a plate could be determined, and a hollow metal duct could be distinguished from a fully grouted duct.

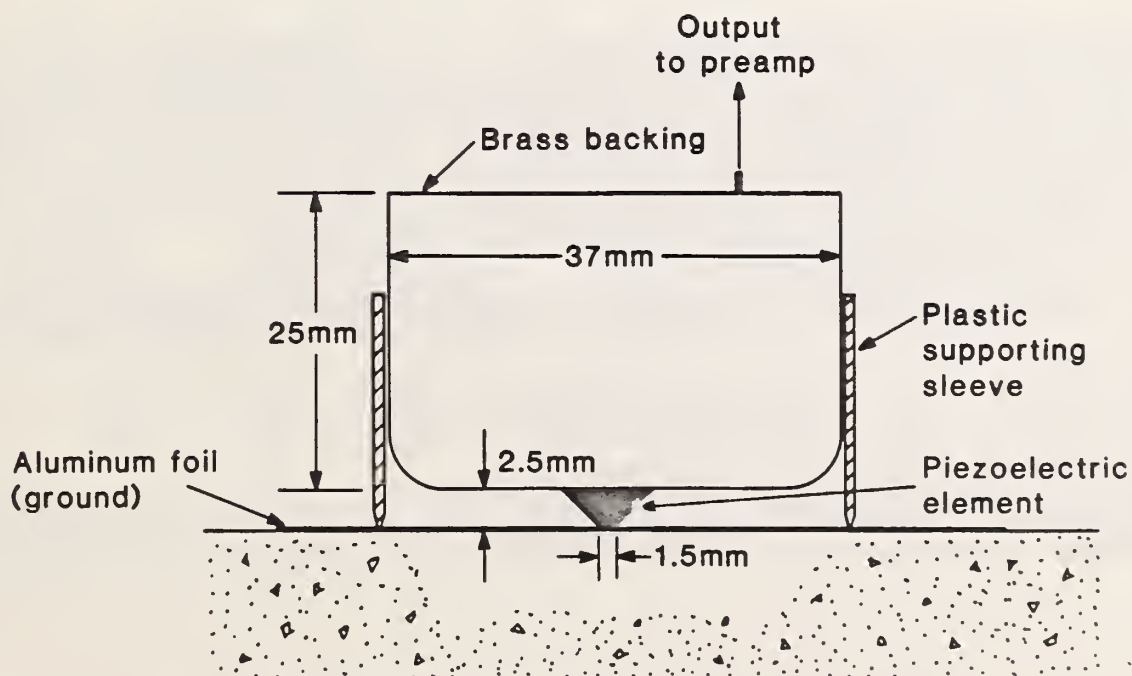
In all of the studies presented in this chapter, frequency domain analysis of displacement waveforms was emphasized. Both time domain and frequency domain analyses require knowledge of the P-wave velocity in a test object. It was shown that P-wave velocity is affected by the measurement method. Velocities determined using the through-transmission, ultrasonic pulse-velocity method were higher than velocities determined using the impact-echo method. Thus velocities obtained from an impact-echo test on a part of a

test object of known thickness must be used for accurate interpretation of impact-echo waveforms and frequency spectra.

The results presented in this chapter show that the impact-echo technique works very well in laboratory studies. The successes that have been achieved in the laboratory strongly suggest that the method has the potential to become a practical field technique for detecting flaws within concrete structures.

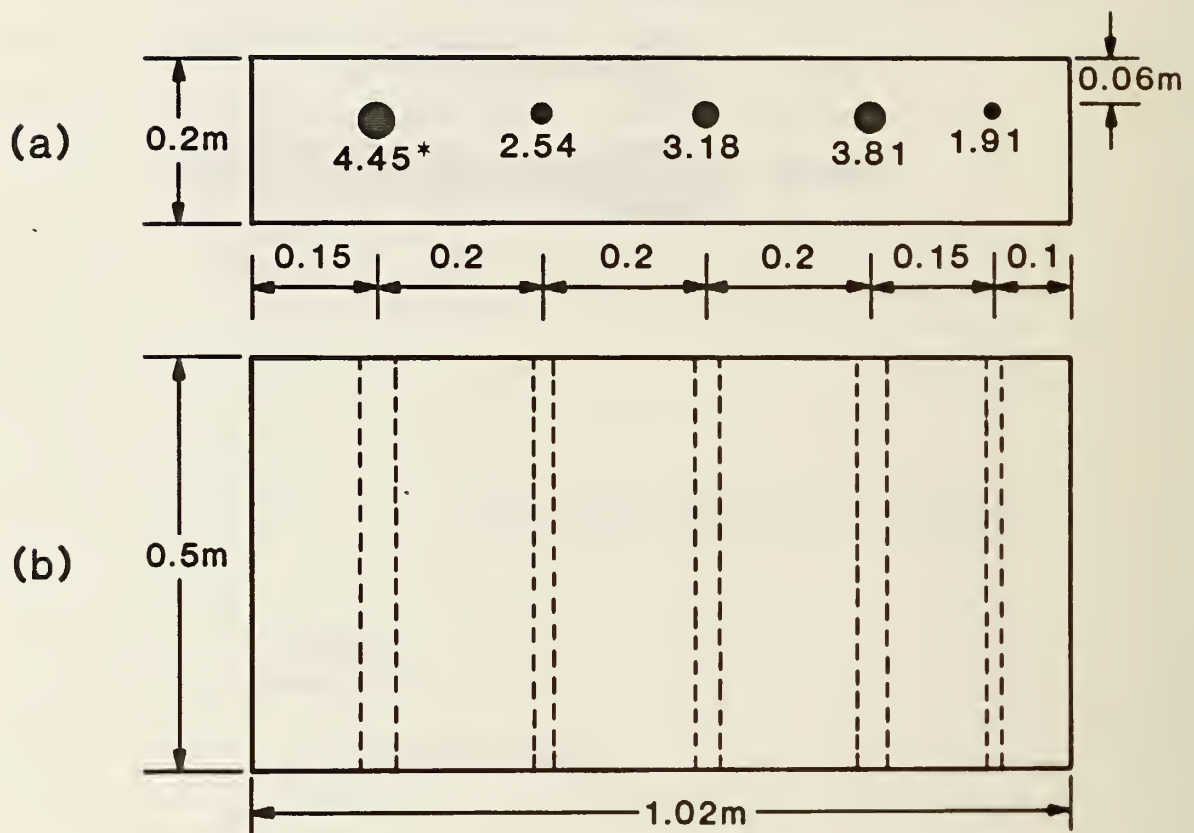


7.1 Impactor with spring driven mass.



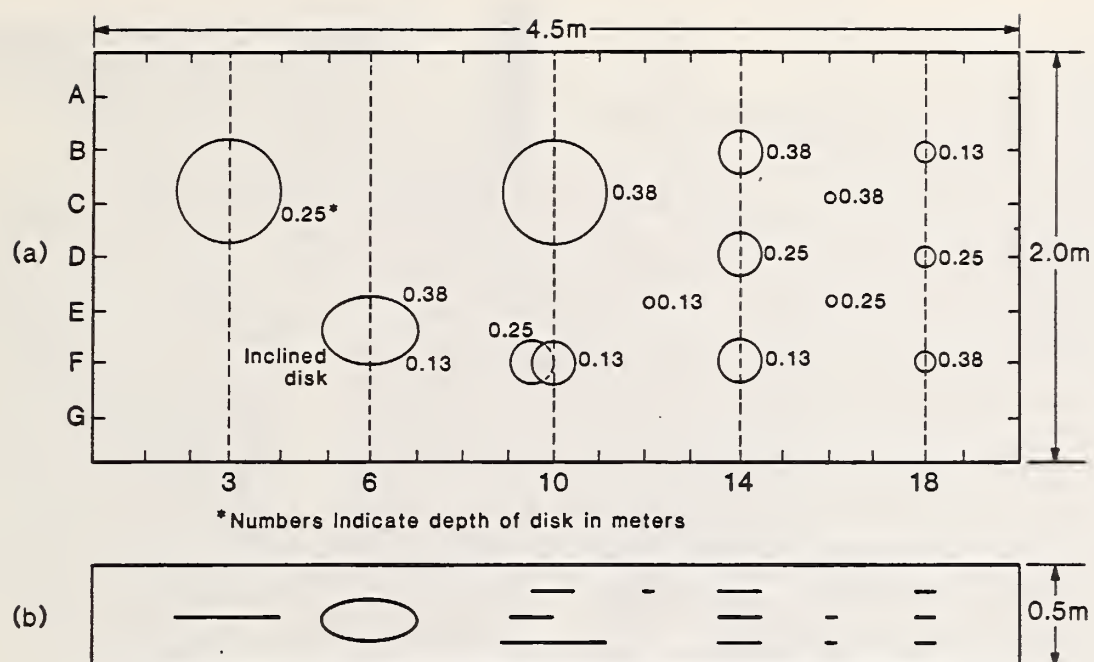
7.2 NBS conical displacement transducer.





\* Diameter of steel bar (cm)

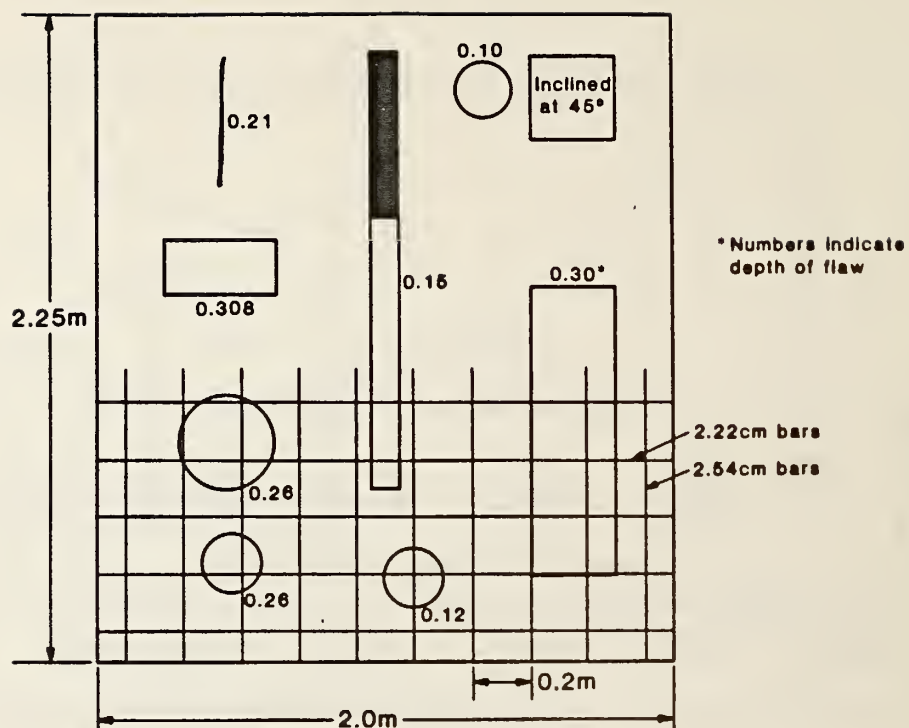
7.3 0.2-m thick concrete plate containing steel bars: a) elevation view; and, b) plan view.



7.4 0.5-m thick concrete plate containing polyurethane disks: a) plan view; and, b) elevation view.



7.5 Formwork for 0.5-m thick concrete plate with disks in place prior to placement of concrete.

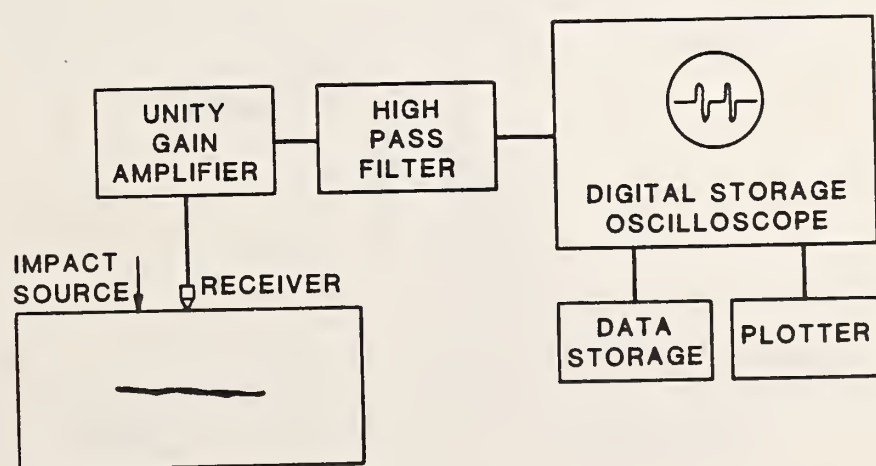
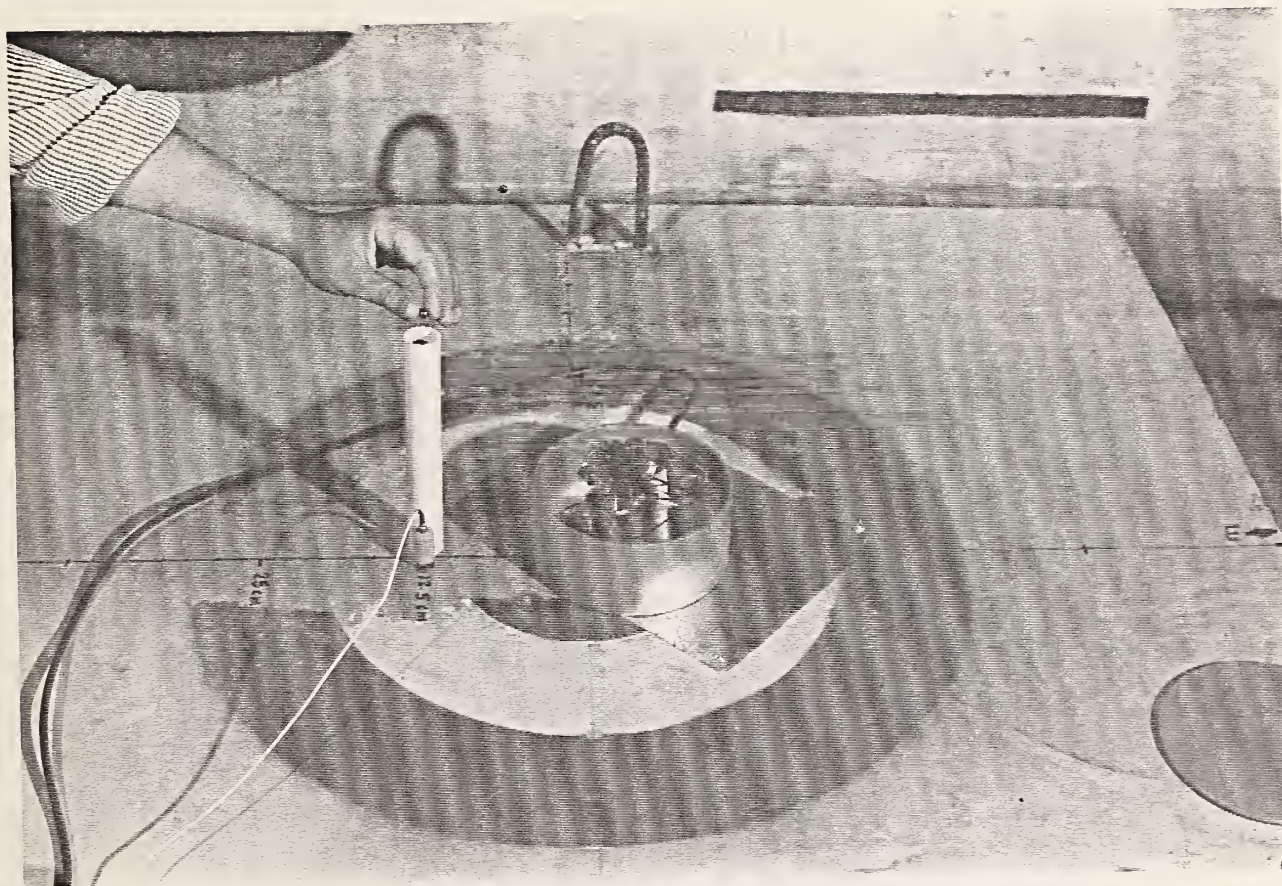


7.6 Plan view of 0.5-m thick reinforced concrete plate containing artificial flaws.

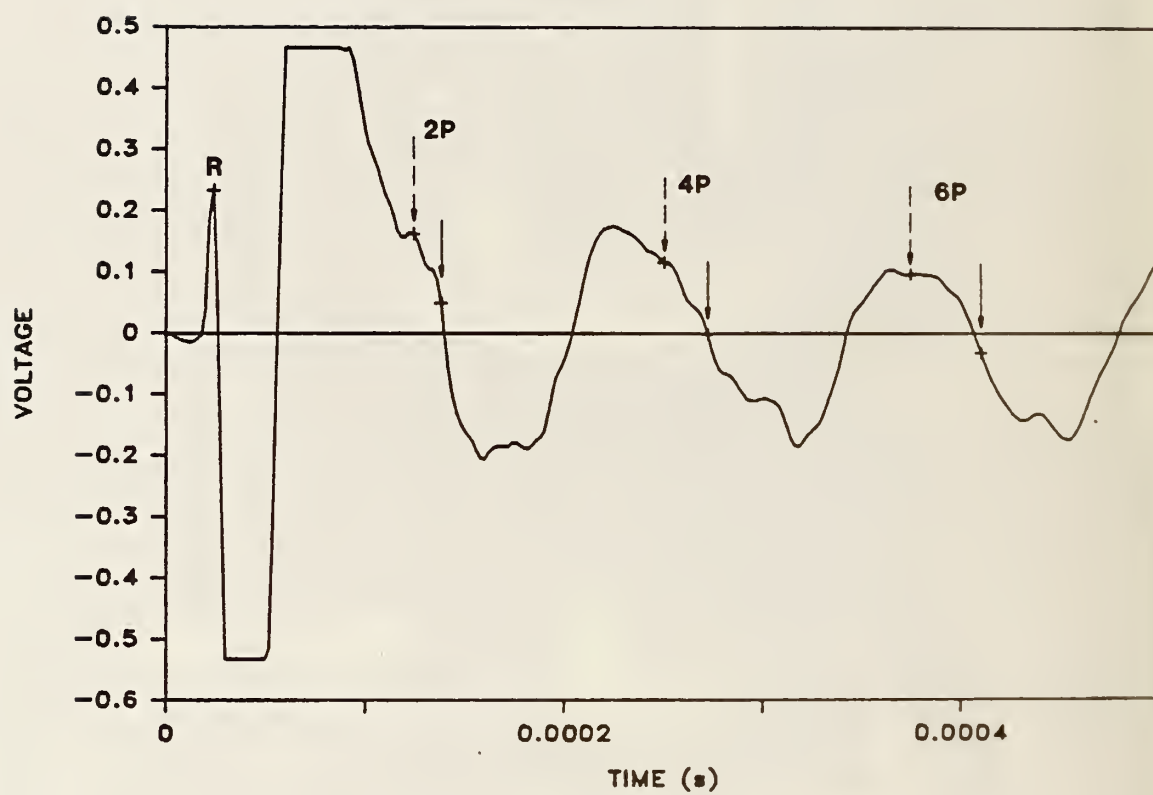


7.7 Formwork for 0.5-m thick reinforced concrete slab with flaws in place prior to placement of concrete.



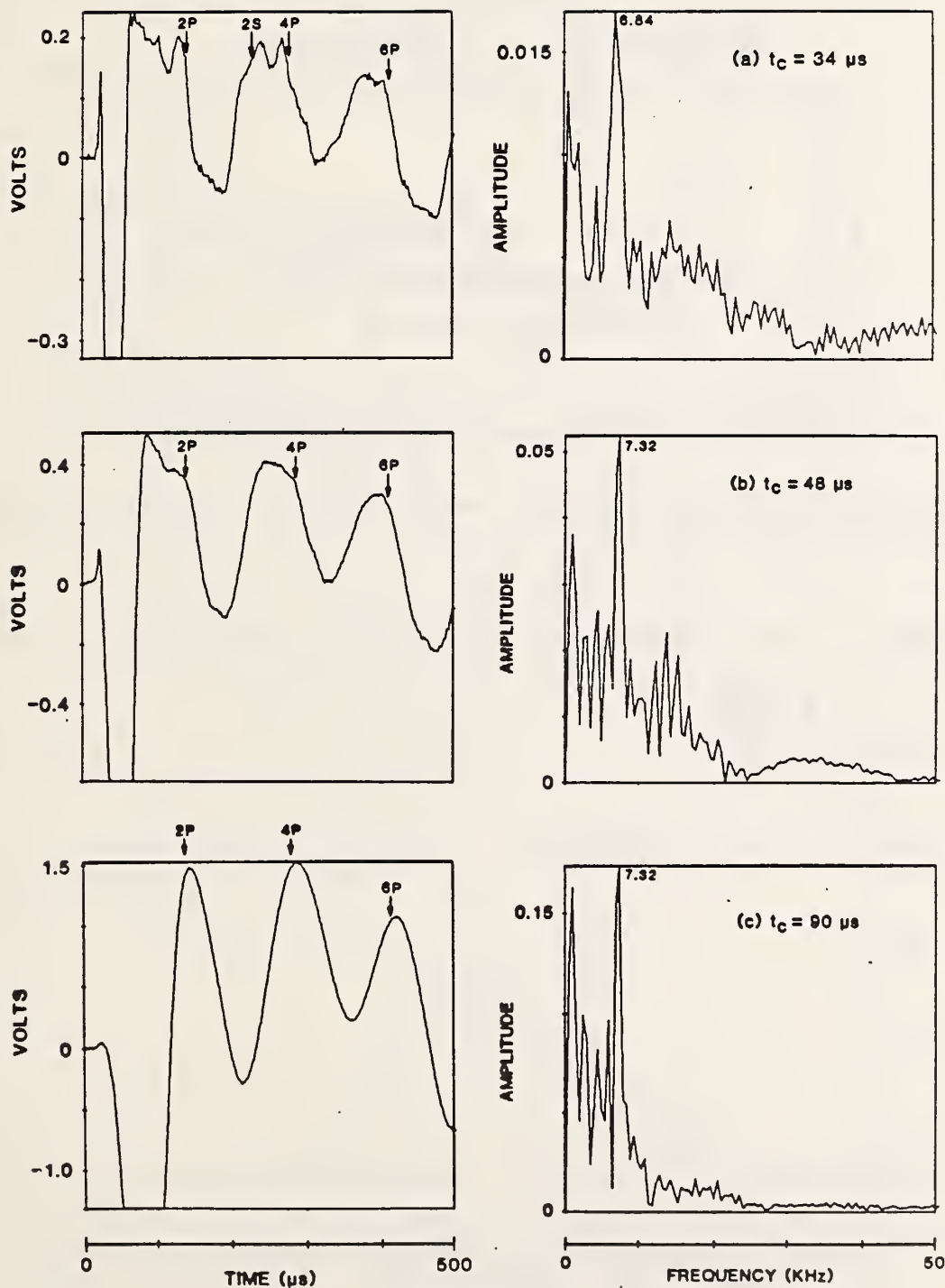


7.8 Test set-up: a) experimental set-up; and, b) schematic representation.

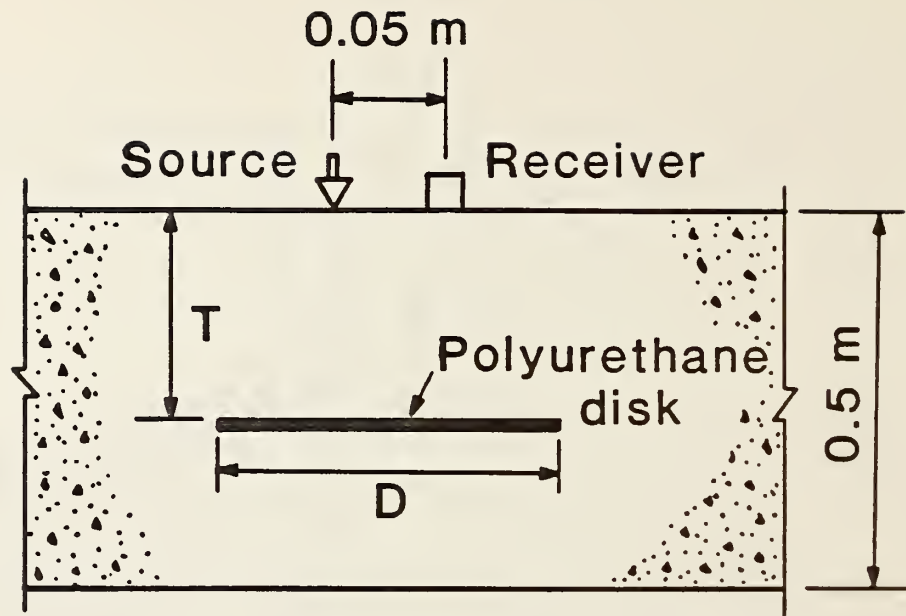


7.9 Surface displacement waveform obtained from 0.25-m thick concrete plate showing computed wave arrival times.

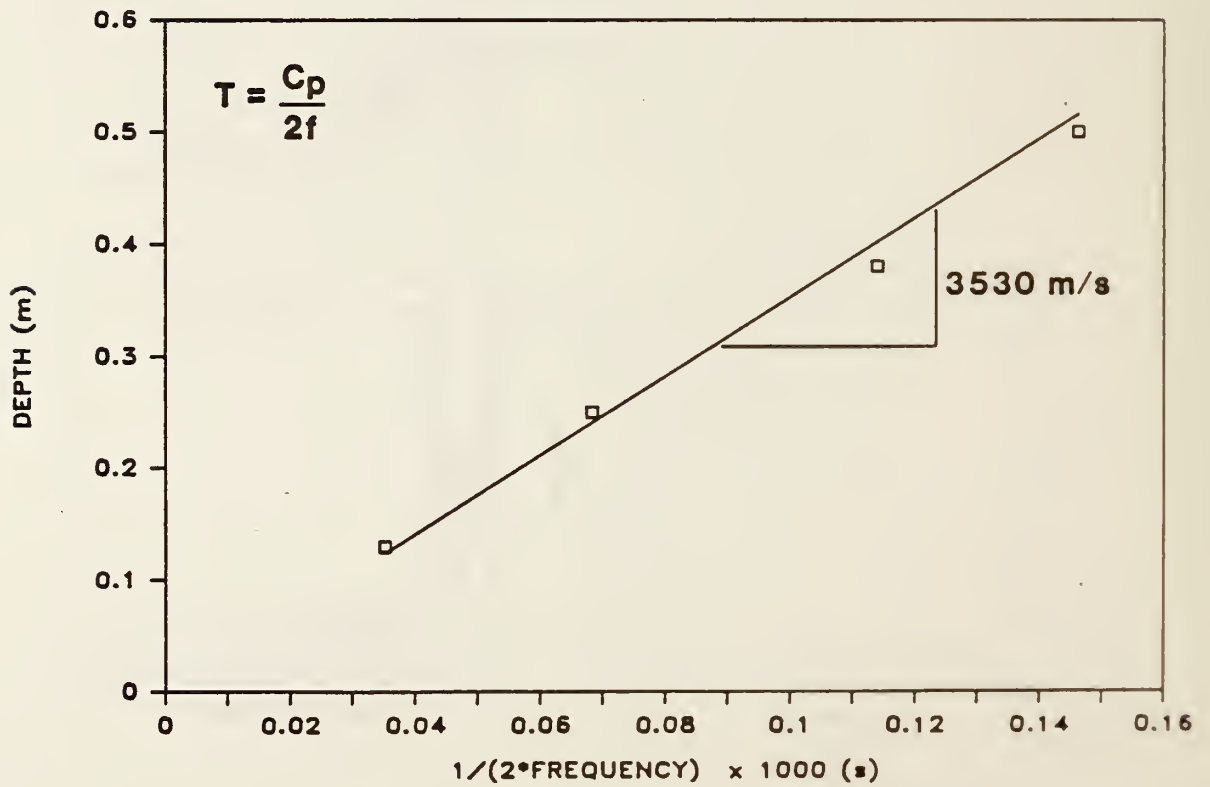




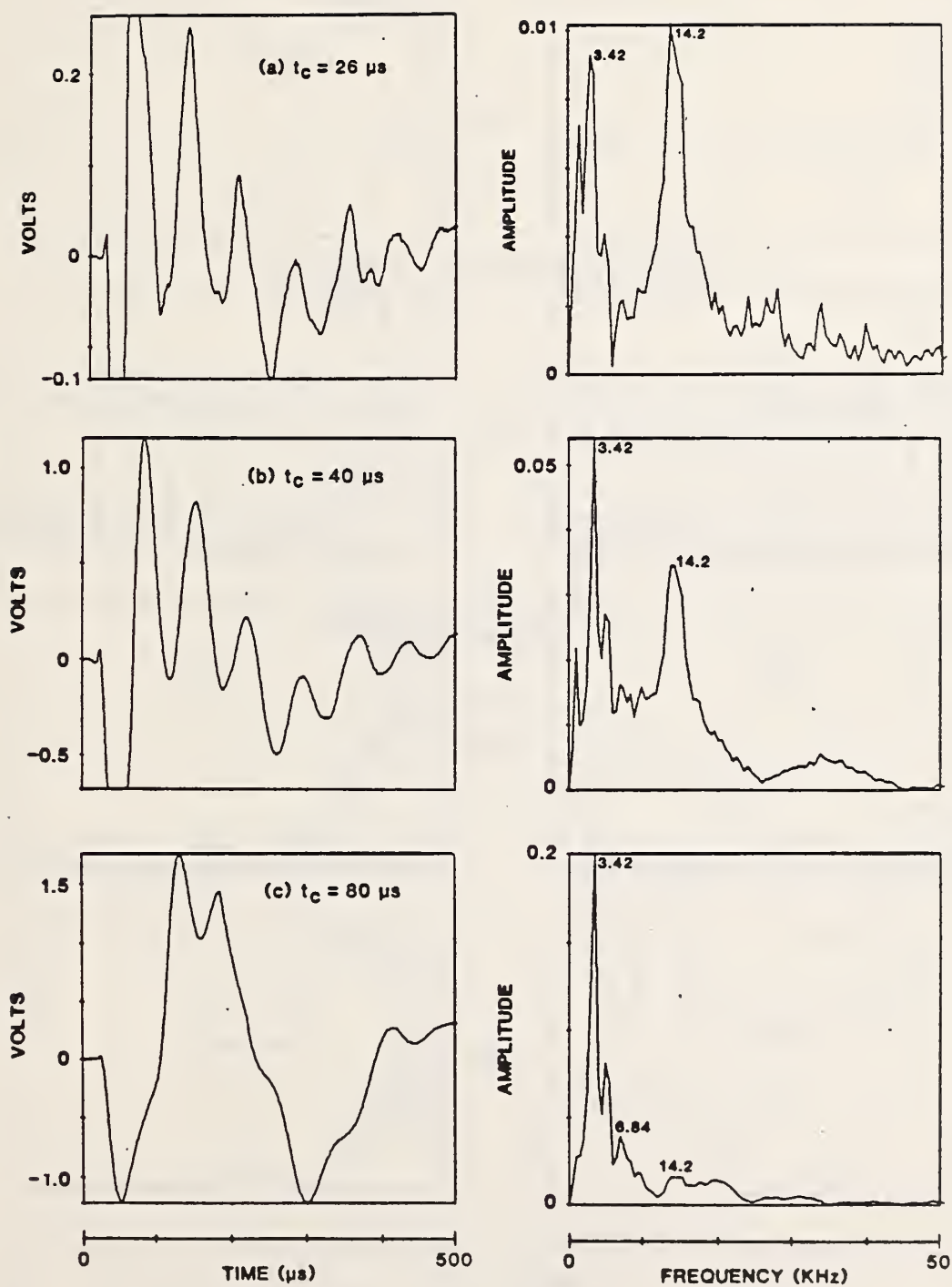
7.10 Waveforms and frequency spectra obtained from the 0.25-m thick concrete plate using various duration impacts: a)  $34 \mu s$ ; b)  $48 \mu s$ ; and, c)  $90 \mu s$ .



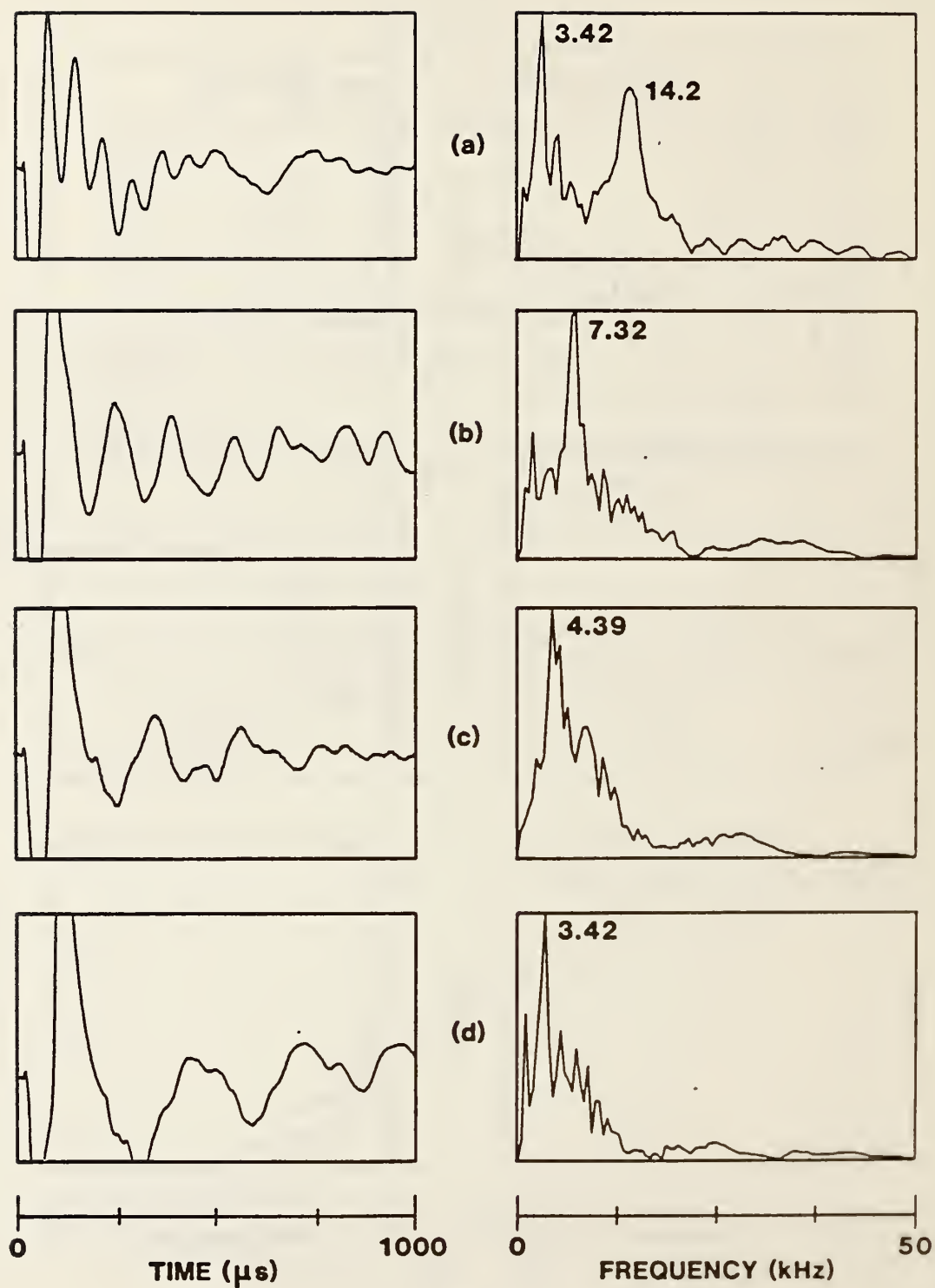
7.12 Test configuration for tests carried out over planar disk-shaped flaws.



7.13 Relationship between depth and frequency.

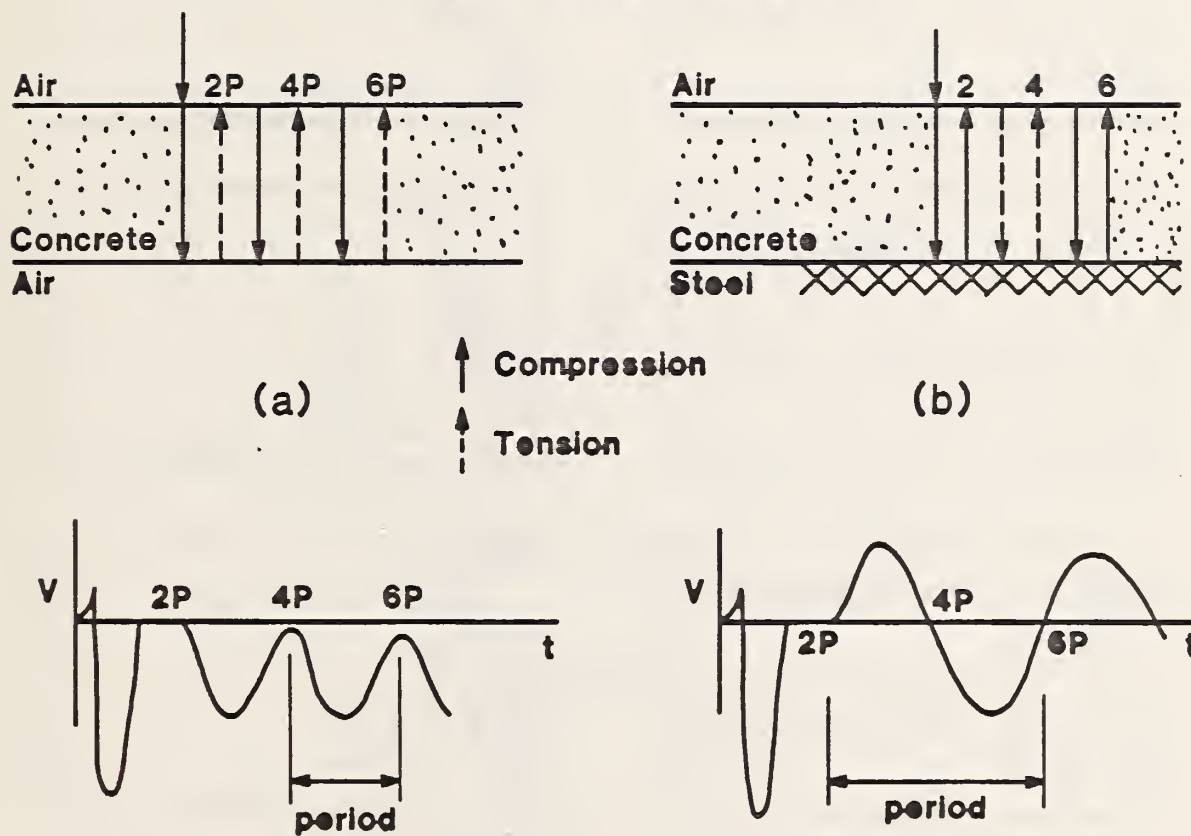


7.15 Waveforms and frequency spectra obtained over a 0.2-m diameter disk-shaped flaw located 0.127 m below the top surface of the 0.5-m thick plate. Duration of the impacts was: a) 26  $\mu s$ ; b) 40  $\mu s$ ; and, c) 80  $\mu s$ .



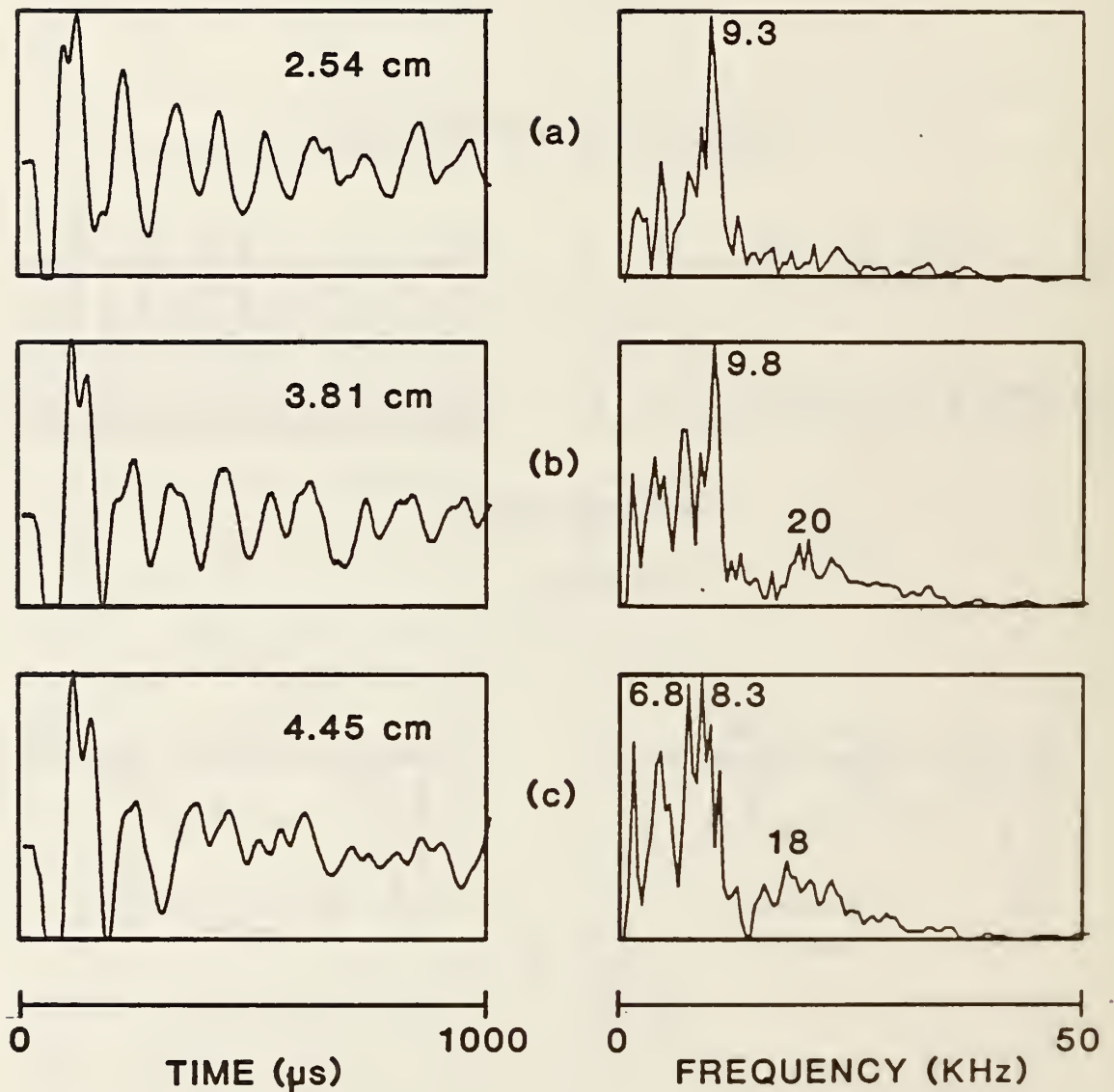
7.17 Waveforms and frequency spectra obtained from flaws located at various depths in the 0.5-m thick concrete plate: a) 0.127 m; b) 0.258 m; c) 0.38 m; and d) bottom surface of the plate (0.5 m).

## EFFECT OF INTERFACE

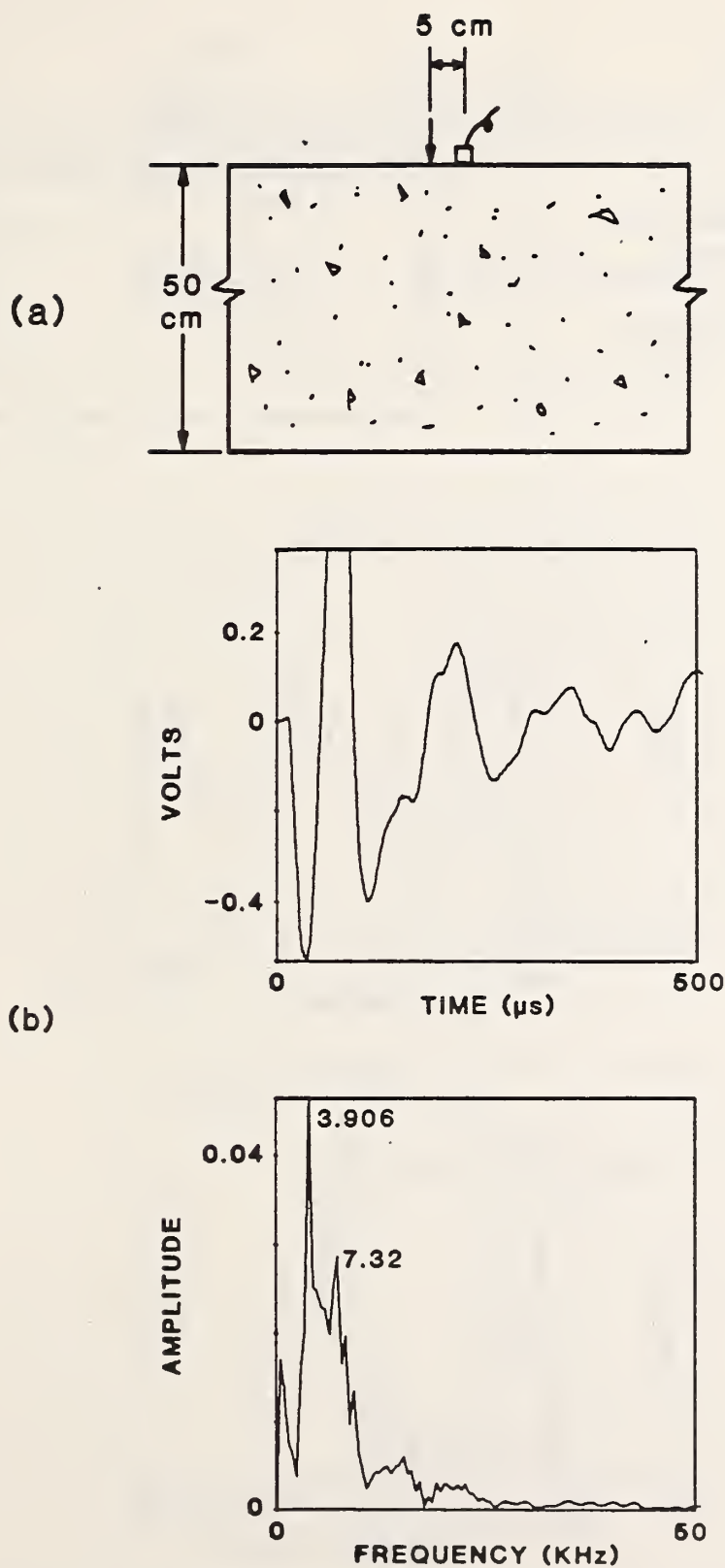


7.19 Wave reflection from concrete/air and concrete/steel interfaces.

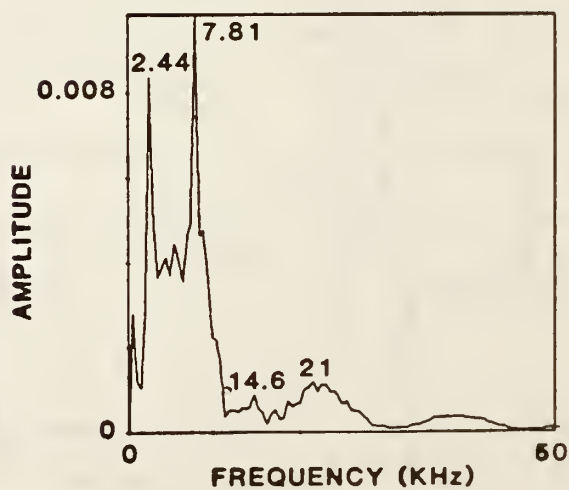
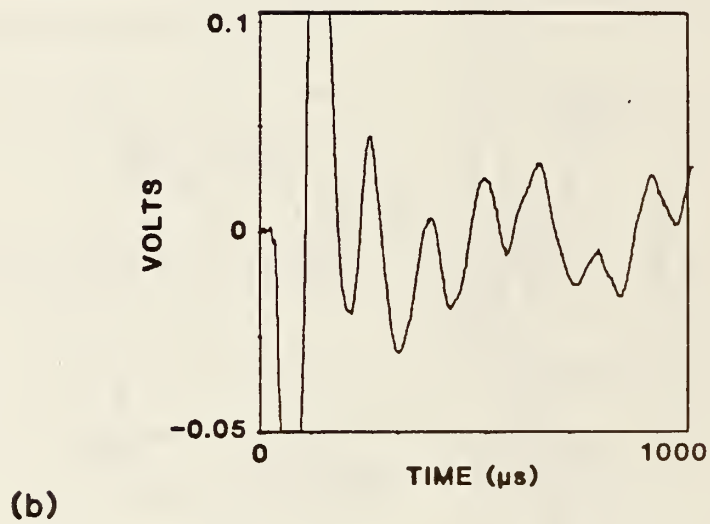
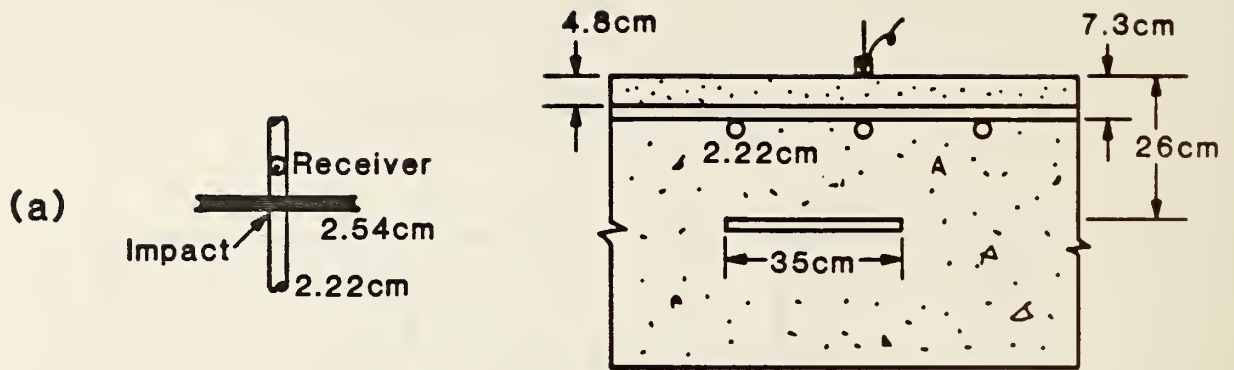




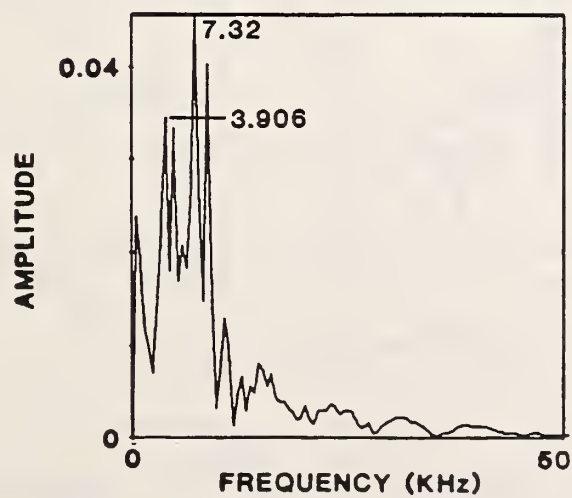
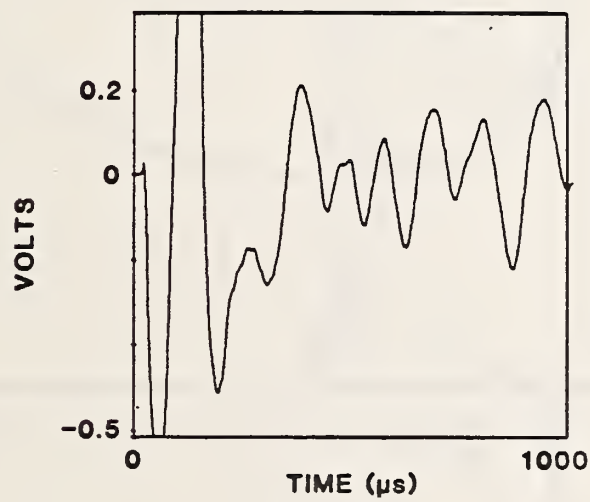
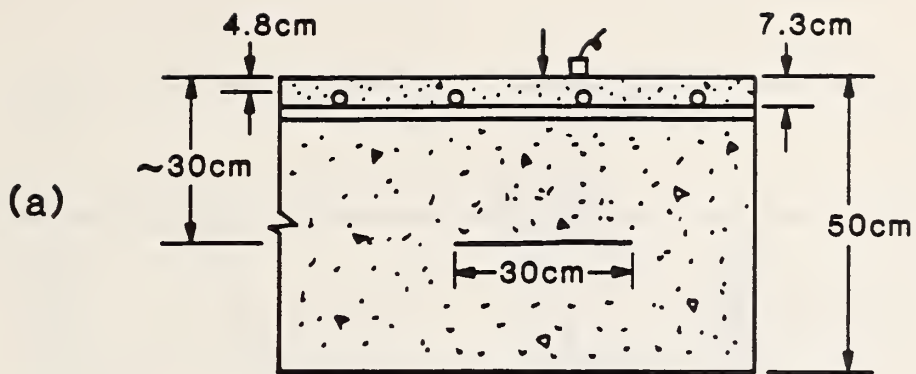
7.21 Waveforms and frequency spectra obtained from different diameter bars located 0.06 m below the top surface of the 0.2-m thick concrete plate; contact time of the impact was 54  $\mu\text{s}$ : a) 2.54 cm; b) 3.81 cm; and, c) 4.45 cm.



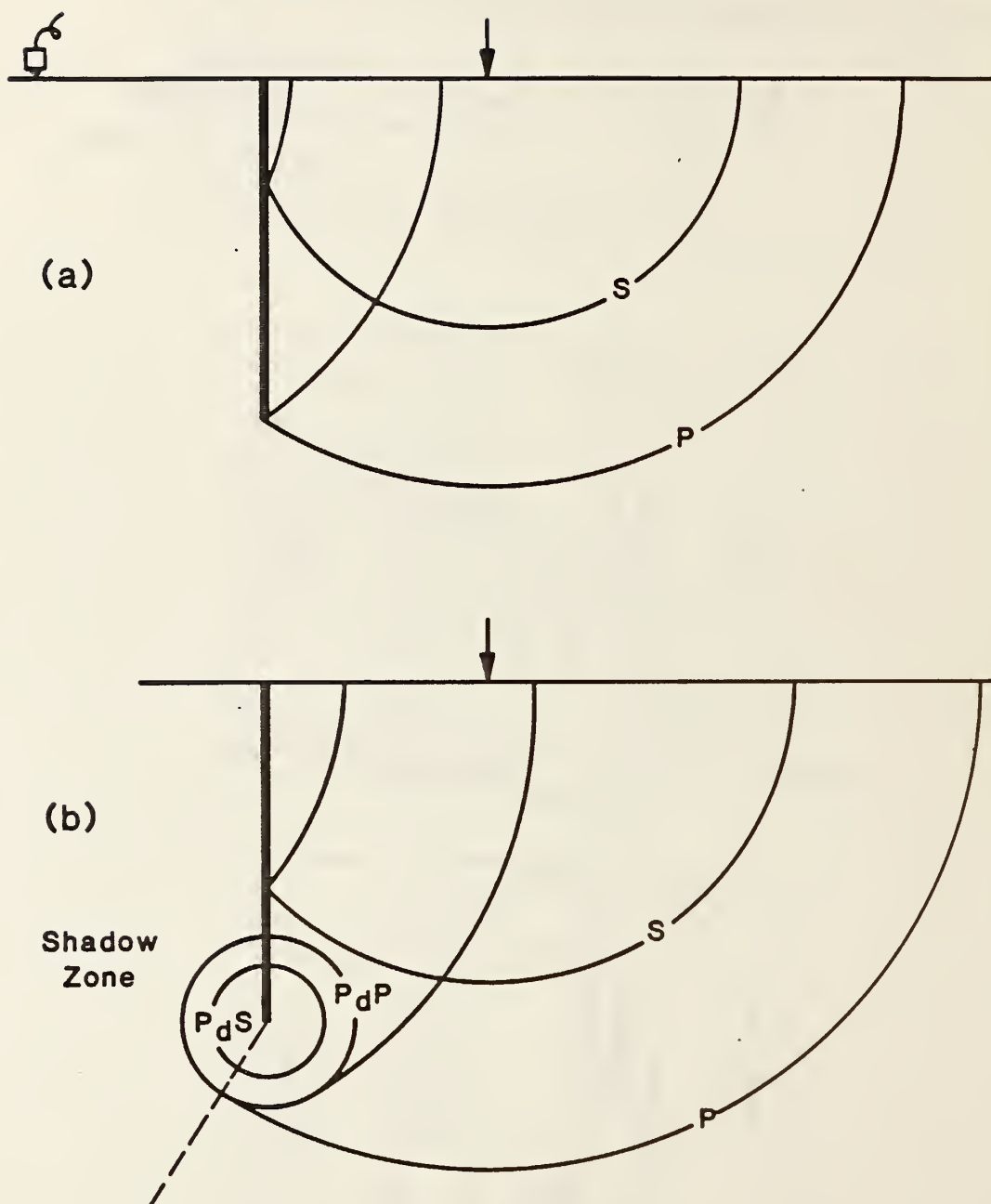
7.23 Waveform and frequency spectrum obtained from a plain section of 0.5-m thick concrete plate containing a variety of flaws and reinforcing bars.



7.25 Response obtained over the 0.35-m diameter flaw shown in Fig. 7.24 for a different test configuration: a) test configuration; and, b) waveform and frequency spectrum.

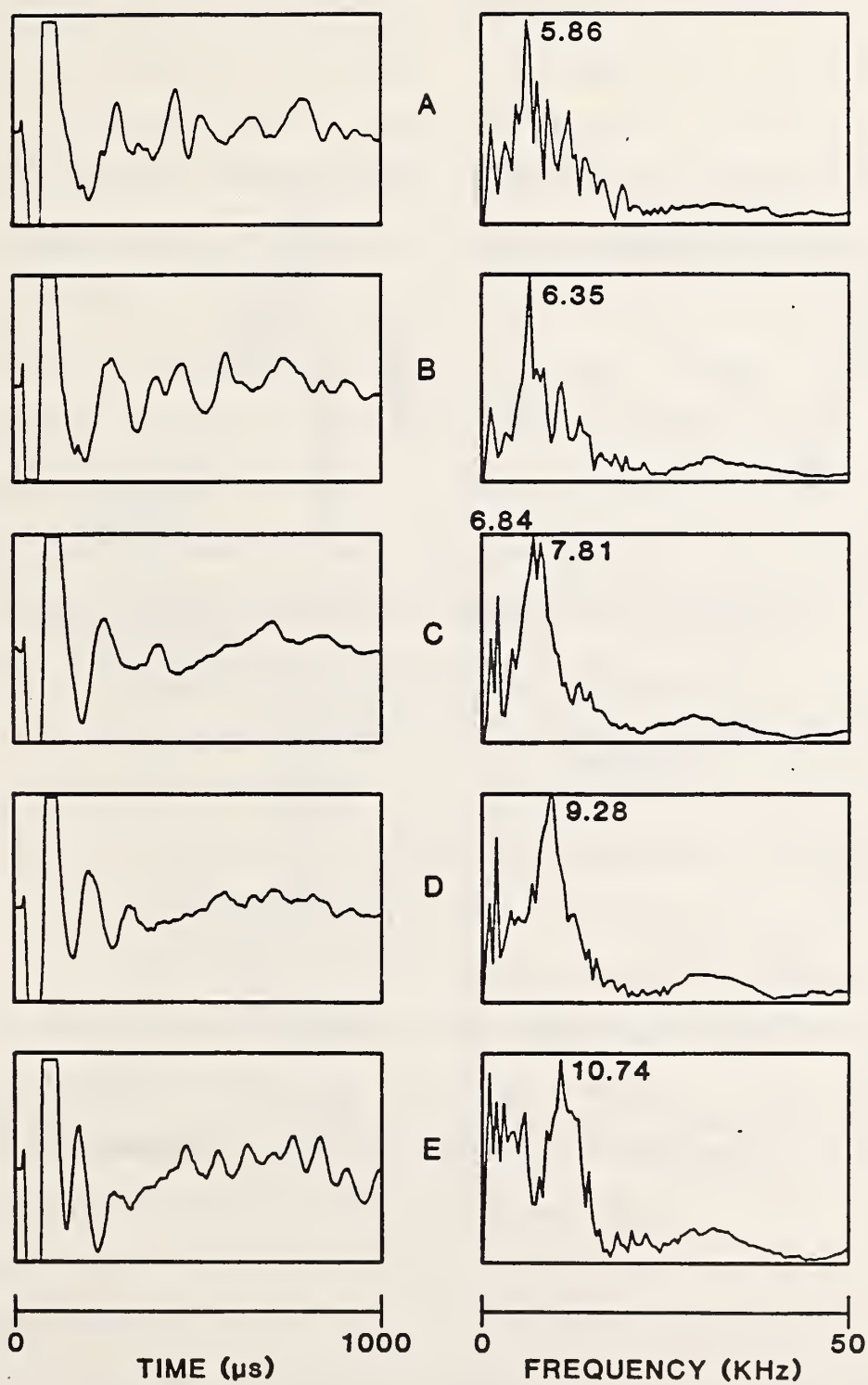


7.27 Response obtained over a simulated crack in reinforced concrete: a) test configuration; and, b) waveform and frequency spectrum.

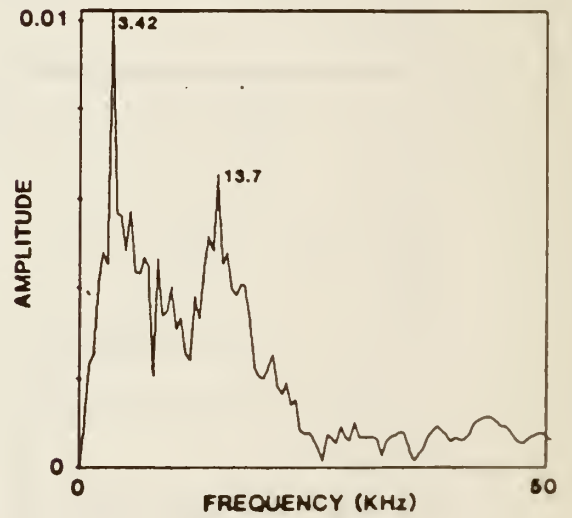
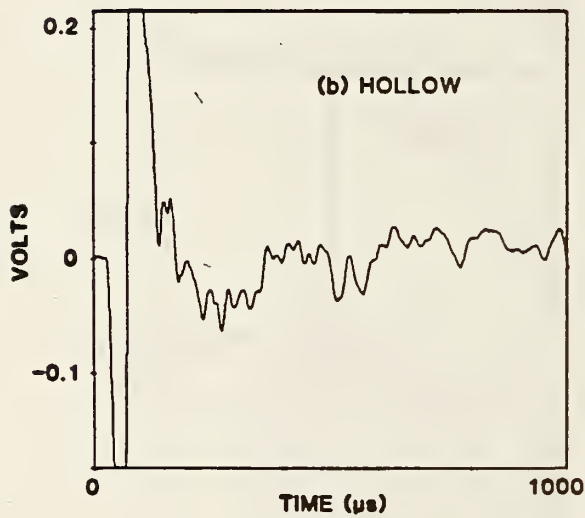
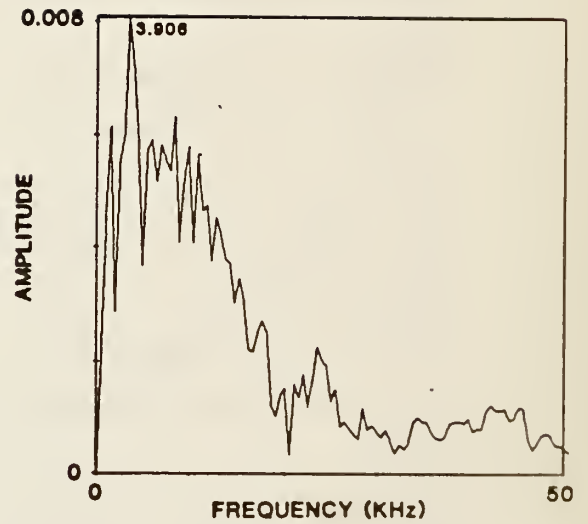
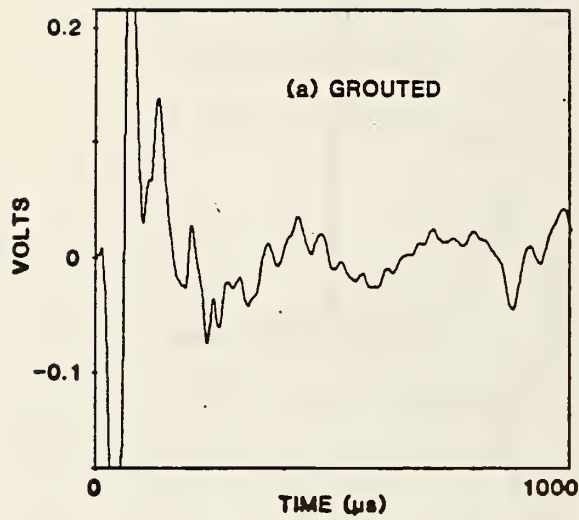


7.29 Schematic illustration of interaction of waves with vertical surface opening crack.





7.31 Waveforms and frequency spectra obtained at various points over the inclined flaw shown in Fig. 7.30.



7.33 Responses obtained over duct for a contact time of 25  $\mu$ s: a) waveform and frequency spectrum for hollow duct; and, b) waveform and frequency spectrum for grouted duct.

propagation in plates containing flat-bottom holes and planar disk-shaped flaws. The analyses presented in this report were limited to axisymmetric problems. The capability of the finite element code to accurately model displacements caused by the diffraction effects produced by the interaction of transient waves with a planar flaw was verified by comparison to an experimentally obtained surface displacement waveform. Parameter studies were carried out to determine the effects of test variables, such as flaw geometry and the contact time of the impact, on surface displacement waveforms.

The development of an experimental impact-echo technique for finding flaws within plain and reinforced concrete was described. The key features of the technique are:

- 1) a point source - impact of steel sphere or mechanical impactor on concrete;
- 2) a point receiver - a broadband, displacement transducer, with a small conical tip; and,
- 3) frequency spectrum analysis of displacement waveforms.

Laboratory results obtained from impact-echo tests on solid plates and plates containing flaws were presented. Observations and conclusions drawn from the analytical and finite element studies were used to aid in interpreting experimental results.

## 8.2 CONCLUSIONS

The significant conclusions reached as a result of the studies presented in this report are stated in the following sections.

of surface displacement waveforms obtained from plates containing disk-shaped flaws:

- 1) The larger the ratio of the diameter of the flaw to the depth of the flaw ( $D/T$ ), the easier it is to detect the flaw.
- 2) The critical  $D/T$  value increases as the contact time of the impact increases.
- 3) As was found for solid plates, effects produced by a flaw on surface displacement waveforms are most pronounced when the waveforms are generated using impacts having shorter contact times and are recorded close to the point of impact; these waveforms are the simplest to interpret.

The numerical flaw studies presented in this report demonstrate that the finite element method is a powerful tool for studying stress wave propagation within solids having arbitrary shapes, boundary conditions, and applied loads, and containing defects.

#### 8.2.1 Laboratory Studies

To accurately interpret waveforms and frequency spectra, the P-wave velocity must be determined from an impact-echo test on a part of the test object of known thickness. P-wave velocities obtained using the ultrasonic, through-transmission method are approximately 10 percent higher than those calculated from impact-echo results.

Frequency spectrum analysis simplifies signal interpretation.

### 8.3 FUTURE RESEARCH

The availability of two- and three-dimensional dynamic finite element computer codes, such as the DYNA code used in this report, and the availability of supercomputers, now make it possible to study a wide variety of nondestructive testing related problems which could not be studied using other existing analytical or numerical methods. The two-dimensional studies of planar flaws in plates that were presented in this report are the first of an almost unlimited number of stress wave propagation problems that could be studied using the finite element method. For example, the standard flat-bottom hole specimens that are used routinely in ultrasonic flaw calibration studies could be analyzed. A classical three dimensional problem that could be solved is the interaction of transient waves with a cylindrical inclusion.

The studies in this report have been restricted to plate-like structures. Before the field potential of the method can be realized, analytical and experimental studies of other structural elements, such as rectangular beams and round columns must be carried out. In addition, the ability of the impact-echo method to detect other types of flaws needs to be investigated. For example, a common type of flaw in concrete structures is "honeycombing" - concrete that is not fully consolidated.

Field testing of the proposed impact-echo method is essential. A practical and efficient field system must be assembled and evaluated under actual field conditions. The key component of this field system will be the development of a rugged displacement



## BIBLIOGRAPHY

1. Abduljabbar, Z., Datta, S., and Shah, A., "Diffraction of Horizontally Polarized Shear Waves by Normal Edge Cracks in a Plate," *Journal of Applied Physics*, Vol. 54, No. 2, February, 1983, pp. 461-472.
2. Achenbach, J., Gautesen, A., and McMaken, H., "Diffraction of Elastic Waves by Cracks - Analytical Results," *Elastic Waves and Non-Destructive Testing of Materials*, ASME, AMD, Vol. 29, Y.H. Pao, ed., 1978, pp. 33-52.
3. Alexander, A. M., "Feasibility of Sonic Pulse-Echo Technique," Misc. Paper C-77-11, U.S. Army Engineer Waterway Experiment Station, Vicksburg, Miss., April, 1980, 25 pp.
4. American Society for Testing and Materials, 1985 Annual Book of ASTM Standards, Philadelphia, Vol. 04.02.
5. Banks, B., Oldfield, G., and Rawding, H., Ultrasonic Flaw Detection in Metals, Prentice-Hall, Inc., New Jersey, 1962, 256 pp.
6. Bell, F., ed., Foundation Engineering in Difficult Ground, Butterworth and Co., Ltd., London, 1978, 598 pp.
7. Bond, L., "Methods for the Computer Modelling of Ultrasonic Waves in Solids," in Research Techniques in Nondestructive Testing, Vol. 6; R. Sharpe, ed., Academic Press, New York, pp. 107-150.
8. Bond, L., Jayasundere, N., Sinclair, D., and Smith, I., "Investigation of Ultrasonic Transducers as used for Nondestructive Testing," in *Review of Progress in Quantitative Nondestructive Evaluation*, Vol. 1, D. Thompson and D. Chimenti, eds., Plenum Press, New York, 1982, pp. 691-701.
9. Bowles, J., Foundation Analysis and Design, 2nd ed., McGraw-Hill Book Co., New York, 1977, 750 pp.
10. Bracewell, R., The Fourier Transform and its Applications, 2nd ed., McGraw-Hill Book Co., 1978, 444 pp.
11. Bradfield, G. and Gatfield, E., "Determining the Thickness of Concrete Pavements by Mechanical Waves: Directed Beam Method," *Magazine of Concrete Research*, V. 16, No. 46, March, 1964, pp. 49-53.
12. Bredenberg, H., ed., *Proceedings of the International Seminar on the Application of Stress-Wave Theory on Piles*, Stockholm, June, 1980, 344 pp.

27. Gardner, W. and Hudson, J., "Ultrasonic Inspection of Thick Section Pressure Vessel Steel by the Time of Flight Diffraction Method," Proc. of 5th International Conference on NDE in the Nuclear Industry, San Diego, California, May, 1982, pp. 250-257.
28. Goldsmith, W., Impact: The Theory and Physical Behavior of Colliding Solids, Edward Arnold Press, Ltd., 1965, pp. 24-50.
29. Goudreau, G. and Hallquist, J., "Recent Developments in Large-Scale Finite Element Lagrangian Hydrocode Technology," Computer Methods in Applied Mechanics and Engineering, Vol. 33, 1982, pp. 725-757.
30. Graff, K., Wave Motion in Elastic Solids, Ohio State University Press, 1975.
31. Hall, K., "Observing Ultrasonic Wave Propagation by Stroboscopic Visualization Methods," Ultrasonics, Vol. 20, No. 4, July, 1982, pp. 159-167.
32. Hallquist, J., "A Procedure for the Solution of Finite-Deformation Contact-Impact Problems by the Finite Element Method, UCRL-52066, Lawrence Livermore Laboratory, April, 1976, 46 pp.
33. Hallquist, J., "User's Manual for DYNA2D - An Explicit Two Dimensional Hydrodynamic Finite Element Code with Interactive Rezoning," Lawrence Livermore Laboratory, Rev. Jan., 1984.
34. Hallquist, J., "User's Manual for MAZE: An Input Generator for DYNA2D and NIKE2D," June, 1983.
35. Hallquist, J., "User's Manual for ORION: An Interactive Post-processor for the Analysis Codes NIKE2D, DYNA2D, and TACO2D," July, 1983.
36. Hearne, T., Jr., Stokoe, K., and Reese, L., "Drilled Shaft Integrity by Wave Propagation Method," Journal of the Geotechnical Engineering Division, ASCE, Vol. 107, No. GT10, Oct., 1981, pp. 1327-1344.
37. Higgs, J., "Integrity Testing of Piles by the Shock Method," Concrete, Oct., 1979, pp. 31-33.
38. Howkins, S., et al., "Pavement Thickness Measurement Using ultrasonic Techniques," Highway Research Record, No. 378, 1972, pp. 20-28.
39. Hsu, N., "Dynamic Green's Function of an Infinite Plate - A Computer Program," NBSIR 85-3234, National Bureau of Standards, Gaithersburg, Maryland, Oct., 1985.

53. Miller, G. and Pursey, H., "The Field and Radiation Impedance of Mechanical Radiators on the Free Surface of a Semi-infinite Solid," Proc. of the Royal Society of London, A, 223, 1954, pp. 521-541.
54. Miller, G. and Pursey, H., "On the Partition of Energy Between Elastic Waves in a Semi-Infinite Solid," Proc. of the Royal Society of London, A, 233, 1955, 55-69.
55. Miklowitz, J., The Theory of Elastic Waves and Waveguides, North Holland, 1978.
56. Moore, W., Swift, G., and Milberger, L., "An Instrument for Detecting Delamination in Concrete Bridge Decks," Highway Research Record, No. 451, 1973, pp. 44-52.
57. Muenow, R., "A Sonic Method to Determine Pavement Thickness," Journal of the PCA Research and Development Laboratories, Vol. 5, No. 3, Sept., 1963, pp. 8-21.
58. Nand, K., Desai, P., Marwadi. S., Wedpathak, A., and Guha, S., "A Sonic Method for the Detection of Deep Cracks in Large Structures," Indian Concrete Journal, March, 1974, pp. 98-102.
59. Niwa, Y., Kitahara, M., and Ikeda, H., "The Boundary Integral Equation Approach to Transient Wave Propagation Problems Around Elastic Inclusions," Theoretical and Applied Mechanics, Vol. 32, University of Tokyo Press, 1984, pp. 183-198.
60. Ogilvy, J. and Temple, J., "Diffraction of Elastic Waves by Cracks: Application of Time-of-Flight Inspection," Ultrasonics, Vol. 21, No. 6, Nov., 1983, pp. 259-269.
61. Olson, L. and Thompson, R., "Case Histories, Evaluation of Drilled Pier Integrity by the Stress Wave Propagation Method," in Drilled Piers and Caissons II, ed. C. Baker, Jr., ASCE, May, 1985, pp. 28-41.
62. Paquet, J., and Briard, M., "Controle non destrucht des pieux en beton," Annales de L'Institut Technique du Batiment et des travaux Publics, No. 337, March, 1976, pp. 49-80.
63. Pao, Y.H. and Gajewski, R., "The Generalized Ray Theory and Transient Responses of Layered Elastic Solids," Physical Acoustics, Vol. XIII, W. P. Mason and R. Thurston, eds., Academic Press, New York, 1977, pp. 183-265.
64. Pao, Y. H., Gajewski, R. R., and Ceranoglu, A. N., "Acoustic Emission and Transient Waves in an Elastic Plate, J. Acoustical Society of America, Vol. 65, 1979, pp. 96-105.



77. Shipley, S., Leistner, H., and Jones, R., "Elastic Wave Propagation - A Comparison Between Finite Element Predictions and Exact Solutions," Proceedings of International Symposium on Wave Propagation and Dynamic Properties of Earth Materials, Aug., 1967, pp. 509-519.
78. Silk, M., "Sizing Crack-Like Defects by Ultrasonic Means," Chapter 2 in Research Techniques in Nondestructive Testing, Vol. 111, R. S. Sharpe, ed., Academic Press, New York, 1977, pp. 51-98.
79. Smith, A., Ultrasonic Testing Fundamentals, Metals Engineering Institute, Battelle Northwest, 1977, 19 pp.
80. Smith, R., "The Use of Surface Scanning Waves to Detect Surface Opening Cracks in Concrete," Presented at International Conference on In Situ/NDT Testing of Concrete, Ottawa, Canada, Oct. 1984.
81. Stain, R., "Integrity Testing," Civil Engineering (London), April, 1982, pp. 53-59.
82. Stearns, S., Digital Signal Analysis, Hayden Book Company, Inc., Rochelle Park, New Jersey, 1975.
83. Steinbach, J. and Vey E., "Caisson Evaluation by Stress Wave Propagation Method," Journal of the Geotechnical Engineering Division, ASCE, Vol. 101, No. GT4, April, 1975, pp. 361-378.
84. Sutherland, H., and Kent, L., "Erosion Rate Measurements Using an Acoustic Technique," Review of Scientific Instruments, Vol. 48, No. 8, Aug., 1977, pp. 1010-1016.
85. Szilard, J., ed., Ultrasonic Testing, John Wiley and Sons, Ltd., New York, 1982, 648 pp.
86. Timoshenko, S., and Goodier, J., Theory of Elasticity, 3rd ed., McGraw-Hill Book Co., New York, 1970, 567 pp.
87. Weaver, R. and Pao, Y.H., "Axisymmetric Elastic Waves Excited by a Point Source in a Plate," ASME Journal of Applied Mechanics, Vol. 49, Dec., 1982, pp. 821-836.
88. Weber, W., Jr., Grey, R., and Cady, P., "Rapid Measurement of Concrete Pavement Thickness and Reinforcement Location - Field Evaluation of Nondestructive Systems," NCHRP Report 168, 1976, 63 pp.
89. Willis, J., "Self-similar Problems in Elastodynamics," Philosophical Transactions of the Royal Society of London, Vol. 274, pp. 435-491, May, 1973.





U.S. DEPT. OF COMM. <b>BIBLIOGRAPHIC DATA SHEET</b> (See instructions)		1. PUBLICATION OR REPORT NO.  NBSIR 86-3452	2. Performing Organ. Report No.	3. Publication Date  SEPTEMBER 1986
4. TITLE AND SUBTITLE Impact-Echo: A Method for Flaw Detection in Concrete Using Transient Stress Waves				
5. AUTHOR(S) Mary Sansalone and Nicholas J. Carino				
6. PERFORMING ORGANIZATION (If joint or other than NBS, see instructions)  NATIONAL BUREAU OF STANDARDS DEPARTMENT OF COMMERCE WASHINGTON, D.C. 20234			7. Contract/Grant No.	
			8. Type of Report & Period Covered	
9. SPONSORING ORGANIZATION NAME AND COMPLETE ADDRESS (Street, City, State, ZIP)  National Bureau of Standards Department of Commerce Gaithersburg, Maryland 20899				
10. SUPPLEMENTARY NOTES  <input type="checkbox"/> Document describes a computer program; SF-185, FIPS Software Summary, is attached.				
11. ABSTRACT (A 200-word or less factual summary of most significant information. If document includes a significant bibliography or literature survey, mention it here) To develop a basis for a nondestructive test method for heterogenous solids, analytical, numerical, and laboratory studies of transient stress wave propagation in plain plates and in plates containing flaws are presented. The test method involves introducing transient stress waves into a test object by mechanical point impact and monitoring reflections of the waves from internal defects and external boundaries using a point receiver. Exact Green's function solutions for a point source on an infinite plate are used to study the response of a plate to elastic impact by a sphere in both the time and frequency domains. Displacement and stress fields produced by a transient point load on the top surface of a plate are obtained using the finite element method. The finite element method is also used to study transient wave propagation in plates containing planar flaws. The development of an experimental impact-echo technique for finding flaws within plain and steel reinforced concrete is described. Laboratory results are presented. Successes achieved in the laboratory suggest that the impact-echo method has the potential to become a reliable field technique for detecting flaws within concrete structures.				
12. KEY WORDS (Six to twelve entries; alphabetical order; capitalize only proper names; and separate key words by semicolons) concrete; finite element method; flaw detection; Green's function; nondestructive testing; stress wave propagation				
13. AVAILABILITY  <input checked="" type="checkbox"/> Unlimited <input type="checkbox"/> For Official Distribution. Do Not Release to NTIS <input type="checkbox"/> Order From Superintendent of Documents, U.S. Government Printing Office, Washington, D.C. 20402.  <input checked="" type="checkbox"/> Order From National Technical Information Service (NTIS), Springfield, VA. 22161			14. NO. OF PRINTED PAGES  234  15. Price  \$22.95	

